Technische Universität München
Fakultät für Chemie
Lehrstuhl für Physikalische Chemie

Defect Dynamics at the Fe_3O_4 (001) Surface under the Fast Scanning Tunnelling Microscope: Real-Time Studies on an Oxide Catalyst

Dissertation

Alexander Bourgund

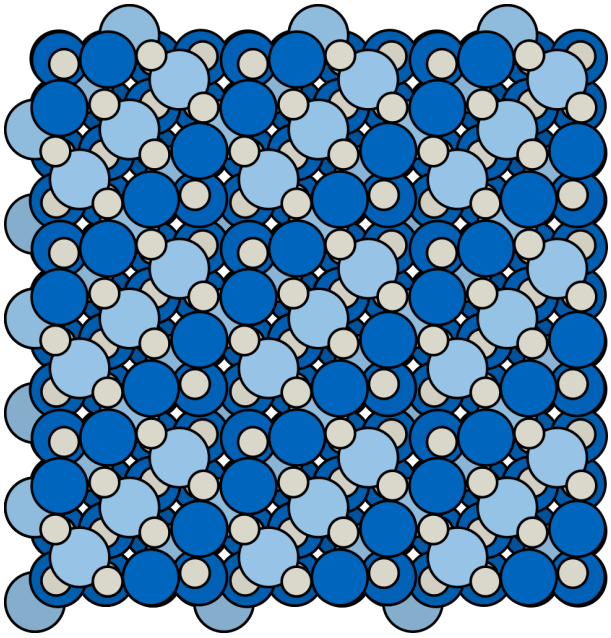

Technische Universität München
Fakultät für Chemie
Lehrstuhl für Physikalische Chemie

Defect Dynamics at the Fe_3O_4(001) Surface under the Fast Scanning Tunnelling Microscope: Real-Time Studies on an Oxide Catalyst

Alexander Bourgund

Vollständiger Abdruck der von der Fakultät für Chemie der Technischen Universität München zur Erlangung des akademischen Grades eines

Doktors der Naturwissenschaften

genehmigten Dissertation.

Vorsitzender:	Prof. Dr. Klaus Köhler
Prüfende/-r der Dissertation:	1. Priv.-Doz. Dr. Friedrich Esch
	2. Prof. Dr. Wilhelm Auwärter

Die Dissertation wurde am 20.01.2020 bei der Technischen Universität München eingereicht und durch die Fakultät für Chemie am 13.03.2020 angenommen.

Magnetite is a highly abundant catalytic oxide support with rich surface chemistry. Its surface dynamics are unveiled at increasing temperatures, and structure-dependent surface hydrogen mobility, subsurface iron mobility in domain boundaries and iron-rich defects, iron exchange with the bulk, and the dynamics of a high-temperature phase transition are observed using fast scanning tunnelling microscopy. The implementation of a highly sensitive sniffer reactor into the experiment allows for correlating structure and reactivity of such catalytic surfaces.

Magnetit ist ein katalytischer Oxidträger mit reichhaltiger Oberflächenchemie. Hier wird die Oberflächendynamik mittels schneller Rastertunnelmikroskopie bei zunehmenden Temperaturen untersucht: strukturabhängige Wasserstoffmobilität an der Oberfläche, Eisenmobilität unter der Oberfläche in Domänengrenzen und eisenreichen Defekten, Eisenaustausch mit dem Volumen und die Dynamik eines Hochtemperaturphasenübergangs. Die Implementierung eines Sniffer-Reaktors ins Experiment ermöglicht die Korrelation von Struktur und Reaktivität.

Acknowledgements

This work would not have been possible without the support and help of others.
First, I want to thank Friedrich Esch for the supervision of my thesis project in the STM lab, sharing his technical and scientific knowledge, encouraging open discussions, and his contagious enthusiasm for scientific work.
Big thanks to Ueli Heiz for the discussions and support through all the ups and downs of my time in the group. His open, accessible, and solution-oriented leadership of his research group always serves as an aspiring example for me.
I am very grateful to Barbara Lechner for sharing her experience in such different domains as investigating surface diffusion phenomena and troubleshooting ultra-high vacuum setups.
Further thanks to our cooperators in Vienna and Hamburg for the great work we did together. I am especially grateful to Gareth Parkinson for discussions about surface defects on $Fe_3O_4(001)$ and how to bolster our experimental findings with DFT calculations, Michael Schmid for providing ImageJ scripts that made the structural analysis of the FastSTM data in the phase transition project so much easier, Matthias Meier, who performed the DFT calculations, Zdenek Jakub for discussions regarding sample preparation, and Andreas Stierle for fruitful cooperation on the phase transition project.
Wolfgang Harbich shared his experiences with his Sniffer and the drawings of his instrument to serve as starting point for the development of the new instrument, for which I am very grateful to him.
Thanks to Carlo Dri and Mirko Panighel for help and discussions regarding troubleshooting and improving the FAST-Labview program and collaboration and discussions on the development of the pyfast package.
I'd like to thank Ke Zhang for discussions and the construction of the heating of the fused silica part of the sniffer. Thanks to all the students who contributed during their research internship, bachelor's or master's thesis: Lea, Sebastian, Yixia, Matthias, Jakob, Frederic, Jay, Joanne, Kathi, Nicolas, and Johanna.
I want to acknowledge Michael Eckinger for CAD drawings, Christian Schmid for software support, and Robert Spitzenpfeil for help with Gitlab and network administration.
It was a pleasure to work in the Heiz group, and I particularly want to thank Matthias Jakob, Alexander von Weber, and Farinaz Mortaheb for our productive and fun office atmosphere, Max Krause and Martin Tschurl for their enthusiasm to discuss rather obscure technical issues, Tim Kratky and Sebastian Günther for sharing spare parts on Friday evenings, and Aras Kartouzian for sharing his experience troubleshooting cluster sources. Moreover, the competent support of the electronics workshop of the chemistry department at TUM, in particular Max Wiedemann, concerning how to best create electronic controller for the sniffer and how to upgrade the existing

one for the FAST module, was always valuable to me. The mechanics workshop at the department professionally turned our plans for the sniffer (and various other sketches) into real parts, thank you very much!
I want to thank Helmut Hollfelder for discussions about science, career paths, and applied chemistry beyond the walls of academia.
Last, but not least, I want to thank my family for their love and support, and my friends for the awesome time we had and their patience and support in recent months while I have been drafting this thesis!

"The entrance into the kingdom of man, founded on the sciences, being not much other than the entrance into the kingdom of heaven, whereinto none may enter except as a little child."
-Francis Bacon, *Novum Organum*, 1620.

Table of Contents

1 Introduction

1.1 Motivation

Technical catalysts are a major part of everybody's lives at least since Döbereiner invented his famous lamp [1] in 1823. They are central for the production of the majority of chemical compounds of our daily life, and can be found in day-to-day life in domains as diverse as exhaust catalysts [2], cleaning agents [3], and fuel-cells [4]. Furthermore, catalysis plays an important role in industrial chemistry. Hydrogen production via water-gas shift reaction [5], ammonia synthesis [6], and alcohol reforming [7] are examples for industrial processes where catalysts play an important role. A breakthrough for the investigation of heterogeneous catalysts was the development of surface science techniques that allow the systematic study of the processes on a catalyst surface. The effort in this field was recognized with the Nobel prize in Chemistry in 2007 which was awarded to Gerhard Ertl *"for his studies of chemical processes on solid surfaces"*, especially the investigation of the catalyst for ammonia synthesis. [8]

Today's and future societies are facing enormous challenges to change the way energy is produced, stored, and transported to transition to renewable energy sources and combat climate change. One attempt to contribute to overcoming both challenges with the help of technology is transforming the way the economy is driven to a *hydrogen economy* [9], which uses hydrogen as a means of storing energy as is done with petrol up until now. The German federal government is working on a national hydrogen strategy [10, 11] to boost the implementation of the technological and logistical changes necessary. A core of these efforts is the development, improvement, and spread of CO_2-free and CO_2-neutral technologies. [11] Hydrogen can be used as a fuel that is synthesised at the location where renewable energy sources are harvested (near wind plants or close to solar plants). It can then be transported to regions where renewable energy sources are not available. Similarly, this would allow vehicles to "refuel" hydrogen gas instead of petrol and use a fuel cell to generate the energy necessary to drive the vehicle.

Surface science methods can yield information on, amongst others, catalyst stability and reactant and intermediate species transport processes. Investigating the stability of catalysts dependent on temperature and pressure helps to better understand catalyst deactivation and poisoning processes. [12–14] Furthermore, transport processes on the catalyst surface like hydrogen atom transport can be critical for a reaction and strongly influence its reaction rate. [15, 16]

Already in today's economy, the production of hydrogen is a major industrial process that supplies CO-free reactants to the Haber-Bosch process [5, 6]. Currently, the major source for hydrogen is the steam methane reforming process,

$$\mathrm{CH_4 + H_2O \rightleftharpoons 3\,H_2 + CO}, \tag{1.1}$$

producing CO as a product. This CO can be used in a second step to synthesis more hydrogen by the water-gas shift (WGS) reaction,

$$CO + H_2O \rightleftharpoons H_2 + CO_2. \tag{1.2}$$

Thereby, the WGS reaction can use CO - which is a common (by-)product [17] - to generate hydrogen without additional consumption of otherwise useful carbon compounds. This is why it is considered CO_2-neutral in the framework of the national hydrogen strategy. [11] The WGS reaction is typically performed using two reactors in series. [17, 18] The first reactor generally uses an iron-oxide (Fe_3O_4) based catalyst at 600-700 K (high-temperature water-gas shift reaction, HT-WGS), while the second reactor is operated at lower temperatures with a copper-zinc oxide based catalyst (460-520 K, low-temperature water-gas shift reaction, LT-WGS). While a lot of work has been done to find new and better catalysts for the WGS reaction on a trial-and-error basis in the past, the processes at the iron oxide based catalyst for the HT-WGS reaction are still not fully understood on the atomic level. [18]

Classical surface science studies commonly use ultra-high vacuum pressures and operate scanning tunnelling microscopes at temperatures of room temperature and below. The continuous development of state-of-the-art surface science techniques towards reaction conditions can make significant contributions to understanding the mechanistic steps at catalyst surfaces, thereby drawing closer to the industrial catalyst. In this thesis, two complementary approaches are pursued to approximate conditions of the catalysts in use, exploring high temperature surface dynamics and reactivity at increased pressures.

The first approach uses accelerated scanning tunnelling microscopy at temperatures up to 784 K to study dynamic processes on the atomic scale. As the $Fe_3O_4(001)$ surface - the most stable surface of magnetite [19] - commonly shows various defects [20], the microscopic ansatz of atomically resolved microscopy allows to distinguish effects from different kinds of defects and their influence on each other. Transport processes on the $Fe_3O_4(001)$ surface of hydrogen are investigated quantitatively at temperatures between room temperature and 382 K and the effect of local iron-rich sites on these dynamics is described. The subsurface mobility of iron at the $Fe_3O_4(001)$ surface is investigated between 353 K and 516 K. Furthermore, fast STM measurements in the high-temperature phase transition of the $Fe_3O_4(001)$ surface are presented, providing the first real space information on the subsurface mobility of cations during the order-disorder phase transition around 720 K, which is close to the reaction temperature of the HT-WGS reaction.

Secondly, subnanometre-sized metal clusters supported by this $Fe_3O_4(001)$ support can allow to tune the catalytic properties of this material, adding an additional layer of complexity to the sample. In order to perform high-sensitivity experiments at variable pressures (up to 10^{-4} mbar) within an ultra-high vacuum system, a special instrument is designed, constructed and implemented as part of this thesis. The instrument is a pulsed mini-reactor called ”sniffer”, which is sensitive enough to obtain quantitative information on the catalytic properties of small amounts of sub-nanometre sized metal clusters.

1.2 Nanoparticles and Nanoclusters in Catalysis

Heterogeneous catalysts often contain noble metals, e.g. platinum or palladium. This makes their application particularly costly. As only atoms at the surface of a heterogeneous catalyst can directly interact with the reactants, catalysts in bulk form only use a small fraction of their atoms to catalyse a reaction. The surface/volume ratio can be improved a lot by the use of catalysts at the nanoscale as that ratio is much higher, and so is the amount of active sites per mass.

For nanoparticles, the general behaviour for a given chemical or physical property, χ, is usually [21, 22]) described by

$$\chi(N) = \chi_{\text{inf}} + a\frac{1}{R} \tag{1.3}$$

with the bulk value represented as χ_{inf}, a constant, a, and the effective radius of the nanoparticle, R. Using the electron affinity (EA) as an example for a physical property illustrates this relationship. Figure 1.1a shows that the electron affinity decreases following this principle over a wide range until the particle size reaches a size of a few tens of atoms [22, 23] dependent on the material of interest. In the range of the smallest particles commonly termed "cluster", the properties can become non-linear and depend on the exact number of atoms [23–25]. In the nano-sized region, new reaction paths can open up [26] and even noble metals like gold (which is catalytically inert as bulk material) in form of nanoparticles become catalytically active for CO combustion [27–29]. Decreasing the particle size further to cluster, the non-scalable size regime sets in and the catalytic activity can change dramatically with each additional atom [30] (see figure 1.1). CO adsorption/desorption kinetics of Pd nanoparticles [31] resemble those of bulk palladium [32], while Pd clusters behave differently, showing the potential for new insights on the non-scalable size regime for catalysis [26]. Examples for cluster size-dependent reactivity include the reactivity of CO with NO to CO_2 and N_2 on palladium clusters [33], CO oxidation through platinum clusters on TiO_2 [34], the cyclotrimerization of acetylene on palladium cluster on MgO [25], and ethylene hydrogenation on platinum clusters [35, 36].

The scientific reasoning to explain the astonishing properties of metal clusters is based on three principles [37] that distinguish them from rather large nanoparticles in the scalable size regime and bulk materials. First, the electronic structure of small metal clusters can show a significant size effect [38–42], which highly impacts the chemical properties. In addition, it is possible to change the electronic structure by adding an atom of a different element and thus influencing the electronic structure (shown for doping Au clusters with Sr in figure 1.2a). [37] Second, the clusters can have multiple isomers close to the ground state, between which they can easily alternate and therefore create new reaction channels (see figure 1.2b). [43] The rapid fluctuation between such isomers is called dynamic structural fluxionality. [37, 41, 43–45]

The third aspect that distinguishes the chemical properties of metal clusters from bulk material is the interaction of the clusters with the support material, which can provide or withdraw electrons to the clusters, influence their electronic structure and therefore impact their catalytic properties. [46–49]

When depositing clusters onto the support material, care must be taken to deposit them intact and avoid inserting the cluster into the support material. This can be achieved through electrostatic

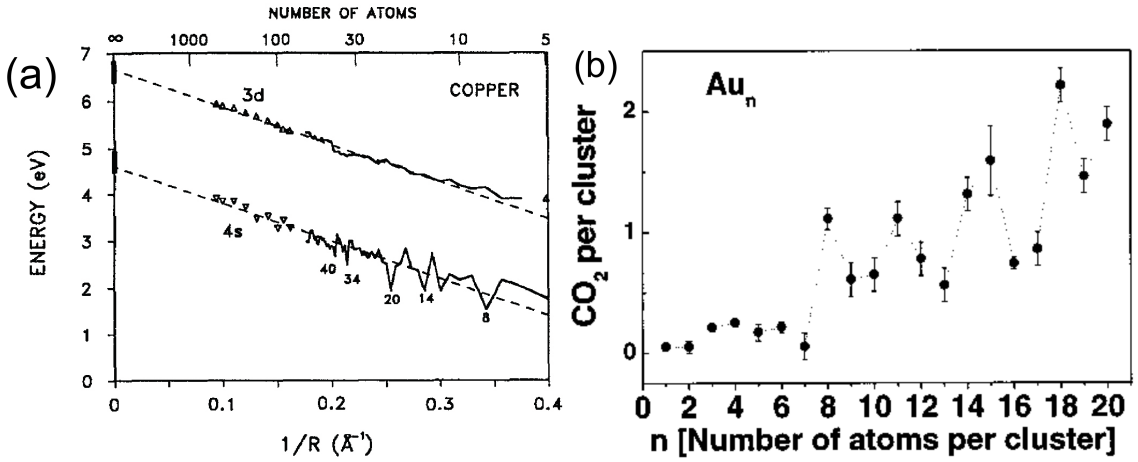

Figure 1.1: Scalability at the nanoscale: (a) The onsets of the 3d and 4s bands determined by ultraviolet photoelectron spectroscopy (UPS) for copper nanoparticles linearly decreases with $\frac{1}{R}$. The scaling relation holds down to a few tens of atoms, where the non-scalable size regime begins. This regime starts at larger cluster sizes for the 4*s* band than the 3*d* band. Reprinted from *J. Chem. Phys.* **1992**, *96*, 3319–3329, with the permission of AIP Publishing. (b) Gold clusters are (contrary to the catalytically inert bulk material) efficient catalysts for CO combustion. Their activity is highly dependent on the size of the cluster. Catalytic activity starts at Au_8 clusters and varies non-linearly with each additional atom. Reprinted with permission from *J. Phys. Chem. A* **1999**, *103*, 9573–9578. Copyright 1999 American Chemical Society.

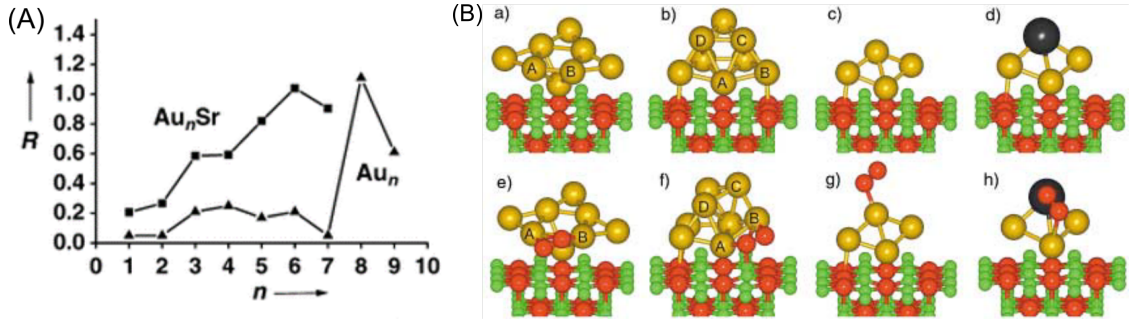

Figure 1.2: (A) Doping Au clusters with a Sr atom leads to significant changes in the chemical reactivity, R, towards CO. (B) In the non-scalable size regime, the clusters have multiple states which are close in energy, allowing the cluster to interchange between them if energetically favourable during a reaction, as shown here for the example of Au and Sr-doped Au clusters Reprinted with permission from *Angew. Chem., Int. Ed.* **2003**, *42*, 1297–1300. Copyright 2003 John Wiley and Sons.

lenses and a retarding field on the support material, which allows the soft-landing [50–53] of clusters with kinetic energies lower than 2 eV/atom, which is the fragmentation threshold determined by molecular dynamics calculations. [50, 52, 54] Figure 1.3 shows that fragments of metal clusters landed on a graphene film with a kinetic energy of 100 eV can indeed be observed and differ from soft-landed clusters. [53]

The stability of clusters on surfaces is of interest to sustain the catalytic properties over time. Possible deactivation processes include catalyst poisoning [55–57], sintering of the clusters [13] and catalyst loss by reaction of catalyst material to a product that can desorb [12]. In case either one reaction participant binds too strongly to the catalyst that it does not desorb easily enough, it can

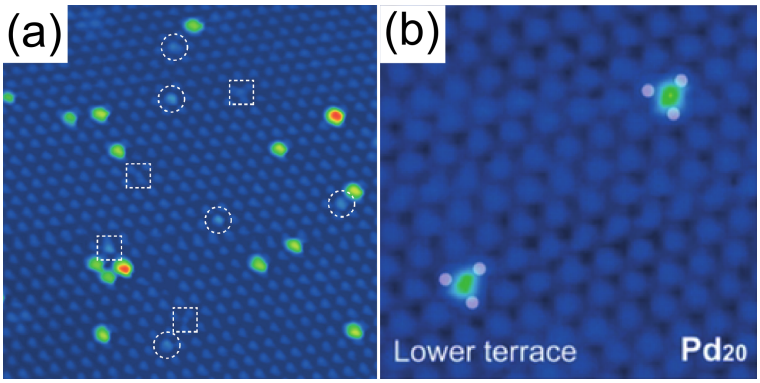

Figure 1.3: (a) Pd_{19} clusters hard-landed ($E_{kin} \approx 100$ eV) on graphene/Ru(0001). The cluster fragments due to the hard-landing are marked by squares and circles. (b) Pd_{20} clusters soft-landed on the same support do not show any fragmentation. Reprinted with permission from *Nano Lett.* **2012**, *12*, 5907–5912. Copyright 2012 American Chemical Society.

enrich at the catalyst surface and block the further adsorption of reactants. [36, 56, 57] Small metal clusters are prone to ripening into larger particles at higher temperatures. The mechanisms can involve transport atom-by-atom or cluster-by-cluster (Ostwald or Smoluchowski ripening, respectively), depends highly on the cluster-support interaction, and can change with temperature. [13] Losing catalyst material is a well-known problem in industrial ammonia synthesis, where some platinum is oxidized to PtO_2, which can become volatile at reaction conditions. [12] Furthermore, metal oxide support materials can encapsulate metal clusters deposited on their surface and thereby prevent contact between the cluster and the reactants. [58–61] This phenomenom is called strong metal-support interaction (SMSI).

1.3 Metal Oxides in Catalysis

In many industrial processes, metal oxide supports are used as heterogeneous catalysts like MgO, Al_2O_3, or Fe_3O_4 [5] due to their high stability and abundance [17]. The properties of the support material strongly influence the catalyst performance. As described in chapter 1.2, the relative strength of the cluster-support interaction can change the structure of deposited clusters and thereby their reactivity. [46–49] One of the most abundant materials is the iron oxide magnetite (Fe_3O_4). It has been used as a precursor for Fe^0 - the catalytically active species in the ammonia synthesis [62] - and as starting material in steel production [63]. Because of its abundance, non-toxicity, and affordability [64], it is an attractive support material for catalysis, and widely used for the water-gas shift reaction [5, 18]. Figure 1.4 shows the dependence of the surface free energies on the facet as distance from the centre (Wulff construction [65]) for magnetite based on density functional theory (DFT) calculations [19]. The most stable surfaces of magnetite are the (001) and (111) surfaces, leading to cubic and octahedral crystal shapes. [19, 66] In recent years, single atoms on magnetite (001) have been investigated. Some metal atoms like Ni [67] seem to be more stable towards ripening than others like Pt [68, 69].

Early studies [70, 71] already in the 1990s found that the atomic structure of magnetite (001) is sensitive to the preparation procedure. Magnetite crystallizes in a face-centred cubic (fcc) struc-

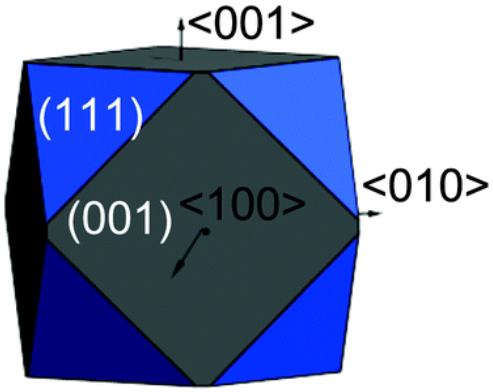

Figure 1.4: Surface free energy for multiple crystal facets of Fe_3O_4. In this representation, higher surface free energy of a surface structure correlates to longer distance from the centre of the crystal. (Wulff construction [65]) The stability of the facets decreases from the (001) to the (111) surface. Reproduced from *Phys. Chem. Chem. Phys.* **2014**, *16*, 21082–21097. - Published by the PCCP Owner Societies.

ture with both Fe^{2+} and Fe^{3+} present in order to reach charge neutrality. The accepted model for the (001) surface is the subsurface cation vacancy structure (SCV) of the $\left(\sqrt{2} \times \sqrt{2}\right)$ R45° reconstruction by Bliem et al. [72], which is well suited to explain a wide range of observations on this surface. [20] It has characteristically undulating rows of Fe_{oct} that are separated by Fe_{tet} (see figure 1.5BC). In a simple bulk-truncated model (see figure 1.5A), one half of tetrahedral lattice positions would be occupied. In contrast, in the SCV reconstruction, three quarters of the tetrahedral surface lattice positions are occupied. At the same time, two Fe_{oct} atoms in the third layer are missing, of which one moved to the second layer to increase the above-mentioned occupation of the Fe_{tet} positions and the other one went to the bulk. As the tetrahedral vacancies are the preferred adsorption sites (called non-blocked sites as there is no Fe_{tet} in the second layer that could block the adsorption [72]) for metal atoms like Ag and Pd, the SCV model predicts only one adsorption site per unit cell for these metals, instead of two sites for the bulk truncated model, which is in agreement with experimental observations [72–76]. Furthermore, Ni and Ir adatoms adsorbed on the surface can move to the position vacated by Fe_{oct} in the third surface layer in the SCV reconstruction as visible in figure 1.6. [76, 77] The reconstructed unit cell has a formal $Fe_{11}O_{16}$ stoichiometry and consists exclusively of Fe^{3+}. [72]

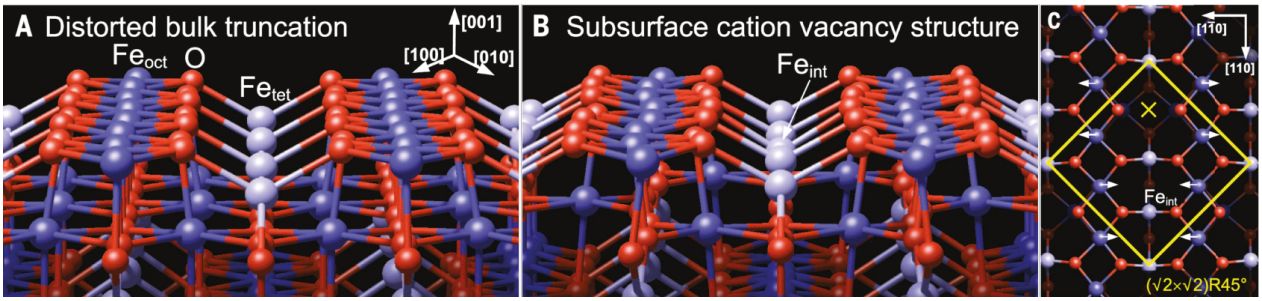

Figure 1.5: The $Fe_3O_4(001)$-$\left(\sqrt{2} \times \sqrt{2}\right)$ R45° reconstructed surface (B) is compared to a hypothetical distorted bulk truncated structure (A). (C) A top view of the reconstructed surface emphasizes the blocked Fe_{int} site and the unblocked site (yellow X). From *Science* **2014**, *346*, 1215–1218. Reprinted with permission from AAAS.

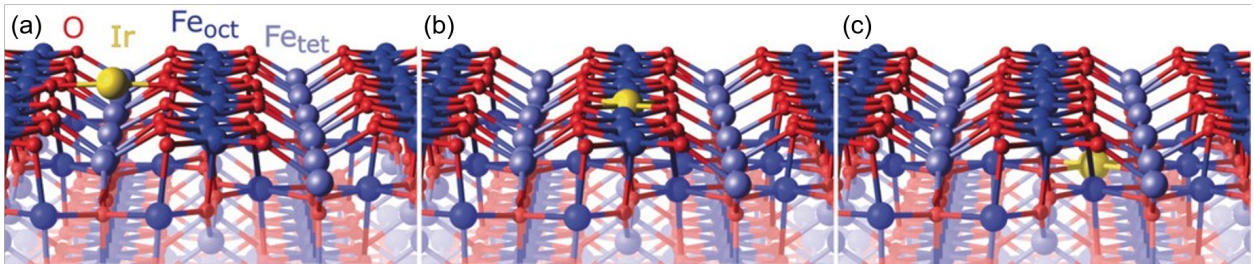

Figure 1.6: Metal atoms like iridium are adsorbed on $Fe_3O_4(001)$ at the two oxygen atoms of the unit cell where a tetrahedral position is vacant in the second layer (a). Heating can cause their substitution into the rows of octahedral Fe atoms in the first layer and the substituted Fe atom is displaced to the third layer (b, heated to 623 K). At higher temperatures, the iridium atom can move to the octahedral vacancy in the third layer of the SCV reconstruction (c, heated to 723 K). Reprinted from Jakub, Z. et al. *Angew.Chem* **2019**, *131*, 14099–14106 under Creative Commons Attribution License.

Real-world magnetite surfaces are known for their variety of defects which influence the physical and chemical properties. An overview of common defects is shown in figure 1.7. Unit cells in which the atom transfer leading to the SCV reconstruction did not happen create local structures similar to the bulk truncated model and are therefore called "unreconstructed unit cells". [20, 78] When two different domains meet, an anti-phase domain boundaries (APDB) is created, which is a line defect where locally unblocked sites are next to each other, creating a row of local defects, which consist of 4 Fe_{oct} next to each other in the third surface layer. [78, 79] Hydrogen atoms can adsorb onto the surface forming a surface hydroxyl group at the non-blocked sites by binding to the respective oxygen atoms of the first surface layer. [80–83] Initial adsorption of methanol and formic acid takes place at the unblocked site as well. Adsorption of these molecules as well as atomic hydrogen at coverages higher than one particle per unit cell leads to the lifting of the $\left(\sqrt{2} \times \sqrt{2}\right)$ R45° reconstruction. [78, 81, 84]

Figure 1.7b shows the phase diagram of the magnetite (001) surface from theoretical calculations. The SCV structure shows a stable regime spanning the common pressures accessible in ultra-high vacuum (UHV) and near ambient pressure (NAP) studies. Evaporating Fe onto the surface creates Fe adatoms, which can move into the surface reconstruction, as described above for Ni and Ir atoms, creating local unreconstructed unit cells. Upon higher coverages, patches of bulk-truncated $(1x1)$ form, followed by some Fe dimers on top of Fe_{tet}. [20, 85]

The SCV reconstructed $Fe_3O_4(001)$ surface is known to adsorb water [83, 86], formic acid [84], and alcohols [78] in a dissociative manner. Alcohol reforming has been observed for methanol on magnetite surface defects. Step edges, Fe adatoms, APDBs, and unreconstructed unit cells on $Fe_3O_4(001)$ are reactive sites for methanol to be oxidized to methanal. [78] On FeO(111) thin films, various alcohols can be oxidized. [87]

Pd [74] and Pt [69] atoms evaporated onto the $\left(\sqrt{2} \times \sqrt{2}\right)$ R45° $Fe_3O_4(001)$ become mobile and sinter into clusters upon CO exposure. Composite materials based on $Fe_3O_4(001)$ crystals show carbon monoxide oxidation (Pd, Pt) [68, 88], hydrogen oxidation and oxygen reduction [68].

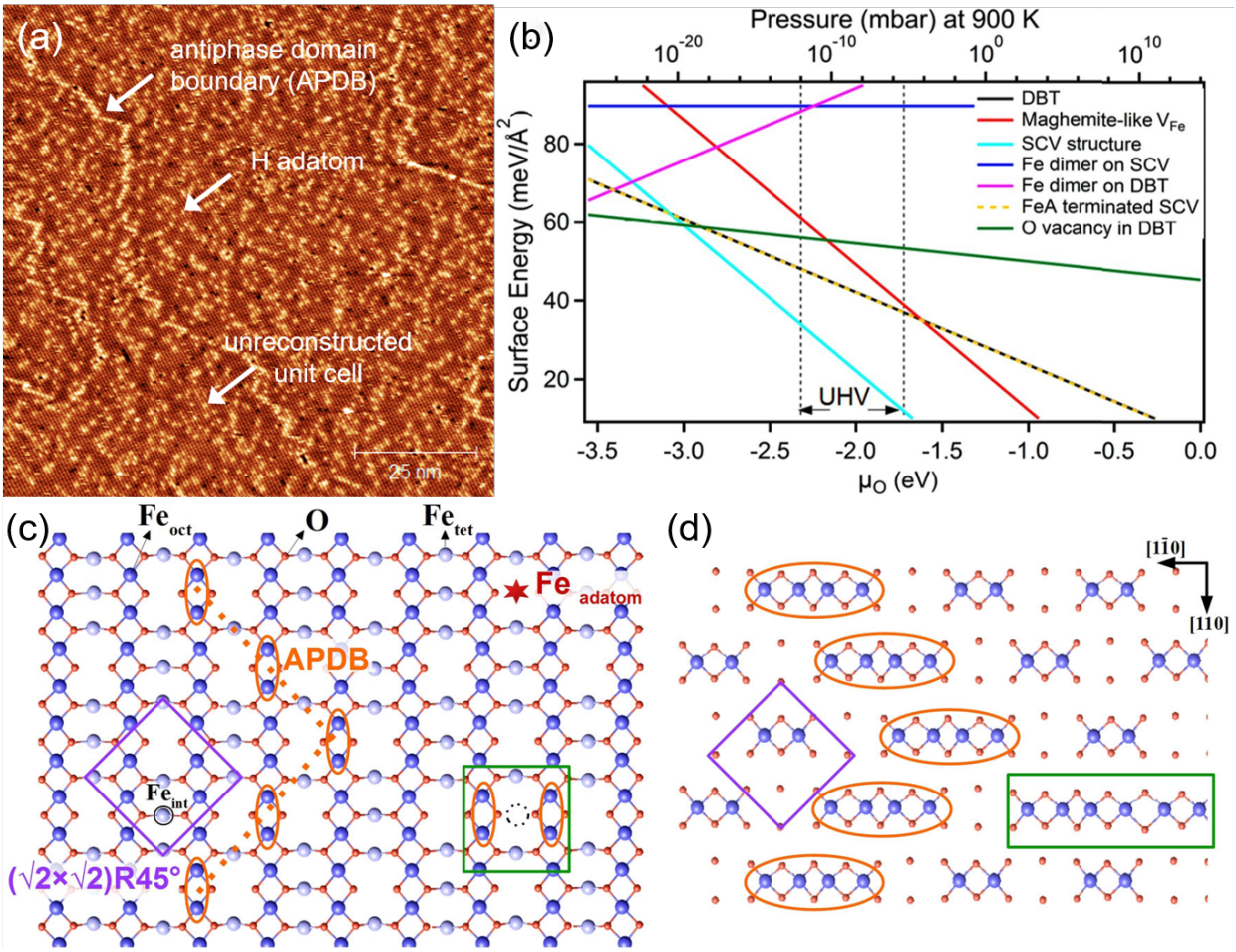

Figure 1.7: Overview of defects on the $\left(\sqrt{2} \times \sqrt{2}\right)$ R45° $Fe_3O_4(001)$ surface under the scanning tunnelling microscope (a) and interpreted according to the SCV model. (c, figure from [78].) The structure displays the first and second layer of the surface, while the structure (d, figure from [78].) represents the third layer of the surface. The purple square indicates the unit cell of the $\left(\sqrt{2} \times \sqrt{2}\right)$ R45° structure. Orange ovals mark an APDB, while green rectangles mark the unreconstructed unit cell. A possible location for a Fe adatom is represented by a red star. (c) Surface phase diagram based on theoretical calculations for different models for the magnetite surface. The chemical potential is correlated to the O_2 pressure at 900 K on the upper x-axis. (b, figure adapted from [20] based on [72])). (a) Reprinted with permission from *J. Phys. Chem. C* **2019**, *123*, 19742-19747. Copyright 2019 American Chemical Society. (b) Reprinted from Surf. Sci. Rep., *71*, Parkinson, G. S., Iron oxide surfaces, 272–365, Copyright 2016, with permission from Elsevier based, based on an figure from *Science* **2014**, *346*, 1215–1218. Reprinted with permission from AAAS. (c,d) Reprinted from Gamba, O. et al. *Top. Catal.* **2017**, *60*, 420–430 under CC 4.0.

2 Experimental Methods

2.1 Scanning Tunnelling Microscopy

Since its invention by Binnig and Rohrer [89–92] in 1979, scanning tunnelling microscopy (STM) has proven itself a very useful tool that can provide a whole range of information on surfaces and surface processes [61, 93, 94] and has even been used for some piece of art [95]. It has enabled scientists to investigate the structure of surfaces from µm to nm and hundreds of pm in real space. It can provide information about e.g. topography and thus the surface structure [61, 93], local conductivity [96], and in some cases even the shape of molecular orbitals [97] dependent on what kind of regulation and scanning parameters are used.

2.1.1 Principles of Scanning Tunnelling Microscopy

Scanning tunnelling microscopy[1] works because when a bias voltage (U_B) is applied between a sharp metallic tip and a (at least semi-)conducting sample which are brought close to each other, a tunnelling current (I_t) can be detected. Wave functions of electronic states near the Fermi level of the sample show a decay length κ into vacuum of

$$\kappa = 5.1\sqrt{\phi[eV]}\ nm^{-1} \tag{2.1}$$

with $\phi[eV]$ being the work function of the sample in eV. The tunnelling current, I_t, scales exponentially with the tip-sample distance, d, from the local density of states (LDOS, $\rho(z=0, E_F)$, E_F being the Fermi level and the height above the sample, z) at the sample surface and the Fermi level

$$I_t \propto U_B\ \rho_{Sample}(z=0, E_F)\ e^{-2\kappa d} \tag{2.2}$$

$$I_t \propto U_B\ \rho_{Sample}(z=0, E_F)\ e^{-10.2\ \sqrt{\phi[eV]}\ d} \tag{2.3}$$

and thus with the work function.
Using the work function of magnetite (001) of 5.20 ± 0.15 eV [103] with equation 2.3 to calculate the exponential term of equation 2.3 shows the surface sensitivity of STM measurements, since only the foremost atoms of the tip contribute to the tunnelling current (see table 2.1). In order to achieve topographic images, two methods can be employed. Moving the tip laterally at a certain height and detecting the tunnelling current is called "constant height" measurement and returns a 2D map of the local tunnelling current. The other approach is called "constant current" measurement and adjusts the height of the tip via a PI regulation to keep the tip at a constant current above

[1] Theoretical describtion of scanning tunnelling microscopy can be found in most surface science textbooks and in research papers. The theoretical description in this chapter is mainly based on [98–102] and further information on the general theory can be found there.

Table 2.1: The tunnelling current is highly sensitive to the tip-sample distance (as expressed by equation 2.3). Calculating the tunnelling current decay in steps of a typical atomic diameter for transition metals (0.3 nm) shows a decay of 10^{-3} for each atomic diameter. Therefore, only the foremost atoms of the tip contribute to the tunnelling current allowing for STM measurement on the atomic scale.

tip-sample distance d	0.0 nm	0.3 nm	0.6 nm	0.9 nm	1.2 nm
exponential term of eq. 2.3	1.0	9.3×10^{-4}	8.7×10^{-7}	8.1×10^{-10}	7.6×10^{-13}

the sample surface. The relative change in tip height thus represents the relative height of the electronic structure of the surface in the scanned area and enables long range scans of surfaces as it reduces the risk of the tip crashing into the sample surface. Therefore, all conventional STM measurements in this thesis are done in constant current mode. Figure 2.1 displays a schematic of a conventional scanning tunnelling microscope with a PI regulation for the tip height to measure the topography of the LDOS of the sample. For constant height measurements the PI regulation is switched off. Dependent on the polarity of the applied bias voltage, unoccupied or occupied

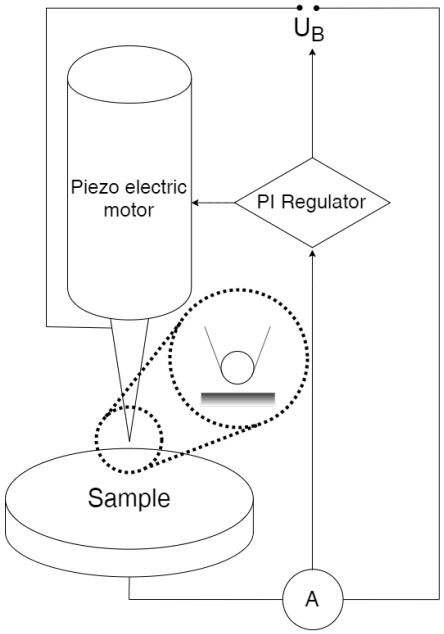

Figure 2.1: Schematic of a conventional scanning tunnelling microscope. A metallic tip is brought close to the surface of a (semi-)conducting sample. A bias voltage is applied at the tunnelling junction and a tunnelling current is detected (A). The tip scans the surface at a constant current, as the piezoelectric motor adjusts the height above the sample in a manner that ensures a constant tunnelling current. As table 2.1 demonstrates, the tunnelling current originates only from the foremost atoms of the tip drawn in the inset.

states can be measured. Variation of the bias voltage can change the electronic state detected by tunnelling.

2.1.2 Fast Scanning Tunnelling Microscopy with a Commercial Microscope

Measurement times of several minutes per frame for conventional STM allows the investigation of surfaces with fixed or frozen (e.g. by cooling to liquid nitrogen or liquid helium temperatures) structures. Conventional STM can only provide qualitative information on thermally activated processes

with significant activation energies (these processes can only be observed at higher temperatures, where the movement increases a lot with temperature), but lacks the time resolution necessary due to its limited measurement speed. In order to investigate these processes in a quantitative way, accelerated STM data is necessary.
For a long time, some researchers developed microscopes purely dedicate to accelerated STM measurements, by choosing all components in a way to shift their resonance frequency to very high frequencies [104–109] and some additionally excite the tip to move in a spiral way to avoid excitation of X and Y scanning frequencies [110].
In 2010, F. Esch and colleagues [111, 112] in Triest came up with a way to accelerate common STMs to and above video rate in a fully non-invasive way. By adding a separate electronics module, this approach combines a sinusoidal wave in the fast scanning direction with a triangular wave in the slow scanning direction, the solution by Esch avoids sharp changes in the movement of the piezoelectric scanner and adds those voltages to the ones from the conventional STM instrument. Together with the ability to correct for the unavoidable sample tilt via a z-phase shift this allows the fast acquisition of STM data. Recent developments [113] extended the application of this technique to atomic force microscopy (AFM) as well as particle tracking along with improvements in the signal generation and readout.
In this thesis, a single-tube scanner of the Omicron VT-AFM is driven by the standard *MATRIX* electronics of Omicron for standard STM measurements. For FastSTM measurements, an addition board enables to add voltages output from an field programmable gate array (FPGA). A commercial NI-PXI-1033 system (National Instruments) hosts the reprogrammable FPGA-based high-speed I/O-board (NI 5781) and a slower I/O-board (NITB-2706) for the slow scanning direction and other parameters like the sample temperature and the bias voltage. It is used with a dedicated Labview 2016 program (versions 3.0 and various development stages of 3.2) on a Windows 10 operating system. A schematic of the current electronics is shown in figure 2.2.

2.2 Low-Energy Electron Diffraction

Electron diffraction can be used to quickly probe the periodicity of the surface structure in reciprocal space. Any low-energy electron diffraction (LEED) instrument (the schematic of the instrument used here is shown in figure 2.3a) needs an electron source, e.g. a filament, a method to control their kinetic energy, and a detection method like a fluorescence screen. A suppressor grid can decrease the background from diffuse scattering. As the inelastic mean free path (IMFP) of an electron within a solid is dependent on its kinetic energy, it is possible to choose the kinetic energy so that the scattered electrons interact only with the top-most layers of a crystalline sample. Figure 2.3b provides an orientation for suitable electron energies. The IMFP has a minimum in the range of 10 - 100 eV, where the IMFP is approximately 0.5 nm.
Constructive interference of the diffracted electrons - first observed by Davisson and Germer [114] - leads to maxima of the electron beam intensity which can be detected with a fluorescence screen (a typical LEED pattern for the $\left(\sqrt{2} \times \sqrt{2}\right)$ R45° -Fe_3O_4(001) surface is shown in figure 2.4a). Those spots correspond to intersections of the Ewald sphere (which relates to the kinetic energy of the incident electron beam) with the crystal truncation rods of the surface and can therefore provide

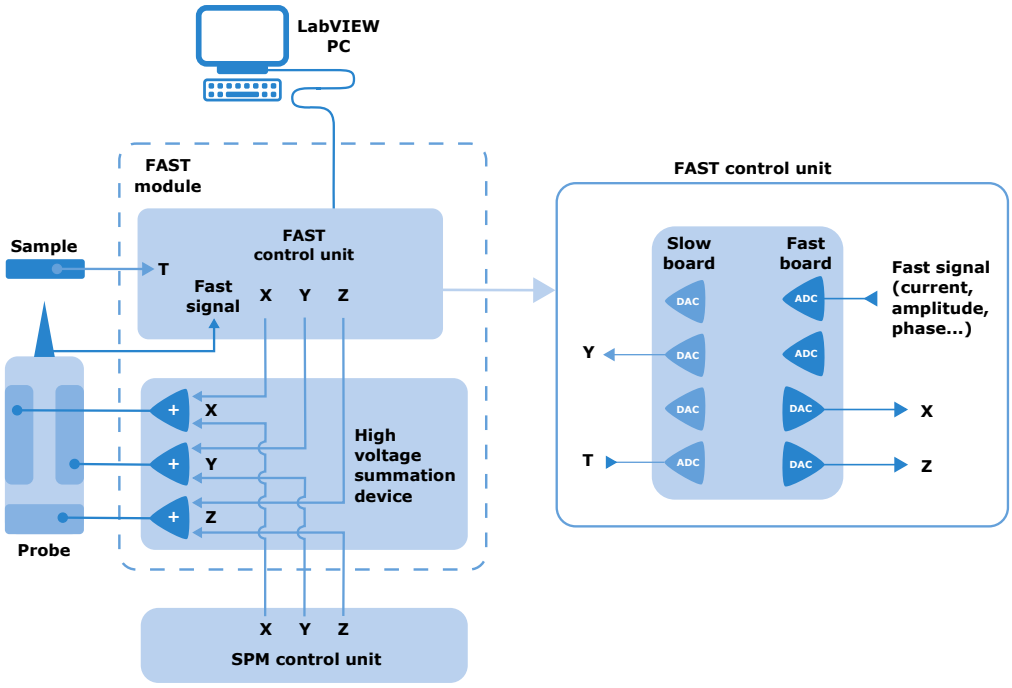

Figure 2.2: Schematic of the FastSTM control electronics add-on based on Dri et al. [113]: The FAST module (enclosed in a dashed line) generates the signal controlled by the LabVIEW computer and adds it to the one originating from the original control unit of the manufacturer and forwards the resulting signal to the piezo tube. The tunnelling current is gripped after the preamplifier before it reaches the original control unit and fed to the high-feed I/O-board, where it can be read into the Labview program and saved to a *.h5* file. A type K thermocouple is connected to the slow board via an network cable, which reads the sample temperature. Reprinted from Ultramicroscopy, 205, Dri, C. et al., The new FAST module: A portable and transparent add-on module for time-resolved investigations with commercial scanning probe microscopes, 49–56., Copyright 2019, with permission from Elsevier.

information about the periodic structure of the investigated surface. Varying the energy of the incident electron beam (and therefore the IMFP) can provide information about some subsequent layers below the top-most layer. The spot size (usually $\approx$ 1 mm) of the electron gun determines the integrated area, while the transfer width of the electron beam is the length over which the structure needs to be periodic to give independent spots. Dependent on the experimental setup and the electron energy it is typically in the range of 5 - 10 nm [115] for conventional low-energy LEED optics. A more detailed discussion can be found in the literature [115–117]. In the present work, LEED experiments were performed with a SPECS ErLEED 100 optics in the 3-grid design (as shown schematically in figure 2.3a) controlled by an ErLEED 1000A control electronics and equipped with a shutter and z-transfer. Initial measurements with a first camera (The Imaging Source, DMK 72AUC02) could not be quantified, because it could not capture enough of the fluorescence signal for quantitative image processing. To record more of the signal of the fluorescence screen, the camera was switched to a single-lens reflex camera (Nikon D5300) with a 18 - 55 mm objective lens, properly focussing the camera slightly behind the screen to reduce the influence of the grid of the fluorescence screen on the data quantification. As the sample heater creates background radiation which changes with its temperature, which can affect quantification of temperature dependent studies, a green filter (figure 2.4b shows its transmission spectrum) is mounted in front of the

objective lens. Measurements were automatized for linear heating ramps, using USB tethering (*ControlMyNikon 5.4.98.99 Standard* (Tetherscript Technology Corp.)), manual focussing onto the spots with the objective lens, temperature series recorded using an iso-value of 1000, an aperture of f/5.6 and a shutter opening time of 0.5 s and recording 0.2 frames per second to synchronize with a 0.2 K/s heating ramp and a filament current of 2.1 A. In order not to exceed the available RAM (and thereby stopping the measurement series), the file format is set to "JPEG size S".

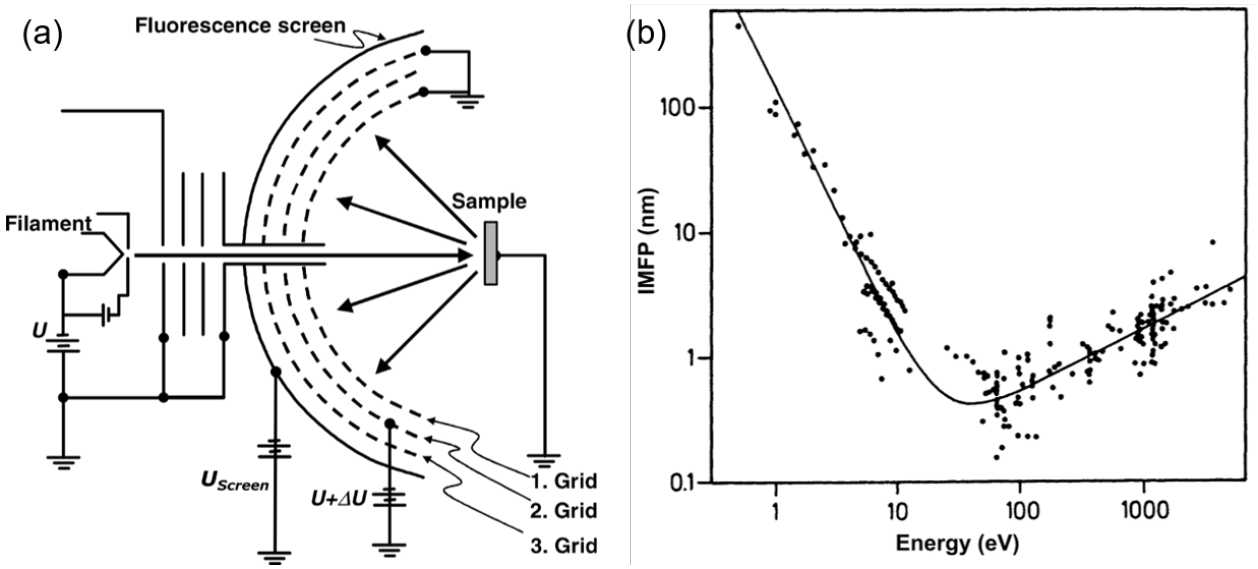

Figure 2.3: (a) A typical 3-grid LEED optics as used in this thesis reproduced from Ibach [118]: Electrons of controlled energy are directed orthogonally onto the sample. The diffracted backscattered electrons are visualized with a fluorescence screen where a high voltage potential (U_{Screen}) is applied. A voltage potential applied at the second grid (suppressor grid) lowers the background from inelastically scattered electrons. (b) The universal curve gives an estimate for the inelastic mean free path (IMFP) of an electron. It is dependent on the electron energy. This curve shows experimental data for elemental solids. (a) Adapted by permission from Springer Nature: Structure of Surfaces by H. Ibach, Copyright 2006. (b) Reprinted with permission from *Surface & Interface Analysis* **1979**, *1*, 1. Copyright 2004 John Wiley and Sons.

Beam damage from the electron gun was observed when measuring with the maximum filament current at high temperatures for the study of the high-temperature phase transition in section 4.3. To mitigate this, a compromise value for the filament current of 2.1 A has been established, where no beam damage in LEED was observed during the timescale of the measurements presented here while still maintaining a high enough spot intensity for quantification.

For data quantification, the grid of the fluorescence screen needs to be accounted for. Fitting line profiles would require blurring of the images, as using a wider line width for the profile does not solve this because of the periodic nature of the grid. However, when looking at data for spots at very low diffraction orders, they have the advantage of a greater width on the screen, spanning enough grid points that the influence of the grid becomes negligible when integrating the intensity of the spot. Low diffraction order spots have the additional advantage that the influence on the spot intensity by the Debye-Waller factor is reduced so much that it does not significantly change the determination of the transition temperature of the high-temperature phase transition of the $Fe_3O_4(001)$ surface in chapter 4.3. There, the (1/2, 3/2) spot is used at 25 eV is used, since the (1/2, 1/2) spot could not

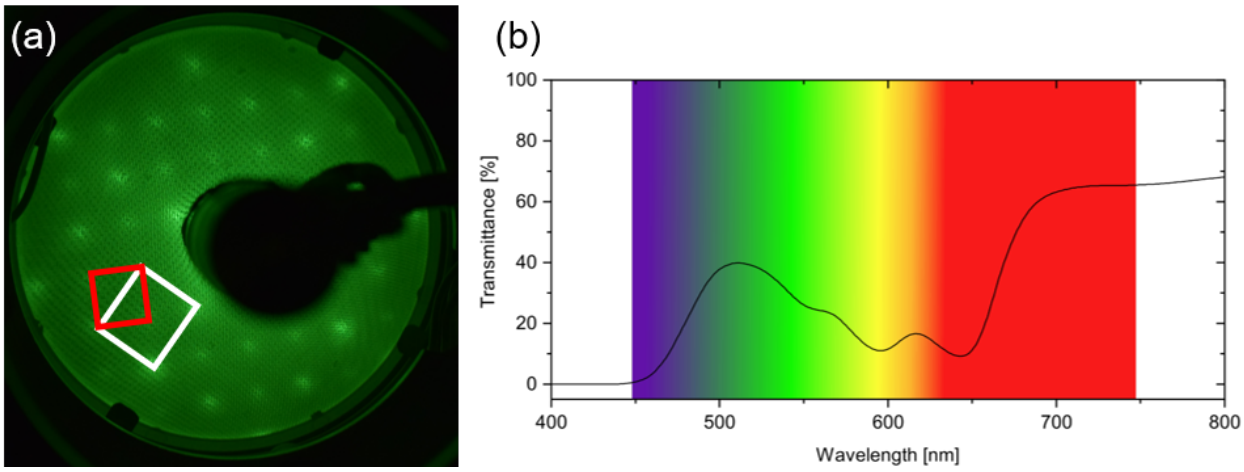

Figure 2.4: (a) Typical LEED pattern of the $\left(\sqrt{2} \times \sqrt{2}\right)$ R45° -Fe_3O_4(001) surface at an incident electron energy of 70 eV. The $\left(\sqrt{2} \times \sqrt{2}\right)$ R45° unit cell is indicated in red, the (1×1) unit cell is marked in white (b) Transmission spectrum of the green filter used for LEED measurements with corresponding colours in the background. The spots on the green fluorescence screen are imaged while background from the heater behind the crystal is reduced.

be image due to the relative size of the electron source in the instrument used. A Matlab script has been created that allows the manual placement of a circular mask for each spot of interest on the first image, and those masks are used automatically for all images of the data set. The intensity of the spot is numerically integrated for each image. A temperature read-out using the same computer as the camera tethering software provides an precise correlation of the sample temperature to the time stamp and thereby allows the assignment of a precise temperature to each image taken of a LEED pattern.

2.3 Temperature-Programmed Desorption and Mass Spectrometry

Temperature-programmed desorption (TPD), first described in the 1940s [119], is an integral tool for surface analysis, giving high-sensitivity information about the existence of one or more adsorption sites and the thermal properties of adsorption and desorption for a given molecule. It probes the adsorption and desorption properties of probe molecules like CO or reactants and products of reactions on the surface. One TPD cycle in principle consists of the dosage of a defined amount of probe gas molecules at or below the start temperature, placing the sample below a quadrupole mass spectrometer, and measuring the detected ion currents for characteristic mass/charge ratios while heating the sample with a heating rate $\beta = \frac{\delta T}{\delta t}$. The Polanyi-Wigner equation describes the desorption rate r_{des} as

$$r_{des} = -\frac{\partial \theta}{\partial t} = \nu_n \theta^n exp\left(-\frac{E_{des}}{RT}\right) \tag{2.4}$$

$$\tag{2.5}$$

with ν_n being the pre-exponential factor of the process of order n, T being the temperature, t being the time, E_{des} the desorption energy, and θ the surface coverage. Assuming a constant heating rate gives equation 2.6

$$r_{des} = -\beta \frac{\partial \theta}{\partial T}. \tag{2.6}$$

Dependent on the system, one or many more peaks appear, as shown in an example in figure 2.5. Higher coverages of adsorbed molecules lead in some cases to surface reconstruction (as described in section 1.3), thereby influencing the resulting TPD spectrum. Therefore, coverage dependent TPD measurement as shown in figure 2.5 can give additional information. Molecules with similar mass or multiple possible sources for a certain mass-to-charge ratio can be distinguished through isotopically labelling or different cracking patterns. The whole range of tools of thermodynamics and kinetics can be applied on TPD. More detailed information on TPD evaluation can be found in the literature, e.g. [101, 120].

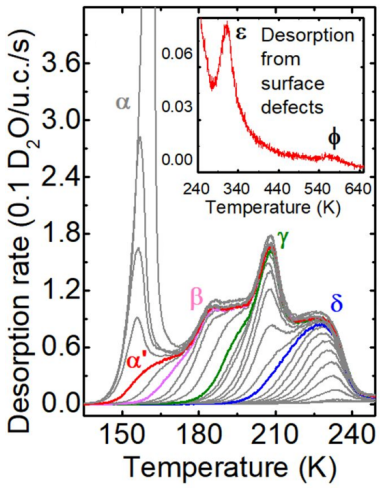

Figure 2.5: Temperature-programmed desorption of D_2O on $Fe_3O_4(001)$ with the higher temperature range shown in the inset. Six main peaks are observed (greek letters). Coverages from 0 up to 14 molecules per unit cell are used. Isotopically labelled water excludes any contribution of water from the residual gas atmosphere. Reproduced under PNAS License from *Proc. Natl. Acad. Sci.* **2018**, *115*, E5642–E5650.

2.4 Experimental Setup and Sample Preparation

The experimental setup used in this work is shown in figure 2.6. It contains three main parts which are described in this section: the STM chamber, the preparation chamber, and the laser-ablation cluster source.

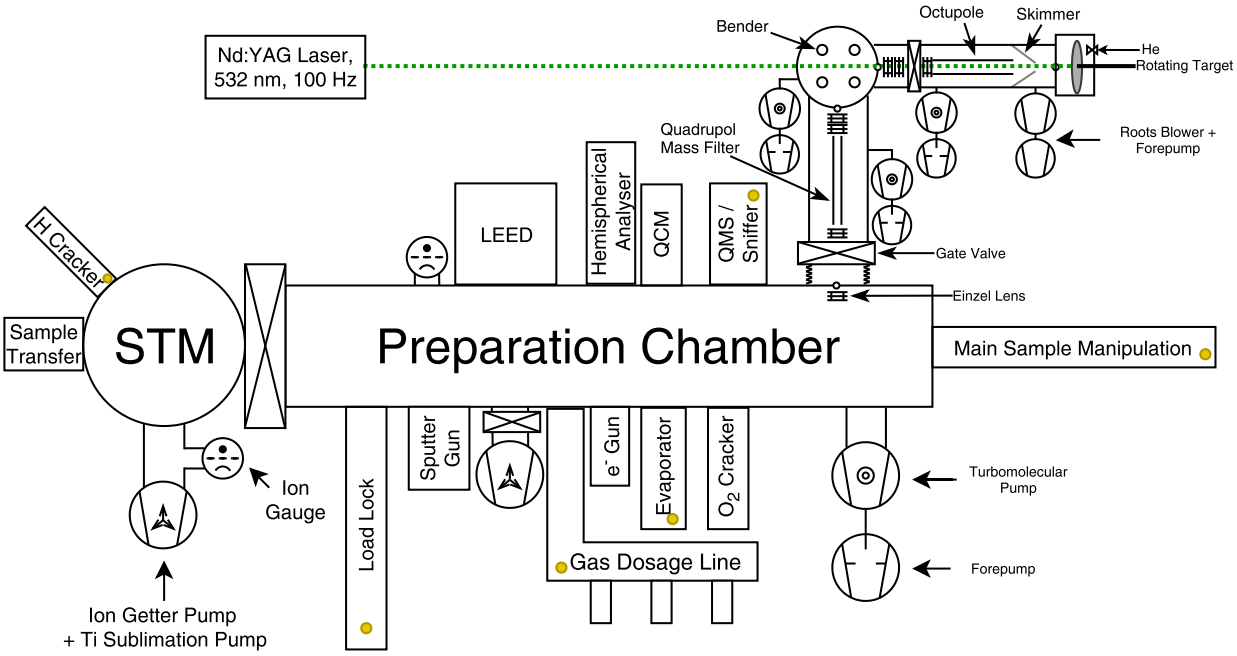

Figure 2.6: Schematic representation of the experimental setup. A yellow circle indicates additional pumping for this instrument. The angular orientations in the schematic are not representative.

STM Chamber

The STM chamber houses the commercial Omicron VT-AFM microscope capable of STM and atomic force microscopy (AFM). A wobblestick allows the sample to be transferred from the main sample manipulator to the microscope. The STM chamber can be separated from the preparation chamber by a gate valve, while the UHV conditions are maintained by an ion getter pump/ titanium sublimation pump assembly and monitored by a hot-cathode gauge. The base pressure in the STM chamber is 2×10^{-11} mbar. A hydrogen cracker in line of sight of the tunnelling junction has been built during this thesis with the goal to investigate a possible isotope effect on the switching motion of hydrogen adatoms. Therefore, deuterium atoms were dosed onto the surface during STM measurements to distinguish hydrogen adatoms and deuterium adatoms. This was not successful, as tip shadow effects prevented the deuterium atoms from reaching the surface while scanning.

Preparation Chamber

The preparation chamber contains all tools for sample preparation, integral characterization methods and a gas dosing system.
Connected to the preparation chamber is a load lock which can be separated from the preparation chamber and vented. Thereby, samples can be separately evacuated and than introduced to the

main sample manipulator in the preparation chamber. This manipulator can move the sample in x,y, and z directions and rotate around its axis and thereby access all instruments mounted on the chamber as well as a handover to the wobblestick in the STM chamber. Sample heating is performed by a boron-nitride heater placed directly below the single crystal and the sample temperature is measured by a thermocouple type K attached to the rim of the top-hat shaped crystal. Sample cooling can be done through a Peltier type cooling system with gaseous nitrogen. Gases can be dosed via multiple leak valves mounted on the gas dosage line. An ion source supplied with Ar gas is used as a sputter gun for sample preparation. A quadrupole mass spectrometer for residual gas analysis, TPD measurements, and leak testing is mounted on the chamber. It has been replaced by a sniffer instrument, containing a QMS of its own, as a part of this thesis which will be described in chapter 3.3. An electron gun combined with a hemispherical analyzer allows cleanliness checks through Auger electron spectroscopy (AES). Electron diffraction optics allow the investigation of the long-range structure of the sample by LEED. An evaporator, a quartz crystal microbalance for controlled evaporation, and an oxygen cracker are mounted as well. The UHV conditions are maintained by a turbo molecular pump (Pfeiffer HighPace 300M) - coupled with a rotary vane pump for the necessary prevacuum - together with a combined ion getter and titanium sublimation pump and monitored by a hot-cathode gauge. Differential pumping is supplied as necessary to the gas dosage line, the load lock, the evaporator, the main sample manipulator, and the sniffer. Another gate valve followed by a stack of einzel lenses separates the preparation chamber from the cluster source. The base pressure in the preparation chamber is 2×10^{-10} mbar.

Cluster Source

A cluster source as described by Heiz et al. [51] is attached to the preparation chamber. A pulsed high-frequency Nd:YAG laser ($\lambda = 532$ nm) is focused on the rotating metal target creating a metal plasma. A piezoelectric valve pulsing helium gas synchronized to the laser thermalises the plasma. Subsequently, the clusters undergo supersonic expansion into vacuum through a nozzle. After the skimmer, the cluster beam is guided by an octupole ion guide and electrostatic einzel lenses to the bender. The bender separates the desired, positively charged clusters from the neutral and negative ones. Further einzel lenses guide the cluster beam. A high-resolution quadrupole mass spectrometer is subsequently used to perform the mass selection. A retarding potential slows the clusters down to ensure soft-landing conditions. In order to bridge the pressure difference from some mbar in the expansion region to 10^{-10} mbar in the preparation chamber, a roots blower with a forepump and three turbo molecular pumps with corresponding forepumps (at the quadrupole, the bender and the octuple) are used. The base pressure in the quadrupole section is 5×10^{-9} mbar, 1×10^{-8} mbar in the bender section and 1×10^{-6} mbar in the octupole section for a non-baked cluster source. The octupole and expansion section can be separated from the bender and quadrupole section via a gate valve, thus ensuring best vacuum conditions in the latter.

Sample Preparation

Sample preparation has been done in the preparation chamber through repeated cycles of argon sputtering for 5 min (1 keV, 5×10^{-6} mbar Ar, normal incident) and annealing (983 K for 20 min).

Due to the sensitive stoichiometry of the Fe_3O_4 single crystal surface, it is important to make sure the Ar and O_2 lines are always kept clean. Every fifth sputter-annealing cycle, the sample is annealed in oxygen (1×10^{-6} mbar O_2). The oxygen annealing is important for the stoichiometry of the surface and gives the $\left(\sqrt{2} \times \sqrt{2}\right)$ R45° -Fe_3O_4(001) surface shown in figure 2.7b. Without sufficient oxidation, the surface shows the Fe-rich so-called "Fe-dimer" termination as displayed in figure 2.7a. To obtain a flat surface and prevent island growth, the sample should be cooled down in UHV after oxidation. Upon dosage of atomic hydrogen onto the surface, a Fe-rich surface shown in figure 2.7c was found, which resembles the Fe-rich surface from figure 2.7a.

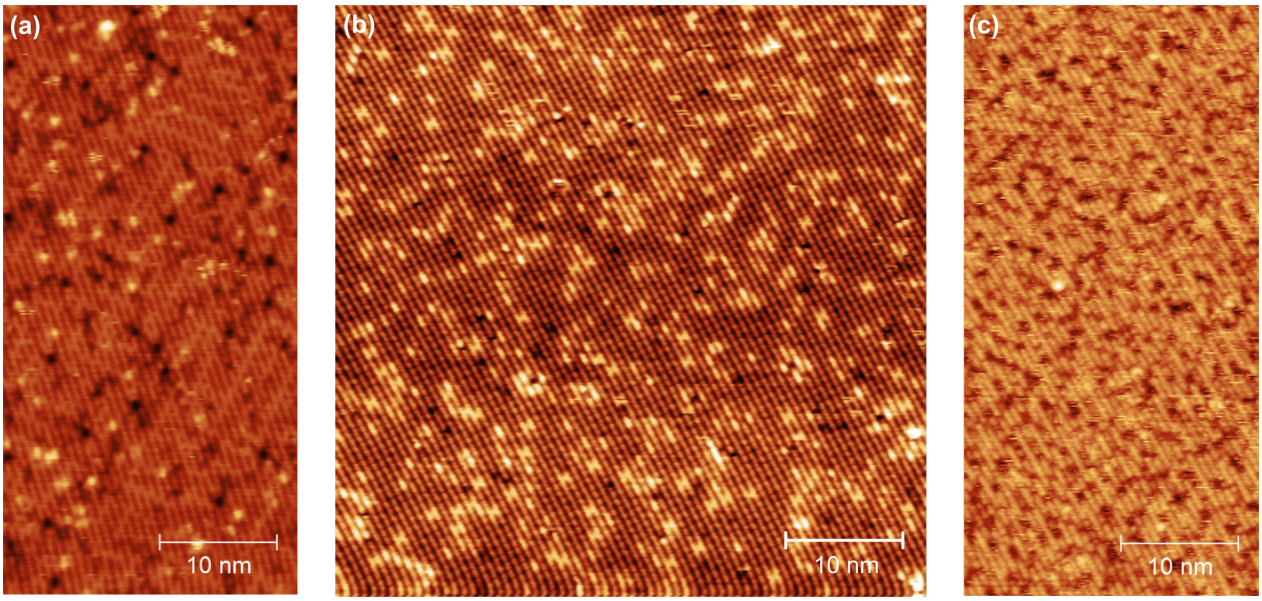

Figure 2.7: Examples of surfaces observed dependent on sample preparation of the (001) facet of the Fe_3O_4 single crystal. (a) Annealing in UHV results in an Fe-rich surface called "Fe-dimer" surface [20]. (b) After annealing in oxygen, the $\left(\sqrt{2} \times \sqrt{2}\right)$ R45° -Fe_3O_4(001) surface [72] studied in this thesis is obtain. (c) Dosage of atomic hydrogen leads to a Fe-rich surface similar to the one obtained through UHV annealing (U_b = 1.5 V, I_t = 0.3 nA).

3 Technical Innovations and Software Development

In this thesis, three main technical challenges have been tackled. The conversion of FastSTM movies (chapter 3.1), their quantitative evaluation (chapter 3.2), and the development of the Sniffer, an instrument for highly sensitive measurements of surface reactivity and catalysis (chapter 3.3).

3.1 pyfast - A Python-based Script for FastSTM Movie Conversion

The FAST module generates 1D data strings which have to be converted to 2D movies. This is performed by a *python* script, "pyfast". Pyfast is a common project with the CNR-IOM Laboratorio TASC, Trieste, Italy, and Catalan Institute of Nanoscience and the Nanotechnology (ICN2), Barcelona, Spain, administered via a Gitlab repository (https://gitlab.com/faststm/pyfast/) and coordinated by Carlo Dri of CNR-IOM. During this PhD thesis, three internship students, Jakob Filser, Frederic Felsen, and Karl Briegel, contributed significantly to the programming of the pyfast improvements and helped me to establish efficient conversion routines for FAST measurements on a daily basis.

Goals for the Pyfast Script - Job Description and Challenges

The FAST module records fast scanning probe movies and saves them in a tailor-made *.h5*-based file format as one-dimensional data string together with measurement metadata. The metadata includes information necessary for the correct data conversion like pixels in X-/Y-direction, measurement frequencies, estimated phase shifts in the X, Y, and Z signals from the FAST-Labview software (see section 2.1.2) as well as information that is useful for further data processing and analysis as time, sample temperature, bias voltage, tunnelling current, and excitation voltage for the X and Y direction. The task of this python script ("pyfast") requires much more than a simple transformation of the 1D data string to a 2D movie: Included are as well filtering of non-physical frequencies in Fourier-space, finding the exact phase shifts of the data, combining the forward and backward frames to create enhanced pixel resolution through interpolation, correcting for the creep of the piezoelectric scanner, correcting the movies for thermal drift in the movies, and finally exporting the movie and its frames with chosen export settings.
While at the beginning of this thesis the simple conversion to a two-dimensional movie with a simple decosination in X direction were implemented, the pyfast script was stepwise upgraded by a new interpolation function at the heart of pyfast, creep correction, drift correction, algorithm optimizations for stability and speed (X phase correction, interpolation), data improvement by frequency filtering, and tensor export as *.p* file.

Structure of the Data

Since the tip scans the surface in a fast sinusoidal movement in X and a slow triangular movement in Y direction, a movement as indicated in figure 3.1 results. Based on the movement, a FastSTM *measurement image* can be decomposed into four *measurement frames*: up-foward (uf), up-backward (ub), down-forward (df), and down-backward (db). By proper interlacing f and b lines, the interlaced *movie frames* can be generated as upward-interlaced (ui) and downward-interlaced (di) that can improve the spacial resolution. Based on this scheme, FastSTM movie outputs can either contain sets of up-forward/down-forward (udf) respectively backward (udb) or upward-interlaced/downward-interlaced (udi) frames - or only subsets (ui, di, uf, df, ub, db) - and is in the following labelled accordingly. The *frame rate* is the number of up/down movements per second (frames per second, fps), thus the dithering frequency. Therefore, one *image* contributes with maximum two frames to a movie, as forward and backward images represent the same time range. Consequently, the maximum measurement frequency of FastSTM measurements is two times the Y scanning frequency.

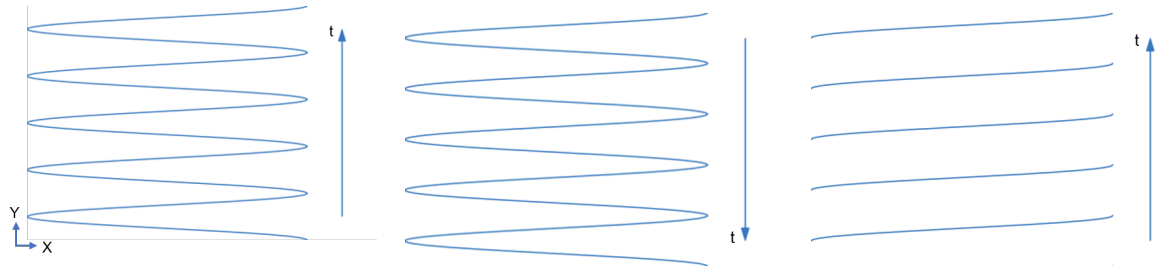

(a) upward movement **(b)** downward movement **(c)** extracted uf data set

Figure 3.1: Schematic representation of the 2D tip movement in (X,Y) space first upwards (a) and than downwards (b). To create processable data in matrix shape, lines and rows have to be determined. Exemplarily, the up-forwards lines are extracted in (c). Figure adapted with permission from [121].

X Phase Shift - How to Determine when the Frame Starts

Since the FAST module records data by exciting the piezoelectric scanner in a pendulum motion close to eigenfrequencies of the scanning system, the precise starting pixel of the first frame is not known and phase shifts may occur. Therefore the number of pixels in X and Y direction are set in the measurement, with a perfect synchronization between scanning motion and tunnelling current data acquisition, and can be read from the metadata. A good starting point for the X phase shift is usually the value determined during the measurement in the image preview of FAST-Labview, but it tends to be off by a small number of pixels. Even a misalignment by one pixel leads to serious misalignment of the rows in interlaced images, and a non-perfect X phase correction makes steps later in the conversion process even more tedious, particularly the creep correction. A first method to correct for this uses an empirically *X phase correction*, which works nicely for a limited amount of movies. This can be time consuming for a big data set or movies with mediocre contrast quality, when minimal changes have to be checked by eye repeatedly. An automatic approach has been developed that uses the line-wise autocorrelation of Gauss-filtered, Hamming-windowed subsequent

up and down frames as a function of different single digit values for the phase correction to determine the best one automatically. Thereby, a smoother processing is helped and the empirical user input is reduced in most cases.

Pendulum acceleration effects - Creep Correction

In FastSTM measurements, even the slow triangular movement in Y direction may lead to problems: the acceleration imposed at the reversal points cannot be followed by the piezoelectric scanner. This leads to an offset between up and down images due to delays. The difference between the electronic signal applied at the scanner tube and the actuated movement of the scanner is the creep of the piezoelectric scanner tube as shown schematically in figure 3.2a and has to be corrected for by a creep correction algorithm in order to exploit the full measurement data set. The correction is currently performed by a cubic Bézier function [122, 123] - mapping the pixels on their real Y positions - and control points are chosen as follows: The first control point P_0 is the starting point of the ideal tip path shifted by $pixels$. This shift is the correction necessary to correct for the hysteresis of the tip movement as shown in figure 3.2b. The last control point is the point on the ideal tip path halfway between the top and the bottom of the frame. The definition of the remaining three point P_1 - P_3 is indicated in figure 3.3. The points P_2 and P_3 are located on the lines between the auxiliary point L_1 (positioned at the height of the first point of the real path projected onto the ideal path) and the first and last control point. Their position on those lines can be changed to accommodate different scanner parameters if necessary. Because this method needs empirical input from the user for each movie in order to correct e.g. the hysteresis of the scanner movement, it is not very reliable for automatic data processing. The current determination of the scanning movement Bézier curve can thus only be performed on images with sufficient contrasst in Y direction (e.g. diagonal or horizontal Fe rows on magnetite). But once the parameters have been determined for a particular FAST measurement setting and tip state, they remain reproducible for this data set.
Currently, an improvement of the algorithm is being developed to substitute the Bézier curves with a sine curve that maps the transition from the static part $\left(\frac{dy}{dt} = 0\right)$ to the linear scanning regime $\left(\frac{dy}{dt} = \text{set scan speed}\right)$ with fewer and more intuitive parameters.

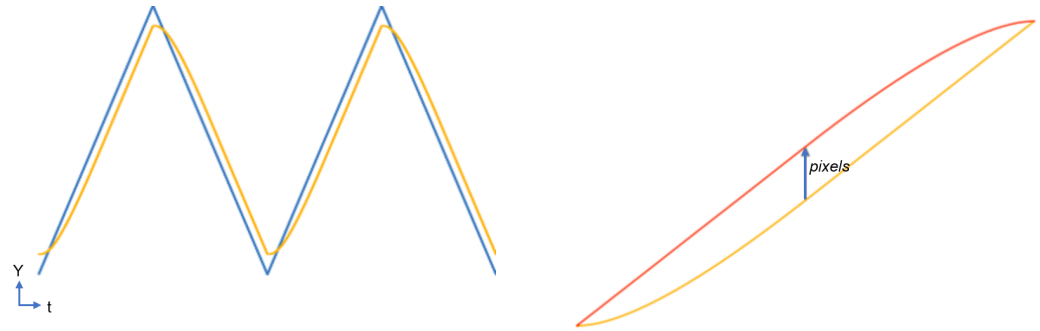

(a) (b)

Figure 3.2: (a) The ideal (blue) and non-ideal (yellow) movement in Y direction is shown here. The reason for this is the creep of the piezoelectric scanner when the triangular driving voltage in Y direction changes its direction (first derivative) at the top and bottom of each frame. (b) The hysteresis in Y direction of the scanner between up (yellow) and down (red) lines is shown. Shifting the traces by *pixels* along the trace is the first step in the creep correction. Figure adapted with permission from [121].

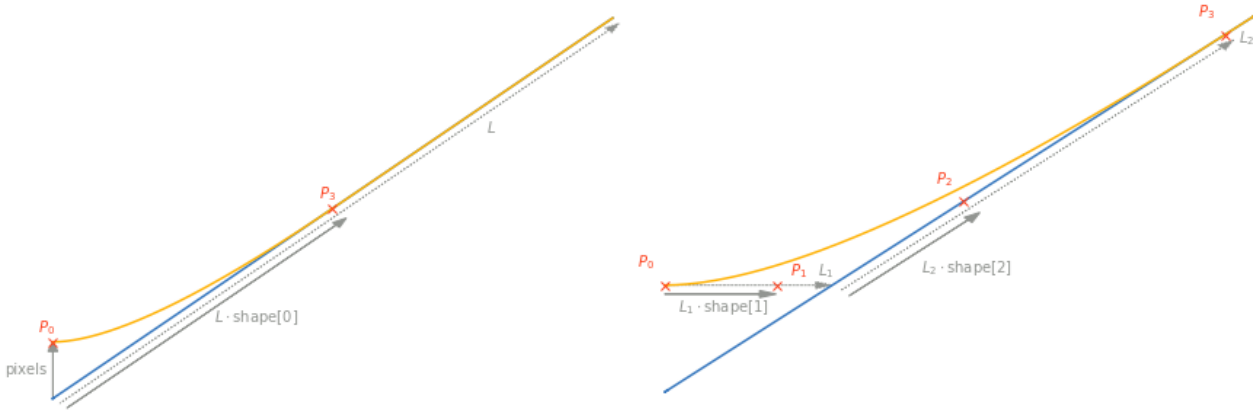

(a) (b)

Figure 3.3: The definition of the four control points P_0 - P_3 for the Bézier function for creep correction is shown here. (b) is zoomed in on the lower part of (a) to show be able to easier indicate the control points labelled here. Figure reproduced with permission from [121].

Turning the Sinusoidal Data into a Rectangular Movie - the Interpolation Function

In order to obtain spatial and temporal information in form of a movie, the tip moves in a sinusoidal movement over the surface and thus it does not have equally-spaced data points on a square grid. As figure 3.4 shows, its data points are non-equally distributed as the radial velocity of the pendulum motion of the tip is faster close to the centre of the image than at its edge. The data set needs to be interpolated to a grid in order to be processable. The easiest way for pure forward or pure backward channels to achieve this is to linearly interpolate in Y direction first (termed ”half-pixel correction” in pyfast) and to interpolate either by weighting (correlating each pixel before to each pixel after interpolation, ”accurate decosination” in pyfast) or by spline interpolation (”quick decosination” in pyfast) each row to create equally spaced pixels. Using the enhanced resolution of combining ’f’ and

Figure 3.4: Schematic representation of the tip movement (blue) and an equally-spaced grid for interpolation (yellow). Figure adapted with permission from [121].

'b' rows to interlaced rows requires an interpolation onto an equally-spaced 2D grid instead of the two-step process for 'f' or 'b' type data channels. This is achieved via a process called *"Delaunay Triangulation"* [124, 125]. It uses a set of triangles that only contain measured data points as corners (as shown in figure 3.5). The three closest surrounding measurement points determine the intensity of the interpolated pixel, weighted by distance. As the position of each data point is constant for each frame due to the perfectly periodic tip movement, the grid built for the interpolation can be used for the whole movie. This saves a large share of computation time enabling from approximately 20 minutes for converting one movie down to almost real-time data conversion.

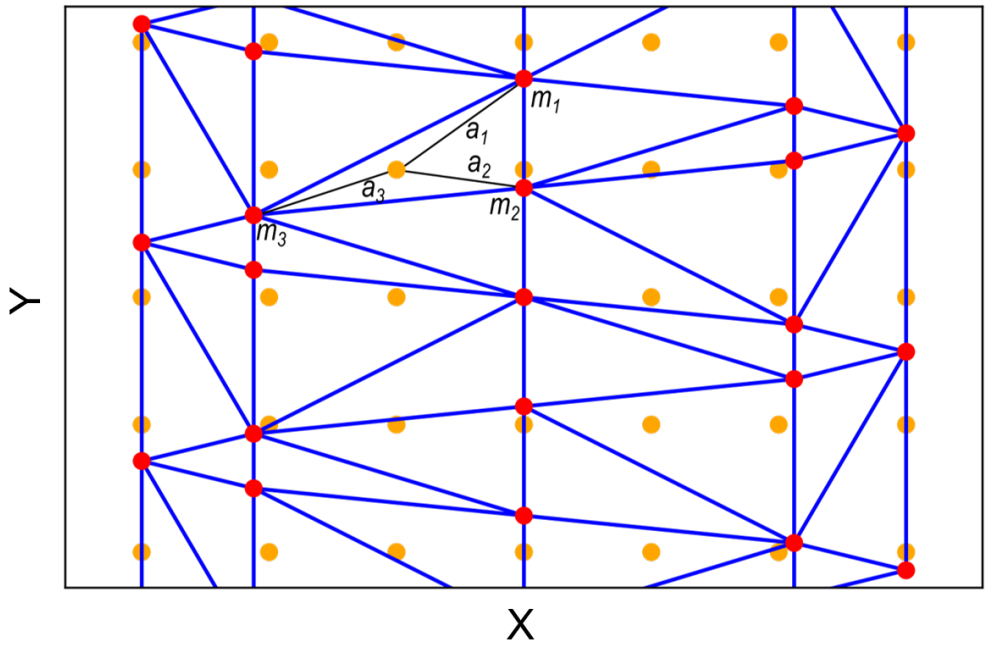

Figure 3.5: Illustration of the Delaunay Triangulation based on the measured data points (red) and the grid points (yellow). Each grid point is defined uniquely by its surrounding triangle and can be calculated by weighting the tree corners (m_1, m_2,m_3) with the distances to the grid points at the centre of the triangle with the reciprocal distances (a_1, a_2, a_3). Figure adapted with permission from [126].

Frequency Filtering

STM measurements are sensitive to vibrations in the setup and care must therefore by taken to mechanically isolate the microscope from the rest of the setup and remove or block components that could cause noise in the signal. Since some minor noise sources (e.g. rotational frequencies of the turbomolecular pumps) sometimes remain, these noise frequencies need to be removed by filtering the FAST signal in the time domain. To this purpose, the whole data string is transformed into a frequency spectrum and back by Fourier transformation. This process is computationally demanding and the RAM size of the computer limits the maximum convertible file size.
As a standard practice, the following filtering operations were performed on the movies:

- The X Scanning Frequency and its Overtones: The X scanning frequency itself and its overtones are filtered out, which corrects for tilt of the topography in X direction because of the tip shape.
- Signals Slower than the Y Frequency: Any measured frequencies slower than the Y frequency of the movie cannot be a result of the regular topography. Consequently, a high-pass filter filters out all frequencies below and equal to the Y frequency.
- Eliminating Single High Peaks: Single, sharp, disproportionally intense peaks can sometimes be observed for the rotation frequencies of the turbo molecular pumps and the corresponding overtones, which are usually filtered. Their amplitude is dependent on the quality of the tip.

One optional filter - selectable by the user - is implemented and can be used dependent on application.

- Removal of Noise Floor: If desired, the noise floor of the movies can be reduced by filtering the median frequency from movie as the real information is usually represented in sharper peaks. This can cause problems for movies with mostly mobile species imaged at high temperatures and reduces the temporal resolution as it effectively includes some temporal averaging as well.

Introduction of Drift Correction

Thermal drift is a permanent issue in all scanning probe measurements [127, 128] at elevated temperatures. Even minuscule temperature gradients can result in drift on the order of fractures of a nm/s, which can create a problem as usually it is desired to image the exact same region over time. There are two strategies to both applied to meet this challenge: First, minimizing the drift by proper correction by hand with the *MATRIX* software standard method. In addition, the movie is drift-corrected "post-measurement". By calculating the drift for two (or more) images that differ by a certain amount of time (typically 20 s in order to overcome subpixel drifts), drift traces can be calculated for the whole movie. The drift correction is than applied either by displaying the part of the movie that is present in all movie frames ("greatest common" method) or by presenting the complete dataset and filling the patches of the movie with zeros ("full" or "maximum area" method), where there is no data at a given point during the movie because the tip is not yet/ anymore there.

Exporting Movies to Useful Formats

Finally, the measured movie is exported for further data analysis and presentation. Movie and frame output are created using FFmpeg [129]. The following exports are possible:

- MOVIE: The data is exported as movie file (*.mp4* or *.avi*) using matplotlib [130] colormaps (e.g. "hot" or "inferno") to represent the data. The movie can be accelerated from real time by an acceleration factor, exported with timestamps and frame descriptor, exported only for a certain range of images, and scaled in X and Y directions. The files here can be operated with any standard program and processes with dedicated scripts.

- FRAMES: For presentation in print, geometric and static analysis, and further data treatment with other software packages like Gwyddion [128] or ImageJ [131] and plugins hereto [132, 133], the data can be exported as image files. The data representation can be chosen like for movies. If desired, the average of subsequent frames can be output. Output formats include *.png*, *.jpg*, and *.gsf* (*Gwyddion Simple Field* file format [128]).

- TENSOR: For easier data processing with multiple python-based *Jupyter* notebooks, the movie is stored as *pickle* file (*.p*). It contains three elements: First and foremost, the data of all frames are contained as three-dimensional array. The second element is the desired video rate of the output (*fps* factor) of the exported movie. The third element is the range of images selected for exportation as movie (*image range*).

- METADATA: The metadata dictionary is written to a .txt file at the end of the export, while a log file of the processing steps taken for this specific movie is exported as well.

3.2 Quantification of FastSTM Data

The quantitative analysis of FastSTM movies can help unravel details such as diffusion paths and residence times. To this purpose, it is desirable to extract reliable spatial and temporal information. While the temporal evaluation is best demonstrated by means of an example given in chapter 4.1, as it is very case specific, the spatial evaluation is discussed in more detail in the following.

Spatial Calibration of FastSTM Data

As already mentioned, FastSTM takes place with the fast scanning frequency close to the first eigenfrequencies of the scanning system. A proper characterisation of these eigenfrequencies can be performed by measureing the logarithmic tunnelling current response in tunnelling contact upon stimulation of the piezoelectric scanner in X, Y and Z direction (shown in figure 3.6). While at low frequencies a correct signal is measured, at high frequencies eigenfrequencies of the scanning system get excited, leading to increased tunnelling currents upon X, Y excitation due to residual sample inclination, while Z excitation leads to both kinds of responses, increase and decrease in the logarithmic tunnelling current.

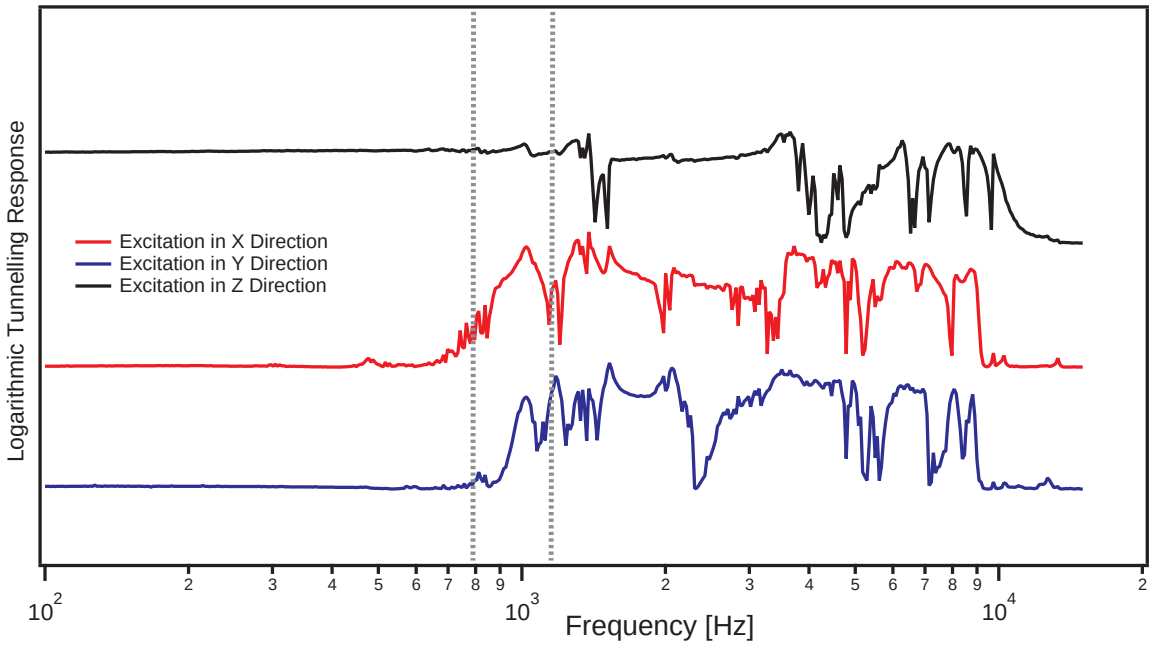

Figure 3.6: Tunnelling Response when exciting the piezoelectric scanner in the fast, slow scanning directions and the Z direction in tunnelling contact measured using the method described in Dri et al. [134]. The grey, dashed lines indicates the X frequencies of the most common measurement settings (785 and 1147 Hz) in this thesis. Figure is based on data measured jointly with F. Knoller [135].

The measurement conditions established for this thesis used fast-scanning direction frequencies indicated by dotted lines in figure 3.6 and listed in table 3.1. The region around 784 Hz provides a suitable frequency window for the FAST module as found together with Knoller [135]. The preamplifier of the microscope used for FastSTM measurements had a bandwidth of $\leq$80 kHz (gain 3x10^7, 330 nA range), above which it starts to act as an integrator of the current signal. Most pixel frequencies noted in table 3.1 are only slightly above the preamplifier bandwidth of 80 kHz and

are suitable for measurements when the frames have enough pixels in the fast scanning direction. Figure 3.7 shows room temperature frames from movies using the frequency settings from table 3.1. The lateral size of the movie is regulated by the voltages driving the tip oscillation in X- (fast scanning) and Y- (slow scanning) direction and do not change the measurement frequency or the pixel frequency.

Table 3.1: Established measurement conditions for FastSTM measurements.

settings	frames per second (fps)	X frequency	pixel frequency	number of pixels
4 fps	4	785	153 846	196 x 196
8 fps	8	784	76 805	98 x 98
11.7 fps	11.7	1 147	112 360	98 x 98
19.6 fps	19.6	785	153 846	40 x 196

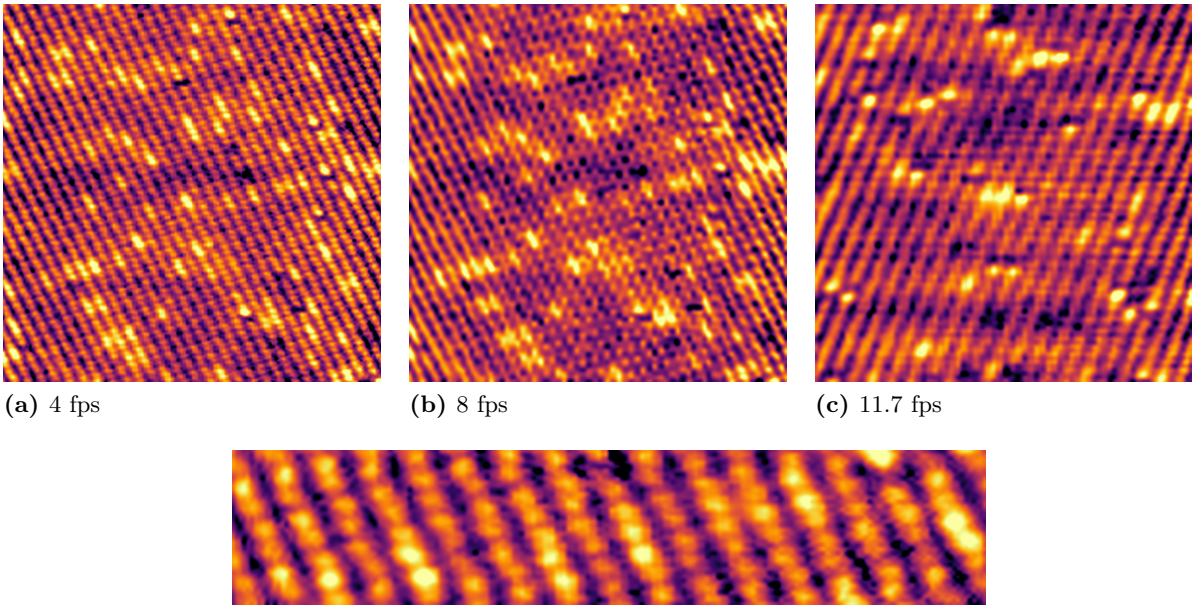

(a) 4 fps **(b)** 8 fps **(c)** 11.7 fps

(d) 19.6 fps

Figure 3.7: Frames of standard settings for FastSTM measurements for different time and length scales with the frame rate indicated below them for the measurement conditions in table 3.1.

While scanning at elevated frequencies, eigenfrequencies are hence partially excited, leading to coupling between X and Y directions and distortions. While those distortions can be reduced by proper choice of frequencies, residual effects need to be corrected for post-measurement.
The uncorrected frames presented in figure 3.7 can serve to provide quantitative information for the movement of features appearing already in conventional STM images (see chapter 4.1). When absolute angles and precise distances are required (as in chapters 4.2 and 4.3), the FastSTM frames need to be corrected in order to get correct information, as done exemplarily for the 4 fps settings with standard voltages for X (0.5 V) and Y (0.7 V) in figure 3.8. This is done using high-resolution frames of the SCV structure of magnetite (001) as shown exemplarily in figure 3.8. The $\left(\sqrt{2} \times \sqrt{2}\right)$ R45° reconstruction has a square unit cell, which should be obtained in the FFT image as well. The setting described above creates frames with a rhombic arrangement of the SCV spots. Measuring the devi-

ation of the angle from 90° gives the shearing angle, resulting in a rectangular alignment of the SCV spots (transformation between figure 3.8a and b). The ratio between the lengths of the two edges of the rectangle gives the Y/X stretching ratio that transforms the sheared frame so that its FFT image shows a square alignment of the SCV spots, therefore the relative lengths and angles are now correct. Care has to be taken to apply these corrections only in one of the two scanning directions, i.e. aligning the Fe rows with one edge (the bottom edge, for the values given here) before shearing and stretching. The fact that stretching on its own is not able to correct this error indicates that there has to be some cross-excitation between the fast and the slow scanning direction. This procedure can be tedious to perform for all frames and impossible for those without the resolution to recognise the SCV peaks in the 2D-FFT image. Using the same measurement setting should give the same scaling proportions of the movie as verified for multiple data sets in this thesis. In order to estimate the correction for the 4 fps setting described above without the influence of the crystal rotation, the data can be corrected by shearing of 11.5° and a Y/X stretching ratio of 1.137. The shearing angle can be in positive or negative direction dependent on the settings used for movie conversion in pyfast (see section 3.1, X phase correction) and can easily be checked by eye. This will give a good estimate of the necessary correction for most cases, while the protocol described before yields correct values even in the range below 1° and 1 %.

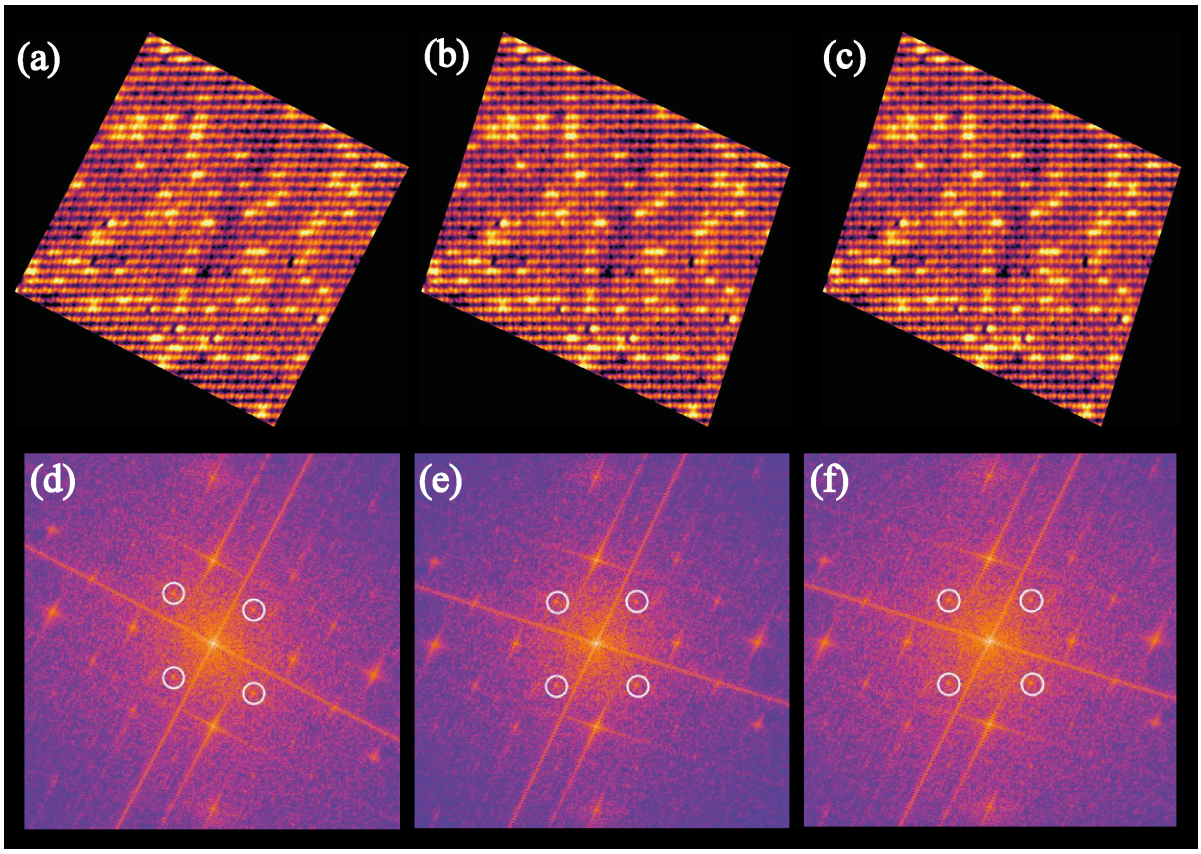

Figure 3.8: To get correct angles and lengths from FastSTM movies, it is necessary to correct the movies. The 2D-FFT images (d,e,f) of the atomically resolved $\left(\sqrt{2} \times \sqrt{2}\right)$ R45° -Fe_3O_4(001) surface (a,b,c) show four peaks for the SCV reconstruction (white circles), which form a square if the movie has been well corrected. Therefore, the rotated movie frame (a,d) is first sheared (b,e), and than stretched (c,f), as described in detail in the text.

The correct real-space length-scales can now be determined by trigonometry based on the row-to-row distance of 0.59 nm in the SCV model [72], the number of Fe rows intersecting with the frame border and the intersecting angle. The movie dimensions are highly dependent on the tip state and can change from day to day, so the real-space lengths need to calculated for every data set. When measuring at higher temperatures, the movie size does not change up to approximately 700 K, while a significant change in size is found at and above 750 K, as the piezo-electric scanner and the tip get warm which changes the real space dimensions of the scanned surface.

3.3 Sniffer - A High-Sensitivity Instrument for the Investigation of Surface Catalysts

This chapter provides information on the design, development, construction, implementation, characterization, and application opportunities of an instrument, the sniffer, providing the capability for highly sensitive kinetic measurements of catalytic reactions at pressures ranging from 10^{-10} mbar to 10^{-4} mbar over seven orders of magnitude. The sniffer instrument is capable of pulsed dosage from several hundred Langmuir (1 Langmuir describes dosing a gas with 1.0×10^{-6} torr $= 1.33\times10^{-6}$ mbar for 1 s [101]) to below 1% of one Langmuir, providing a wide range of dosage variation for possible experiments from titration of small amounts of reaction product on the surface to dosing several hundred Langmuir, creating an experimental environment closer to ambient conditions than most common UHV studies. This amount of reactant improves the sensitivity towards side products created only at minor shares and enables are more complete kinetic analysis including more side products.

Three main technical challenges were identified and subsequently used to develop design criteria for the instrument.

First, the instrument shall be capable to apply local pressures closer to ambient pressure at the surface of the sample, since this would allow the pressure-dependent creation of structures not visible at pressures common in UHV like particular oxide surfaces, which might show different reactivity than the low-pressure structures. On the other hand, the instrument shall still be integrated into the UHV setup, so that it can take advantage of the high control over the sample preparation in UHV and the surface characterisation techniques available. The setup therefore needs to be a hybrid one, having high-pressure capabilities as well as UHV compatibility. Consequently, it is desirable to apply the high pressure only to a very small volume in front of the sample, which can be isolated from the rest of the chamber, and have additional pumping for this volume, in order not to affect the whole UHV chamber.

Second, the product amount can be small, especially when studying size-selected metal clusters, since the cluster coverage needs to be low enough to still ensure monodisperse clusters after deposition. This requires a high precision of the reactant dosage and a high sensitivity of the detection. To achieve this, it is necessary to make sure all the product reaches the detector and the have a particularly low background.

Third, the instrument shall be capable to gain information on reaction kinetics and residence times of reactants and products on the surface. To achieve this, the reactant is dosed with pulsed valves, so the time-dependent behaviour can be monitored reproducibly.

Methods for Investigating High-Sensitivity Surface Catalysis

A first attempt to isolate a TPD instrument from a surrounding UHV was done by Feulner and Menzel [136], placing a glass envelope around the detector and having a sample-sized aperture at the front ("Feulner Cup"). Thereby, the detector only measures desorbing species from the sample and the inside of the glass envelope. In the instrument developed in this thesis, a stainless steel cone with a sample-sized aperture is used to create a small separate volume in which high local pressure

can be applied without affecting the surrounding UHV chamber. This also lowers the background level since only species from this small separate volume can reach the detector.
To obtain more information on kinetics, turnover frequencies, and catalyst stability, dedicated pulsed reactors in high-vacuum (TAP and TAP-2 reactors [137, 138]) were developed. Molecular beam experiments [139–142] enable experiments where each molecule only collides once with the surface. Judai et al. [143] employed a high-frequency piezo-electric driven valve for pulsed measurements in UHV. In that instrument, the crystal is brought as close as some centimetres to the QMS and the output of the pulsed gas doser in the UHV chamber. Inspired from the pulsed valves and molecular beam techniques, pulsed valve are used for the instrument developed here, and care has been taken to keep the tubing for the pulsed gases as straight as possible to avoid turbulences at kinks. Watanabe and Isomura [144] used a larger high-pressure cell using a circulation pump for gas flow in a different kind of instrument. The group of Harbich [145] in 2011 developed a UHV-compatible reaction cell called sniffer, which reversibly separates the sample from the surrounding UHV chamber and allows higher pressure pulsed experiments, which serves as a starting point for the development of the new instrument and shall be improved upon by measures discussed above and further below.

Development, Design, and Characterisation

The instrument developed within this thesis is based on the approach of the group of Harbich [145–147], while the pulse characteristics, the background level, and the resistance of the instrument towards reactive gases, shall be improved through modifications described in the following paragraphs. Since a larger-diameter flange of DN63 compared to Harbich's DN40 flange is available here, the base tubing diameter for the reactant tubes is increased to 4 mm from 3 mm and most kinks in the tubes are removed. This enables the transport more gas in the same time. Additionally, the larger cross-section makes pumping easier, which decreases the intrinsic pulse decay time of the instrument and thereby extends the window of observation towards shorter pulses. Particular focus for improvements has been put to avoid kinks in the tubing for the gas pulses, lower the background by leading the products directly to the detector and reducing the influence of desorption/adsorption processes at the pipes by making them out of fused silica and heating all of them to >370 K. Additional welded bellow-sealed valves enable the dismounting of the pulsed valves from the setup for bake-out or poppet exchange without breaking vacuum.

Principle Components

The general structure of the instrument is displayed in figure 3.9. Two pulsed valves (solenoid valves, Parker Series 99) create reactant gas pulses which are directed onto the sample first by stainless steel tubes and through a spacer (PTFE) to fused silica tubes on the vacuum side. From the sample, the product gas is lead straight to the QMS (PrismaPlus, Pfeiffer Vacuum GmbH) entrance through a fused silica tube. The gas flow is indicated with white arrows in figure 3.9. The instrument is isolated from the surrounding UHV chamber by a cone (stainless steel) and is pumped separately to a base pressure of 5×10^{-5} mbar by a turbo molecular pump, which is connected to a flexible tube fixed to the sniffer. Since the poppets of the solenoid valves are sensitive to temperature change

and the valves are not made to be used above 378 K [148], the possibility to dismount the solenoid valves without breaking the vacuum of the main chamber greatly enhance the workflow. Therefore, welded bellow-sealed valves (Swagelok, SS-4H-V51) are placed between the solenoid valves and the vacuum side. Furthermore, these valves are temperature stable (up to 588 K [149]) in the range of the bake-out temperatures (in this work: < 473 K) and therefore do not need dedicated cooling. The solenoid valve can therefore be mounted after a bake-out and heated separately to 378 K while pumped via their gas-lines to obtain a clean and water-free setup. Feedthroughs for electronics and thermocouples allow controlled heating and potential measurements.

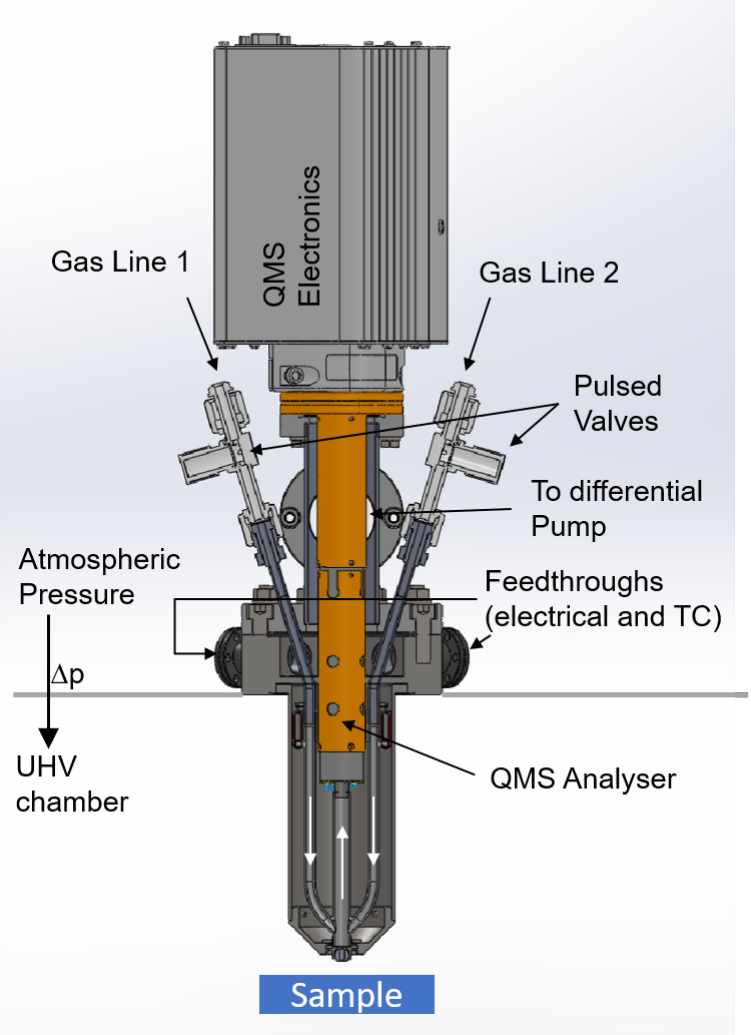

Figure 3.9: The Sniffer instrument uses two gas inlet lines with pulsed valves at their ends to direct defined gas pulses towards the sample. White arrows indicate the direction of the gas flow within the instrument through fused silica tubes towards the sample and therefrom to the QMS. A separate turbomolecular pump evacuates the Sniffer and avoids accumulation of gas during the measurements, improving time resolution of the pulses. To power the heating for the fused silica part and its control, one small flange contains electronic feedthroughs for the heating and another one contains thermocouple connectors for precise temperature measurement at the fused silica tube.

Ionization

The ionization section of the instrument is based on the open ion source configuration of the *PrismaPlus* (Pfeiffer Vacuum GmbH) quadrupole mass spectrometer. As the transient local pressure during the pulses can be higher than the usual pressures at open filaments, a stainless steel tube is inserted into the ionization region, having a slit at the height of the QMS filament as in the design of [146]. This allows sufficient electrons to enter the ionizer, while protecting the filament from being destroyed by the gas pulses. Additionally, this makes sure the filament does not interfere with the gas atmosphere. Still, at high pulse pressure, a transient decrease of the filament emissivity can be observed (see dips in pulse profiles in figure 3.13a). As the stainless steel tube seemed to react with reactant gas pulses over time, it was substituted with a similar part made from tantalum vacuum-annealed to 1173 K, which is more inert at high temperatures [64] as long as not too high O_2 or H_2 pressures are used. The tube is connected to the surrounding cage through spot-welding at the entrance of the ionization section to prevent charging of the tube.

Creating a Low Background Device

Deviating from the design of Harbich [146], all pipes on the vacuum side of the instrument are made from fused silica and do not have sharp kinks, to avoid contamination from pipes extracted from stainless steel by high-pressure gas pulses and avoid stretching of the pulses. The strong adsorption of water on the chemically more inert fused silica makes it necessary to have a dedicated heating method for the fused silica part to avoid contamination effects from water and reduce at any cost the background pressure level to drastically increase the signal-to-noise ratio. Multiple heating methods are possible. The latest version of the Harbich instrument [146] uses fused silica in the part of the central tube that is close to the ionization section, which is fit into a glass-ceramic tube with multiple parallel tubes for heating wire. This structure is not easily transferable to the full fused silica tubing, as it is rather space-consuming. Furthermore, porous ceramics can contribute to increasing the background level. Two methods for heating the fused silica part to above 372 K were considered here (shown in figure 3.10). The first approach uses tantalum wire wrapped around the fused silica pipes, which is shown in figure 3.10a. One wire is wrapped around the central tube and another one is wrapped around the two thinner side arms, enabling different heating control for both. Thermocouples measure the temperature close to the ”upper” end of the central pipe and one side pipe, and one is placed at the intersection of the three pipes. As long as the heating temperatures are not too high, the direct contact between the Ta wire and the fused silica does not seem to change the tantalum properties over time by reaction or other otherwise. A second approach considered uses radiative heating through tantalum wire wrapped around metal rods close to the fused silica pipes as the drawing in figure 3.10b shows. The cone separating the instrument from the rest of the vacuum chamber should reflect the heat. This approach has not been built, as it involves heating the whole instrument, thus creating an instrument that is hot from the outside as well. This could have adverse effects the other instruments and the vacuum system, and would require higher heating power to heat more material than the first approach.
The signal-to-noise ratio is influenced by two more topics: First, the dimensions of the slit for the electrons in the Ta tube can influence the detected signal. A larger slit increases the number of

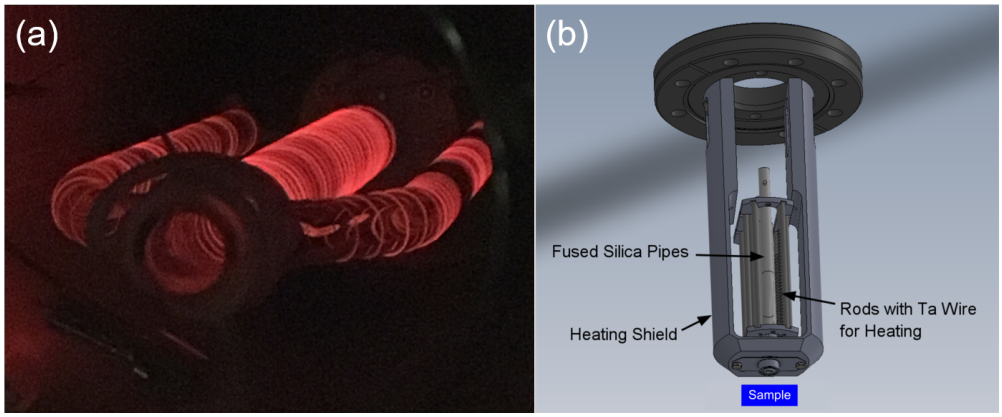

Figure 3.10: Heating methods considered for the fused silica pipes of the sniffer. (a) Contact heating via tantalum wires wrapped around the fused silica part at operation temperature. (b) Radiative heating method using tantalum wire wrapped around vertical rods and surrounded by a heating shield, which has not been built.

electrons available for ionisation, thereby detecting more ions and, consequently, more signal in the QMS. On the other hand, collision desorption from the interior of the tube can be increased with an increased number of electrons in the tube. Therefore, an optimum between those two influence has to be found. The slit in the current implementation has width of 0.5 mm and a length of 3.0 mm. Second, isotopically-labelled gases can improve the signal to noise ratio, since their background should be minor.

Distance Measurement through Electric Isolation of the Head

The instrument can be retracted from and moved into the preparation chamber of the setup via a Z transfer (ZLTM 11450HW, Vacgen Ltd). The sample is positioned in front of the instrument through the manipulation arm described in chapter 2.4. Two different instrument heads were implemented. One consisting of a pierced and flattened ball (ordinary steel) held by a spring into a stainless steel pod electrically isolated from the rest of the instrument by glass-ceramics similar to the original design [145, 146] and the other one being a cone made from fused silica. Both are shown in figure 3.11.

The first one enables an additional degrees of freedom to align the instrument inlet to the sample surface, as the manipulation arm can not control the angle along its long axis. Additionally, the distance between the head and the sample can be monitored by measuring the electronic conductivity between the sample and the electronically isolated instrument head. This design, however, necessitates a sharp edge narrowing the cross section of the tubing, which could reduce the amount of reactant to reach the sample surface directly by backscattering at the ball pod.

The other instrument head built from fused silica does have a truly conical shape. It was supposed to reduce backscattering of gases from the ball pod. As it is no longer made from electrically conducting material, the electric conductivity can no longer be used for quantification of the head-sample distance. Therefore, the sample positioning needs to be supervised optically through a viewport on the side of the preparation chamber. A camera with optical zoom (The Imaging Source, DMK 72AUC02) improves the precision and allows a convenient control. Figure 3.12 shows

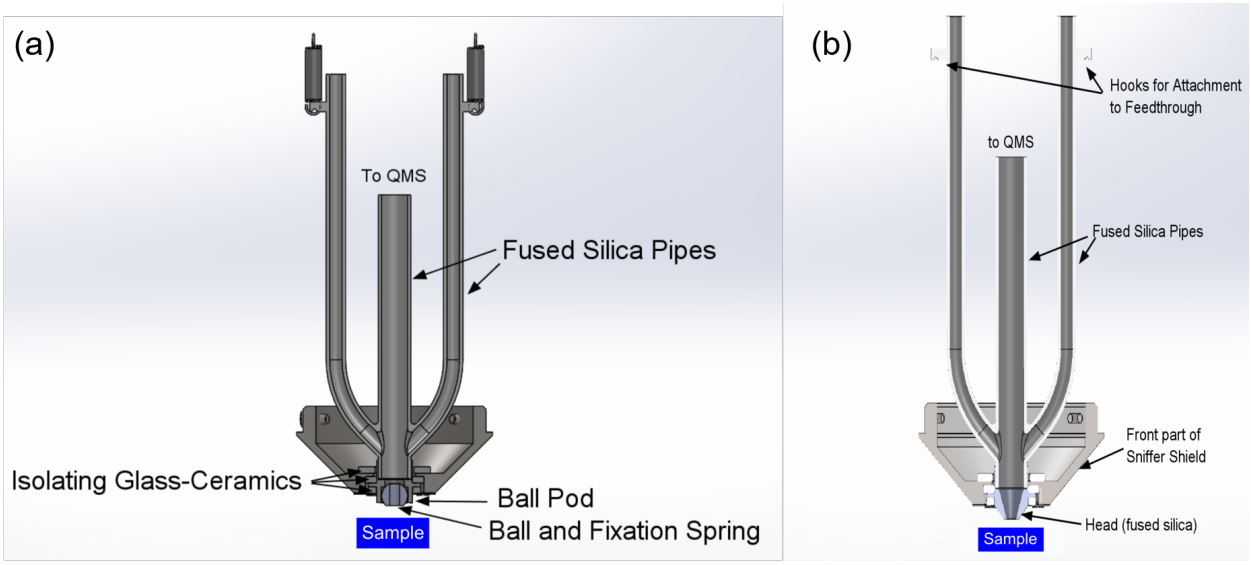

Figure 3.11: Zoom into the front part of the instrument (a) for the adjustable ball design and (b) for the fused silica cone design.

the fused silica cone above the sample in a slightly retracted position.

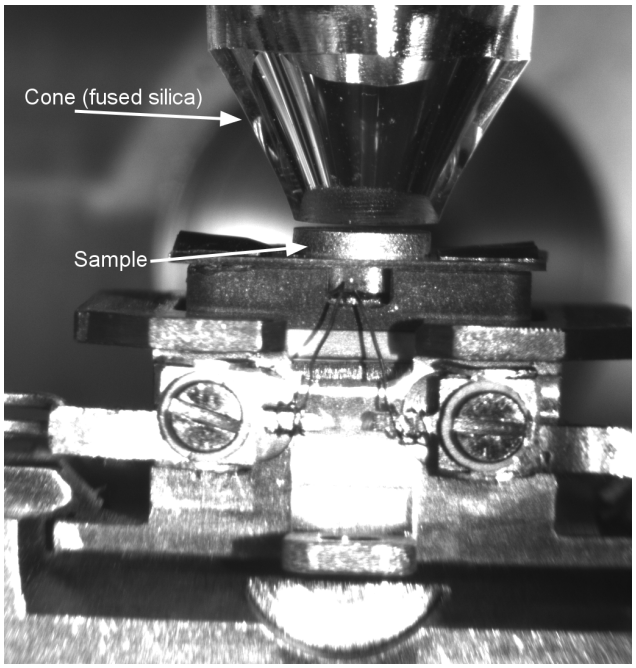

Figure 3.12: Fused silica cone at the head of the sniffer photographed with a slightly retracted sample.

Calibration and Pulse Shape Control

The pulsed valves used here are solenoid valves [150–153] are Parker Series 99 valves [148] with two different orifice sizes. The advantage of solenoid valves is that they are more compact than piezo-electric based valves. All Series 99 valves were controlled by a home-built Labview program via a digital-to-analogue converter connected to an amplifier. Thereby, pulse sequences with for both valves with different pulse heights and lengths can be repeated for a chosen number of cycles

or until stopped manually. A pre-pulse can be added to the pulse shape if desired, in case a steeper opening might be necessary. Ion currents from the QMS are related to local pressures by calibrating through backfilling the chamber. The first valves used here have an orifice of 2.95 mm, can be used of the shelf, and give highly reproducible pulses for a simple physical gas reflection experiment with elemental nitrogen gas using its 25 V opening voltage for 6 ms (the minimal time needed for this valve to shown reproducible behaviour) indicated in figure 3.13a with various pressures on the high-pressure side of the valve (0.02 - 1.00 mbar) and a Faraday cup detection. Comparing the pulses obtained shows that higher pre-pressure leads to higher and longer gas pulses at the QMS. When pulse heights above 3.5×10^{-5} mbar arrive at the QMS, the emissivity of the filament breaks down, leading to saddle-shaped pulse signal detection for pre-pressures above 0.1 mbar (while the actual pulse is likely higher and shaped similarly to the other pulses). The QMS signal is back at the baseline level after 1 to 3 seconds for these settings. Adding welded bellow-sealed valves between the vacuum side and the solenoid valve increases the FWHM of the pulse from 200 ms to 400 ms and stretches out the pulse shape, as displayed in figure 3.13b. Nevertheless, this pulse shape may be a acceptable cost for most applications for the well-being of the UHV chamber and the flexibility obtained thereby. Inverse mounting of this valve does not significantly change the pulse shape. Comparing the FWHM of pulse with an approximate transient pressure maximum of 4×10^{-5} mbar as in figure 3.13b to the instrument of Harbich [145] shows that for comparable transient peak heights, the FWHM of the pulse of 450 - 550 ms of the Harbich instrument [145] is longer than the 200 ms (without welded bellow-sealed valve) as well as the 400 ms (using the additional welded bellow-sealed valve) for the instrument built as part of this thesis.

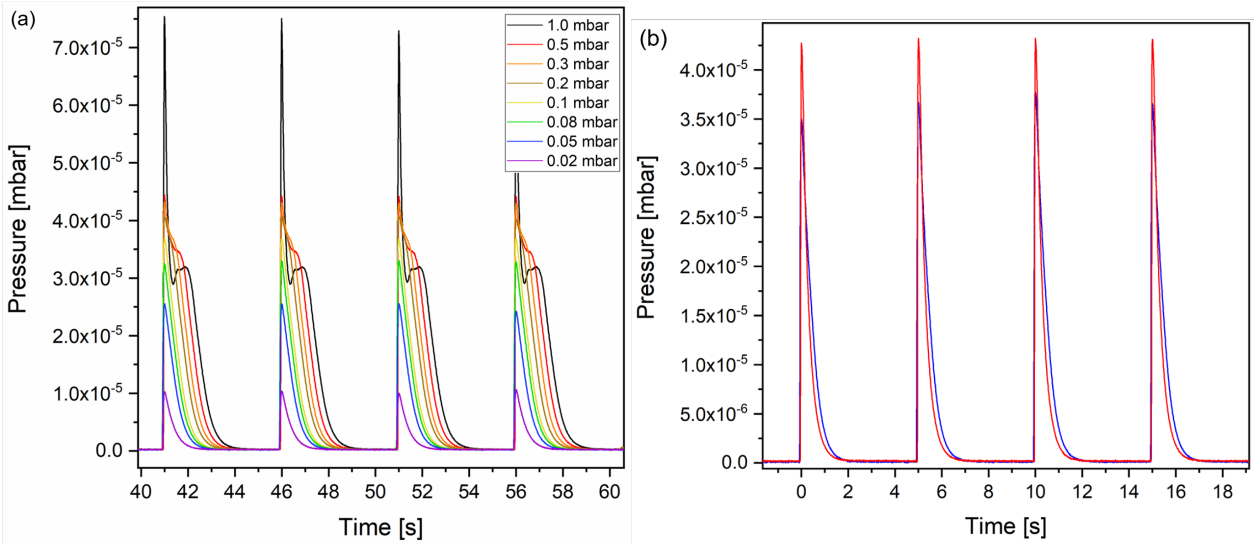

Figure 3.13: (a) Pulse characteristics of the large orifice solenoid valve (2.95 mm) with pre-pressure series. Saturation of the faraday cup is observed for the four highest pre-pressures, showing a saddle-point in the pulse due to an automatic adjustment of preamplifier settings when saturating. (b) An additional welded bellow-sealed valve between solenoid valve and vacuum allows an easy exchange of the valve without the need to break the vacuum and protects the vacuum chamber from leakages at the solenoid valve. The effect of the welded bellow-sealed valve on the pulse shape is shown here for the large orifice valves (2.95 nm, blue line, Faraday cup, 25 V for 6 ms, 5×10^{-2} mbar N_2). A corresponding pulse without the welded bellow-sealed valve is indicated in red.

Using the second set of solenoid valves with an orifice of 0.76 mm, the lighter and now cone-shaped poppet allows for partial or otherwise non-standard opening methods when decreasing the opening voltage below the rated opening voltage of 24 V, as can be observed in figure 3.14a. Changing the opening voltage in 0.1 V steps between 18 and 19 V (using 5 ms and a pre-pressure of 1 mbar O_2) changes the pulse height by more than a factor of ten, while the QMS signal decays back to the baseline within one second for opening voltages below 18.5 V. Similar to the valve with larger orifice above, the pre-pressure influences the height and length of the gas pulses. Figure 3.14b shows the pressure dependence for CO when opening the valve at 17.24 V for 5 ms. The pulse widths (FWHM) is about 200 ms for pre-pressures at 1.0 mbar and below. The pulse height is smaller by a factor of around 100 compared to the larger valve of figure 3.13a. Since the pulses are shorter as well, the corresponding dosage is lower by three orders of magnitude [154].

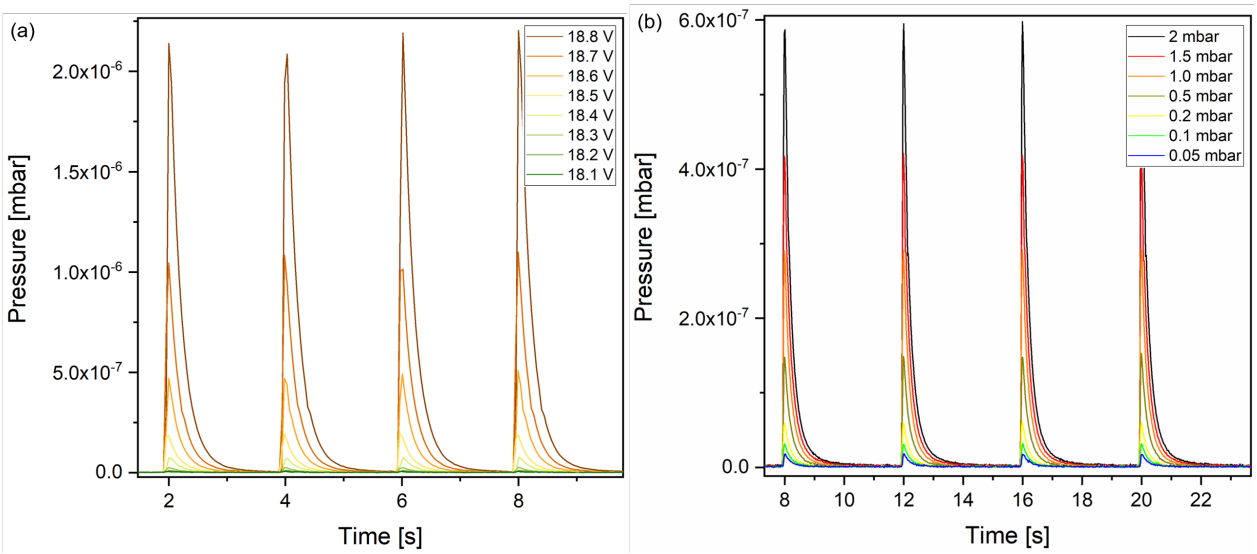

Figure 3.14: Pulse characteristics of a small orifice solenoid valve (0.76 mm). (a) The conically-shaped poppet allows the valve to open partially or in an otherwise non-standard way below its rated opening voltage of 24 V. This enables the adjustment of the pulse size by fine-tuning the opening voltage as shown here. (5 ms electronic pulse length, 1 mbar O_2 pre-pressure) (b) Pre-pressure dependence of the small orifice (0.76 mm) solenoid valve analogous to the large orifice valve data shown in figure 3.13a (17.24 V opening voltage for 5 ms, CO gas).

To find out how much of the reactants does reach the surface, a retraction experiment using the instrument head in the adjustable ball design is performed, starting with the sample in contact with the head of the sniffer and retracting the sample stepwise (see figure 3.15). The dosage is calculated for each pulse and normalised to the pulse at direct sample-sniffer contact. This measurements show that it is particularly important to keep the distance between sniffer and sample as close as possible, while still avoiding to modify the sample by touching it. Furthermore, it is found that about 55 % of the dosage can still be collected with the QMS when the sample is more the 9 mm away. [154] A similar amount of gas can still be measured when moving the sample laterally. This indicates that approximately 55 % of a pulse does not leave the instrument and directly goes to the QMS detector. An attempt to improve this behaviour by removing the ball pod in the fused silica-cone design did yield similar results. Therefore, when calculating yields of surface reactions,

it is important to determine the amount of reactant reaching the surface.

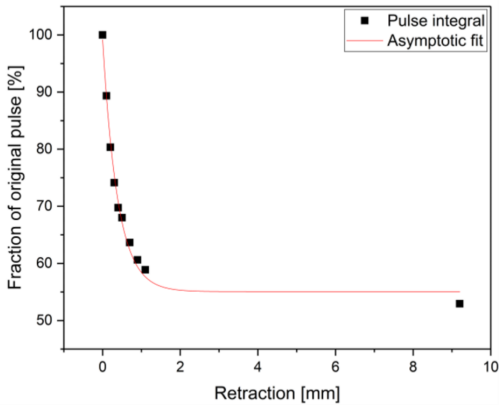

Figure 3.15: Determining how sensitive the Sniffer is to the distance of the sample to the instrument head, CO pulses are applied and the amount of gas detected at the QMS is measured as a function of this distance. The dosage is normalised to the dosage when the sample is in contact with the instrument head. The asymtotic fit serves as a guide to the eye. The signal decays sharply within the first mm from and does not decay below 50 %. Therefore, it is important to take this distance into account for yield calculations. Figure reproduced with permission from [154].

CO Oxidation with Platinum Clusters on $Fe_3O_4(001)$

To demonstrate the capabilities of the instrument for investigating the catalytic properties of nanoclusters on surfaces, the reactivity of platinum atoms on $Fe_3O_4(001)$ (coverage 0.2 particles per nm^2, deposited with the cluster source in unselected mode with a centre of m/z of 100) with carbon monoxide is probed. Bliem et al. [68] found in STM that $Fe_3O_4(001)$ does not change upon CO exposure at 550 K, while decorating $Fe_3O_4(001)$ with platinum atoms leads to the growth of holes upon CO exposure. This is explained by oxidation of CO at platinum particles with lattice oxygen as reaction partner. Platinum atoms are know to be mobile at room temperature already when exposed to 2×10^{-10} mbar CO, forming subnanometer clusters. [69] Here, the CO_2 production on $Pt/Fe_3O_4(001)$ is measured. Due to the mobility of $Pt/Fe_3O_4(001)$, the platinum atoms likely grow to clusters upon initial CO pulsing. Using the Sniffer, the QMS signal of CO_2 (m/z = 44, Faraday cup) while pulsing CO during a temperature ramp (1 K/s) is measured. Applying CO pulses (1 mbar pre-pressure, 17.5 V for 5 ms with 5 s pulse-to-pulse distance) and integrating each pulse separately gives the amount of CO_2 production for the respective temperature displayed in figure 3.16. The solid line represents a trend line for CO_2 production with a running average of 30 data points.

Heating up the sample, CO_2 production starts to increase above 500 K with the maximum at 750 K. A small shoulder at 550 K is observed, where Bliem et al. [68] found the above-mentioned hole growth in STM. This data here shows that CO_2 is produced on $Pt/Fe_3O_4(001)$ above 500 K with CO as reactant and no oxygen source provided besides the lattice oxygen from $Fe_3O_4(001)$, hinting at a Mars-van Krevelen type mechanism [155]. Reactivity of CO starts to increase in the range in which CO desorption is observed on platinum single crystals at low to intermediate coverages (450 - 550 K [156, 157]), creating sites for lattice oxygen to bind to the Pt cluster and subsequently react with CO to CO_2, which can easily desorb at this temperature [158]. The decrease in CO_2

production above 750 K might be related to O_2 desorption similar to the peaks observed on Pt(111) [158, 159] in the range of 700 - 900 K, depriving the reaction of lattice oxygen atoms bound to the platinum clusters and thereby decreasing the probability of simultaneous presence of $CO_{@Pt}$ and $O_{@Pt}$ necessary for CO_2 formation.
These results show that the Sniffer instrument built within this thesis can provide new information for the investigation of surface catalysts. In combination with the existing variable-temperature STM instrument, this opens up opportunities for studies combining precise characterisation of the reactions taking place and the stability of the catalyst based on supported metal clusters.

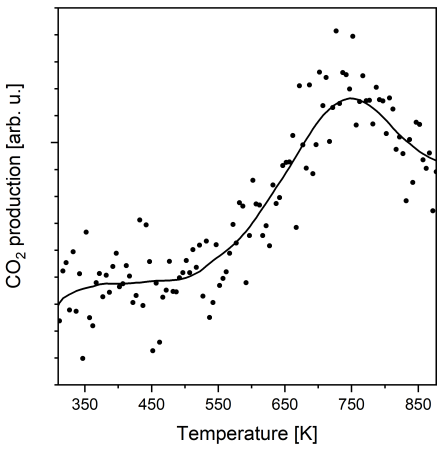

Figure 3.16: CO_2 production (ion current of m/z = 44) over platinum clusters on $Fe_3O_4(001)$ from CO pulsing during a temperature ramp (1 K/s). No oxygen is provided besides the lattice oxygen of $Fe_3O_4(001)$. This confirms that the hole growth of $Pt/Fe_3O_4(001)$ in CO at 550 K observed by Bliem et al. [68] does in fact involve CO_2 production. It is likely that the beginning CO desorption from the Pt clusters at 500 - 550 K facilitates the binding of $O_{lattice}$ to the clusters and thereby increasing the CO_2 production, while the broad O_2 desorption regime from Pt between 700 and 900 K might remove the oxygen from the platinum clusters and might cause the decrease in CO_2 production observed above 750 K (see text for more details).

Conclusions and Outlook

A high-sensitivity instrument for investigating surface catalysts with reactant pulses of transient pressures up to 10^{-4} mbar in ultra-high vacuum has been designed, built, and tested. It allows to titrate small amounts of product of the surface with adjustable gas pulses. Experiments using water as reactant are now easily possible within the UHV chamber without adverse effects to the ultra-high vacuum. Catalytic measurements are possible starting at 100 K to the highest achievable temperature, which is in the range of 1250 - 1350 K for the sample holders used here. The smaller volume of the gas pipes within the instruments and the heated fused silica pipes increase the amount of product which is lead to the QMS, yielding an increase in sensitivity to side products. The instrument built here is shown to have shorter pulse widths (FWHM of 200 ms) than the instrument described by Bonanni et al. (FWHM of 450 - 550 ms)[145] when applying similar pulse maxima.
The combination with variable temperature STM, FastSTM, and a laser-vaporization cluster source

gives a potent tool to combine state-of-the-art local methods with highly sensitive integral tools for investigations into reactivity, catalysis, and catalyst deactivation mechanisms at the atomic scale. Future upgrades of the instrument could include the implementation of photo-desorption and photochemical reactivity measurements.

4 Investigating Surface Defect Dynamics and High-Temperature Stability of the Magnetite (001) Surface

Understanding dynamic processes in catalysis is key to furthering the knowledge of catalytic activity thereof. Catalytic oxidation of organic molecules at oxide surfaces often involves interactions with surface defects [155], and alcohol oxidation is known to crucially depend on the ability to migrate the product hydrogen to a recombination site (e.g. a Pt cluster) in order to allow it to desorb and prevent poisoning of the surface. [16, 160, 161] Metal clusters are prone to sintering processes at elevated temperatures [13, 53] and can deactivate on oxide surfaces by encapsulation by the supporting oxide [162], an effect called strong metal-support interaction (SMSI). Furthermore, as the water-gas shift reaction is performed on a magnetite-based catalyst at higher temperatures and is sensitive to the defect concentration and thereby the amount of Fe^{2+} near the surface [18]. So it is highly desirable to better understand the dynamics on the magnetite (001) surface at elevated temperatures, which could affect the stability and catalytic properties of supported catalysts as well as the magnetite-based water-gas shift reaction catalyst.

FastSTM allows for the local investigation of dynamic processes on surfaces on the atomic scale, to improve the understanding of $Fe_3O_4(001)$ as catalyst and catalyst support. Within the following subchapters, it is found that mobility of defects at the magnetite (001) surface can be controlled separately by temperature adjustment in the range between room temperature up to 780 K. First, H adatoms movement on $Fe_3O_4(001)$ and the influence of a local defect on the dynamics of this movement is investigated. H adatom are know to desorb around 550 K from the $Fe_3O_4(001)$ surface. [83] In the second subchapter, it is found that unreconstructed unit cells (i.e. excess Fe atoms in the subsurface) are mobile in the temperature range starting at approximately 500 K. In a third study, the microscopic processes during the high-temperature phase transition of the magnetite (001) surface involving vertical and lateral Fe atom transport around 720 K is investigated. All three studies take advantage of the functionalities of the new FAST module [113] and they employ the data analysis strategies developed in chapters 3.1 and 3.2 and additional, more specific methods described in the following chapter, where necessary.

4.1 Quantitative Investigation of the Dynamics of Hydrogen on $Fe_3O_4(001)$

In this section the hydrogen mobility on magnetite (001) is investigated. Density functional theory (DFT) calculations shown in this section were performed by M. Meier and C. Franchini at the Technical University of Vienna (see section 6.1 for address) as part of the collaboration on this study. The results of this study were published in *J. Phys. Chem. C* [163], reprinted in section 6.1, where additional details can be found.

Hydrogen Adatoms on the $Fe_3O_4(001)$ Surface

Hydrogen adatoms on $Fe_3O_4(001)$ are bound to oxygen atoms on the non-blocked site of the subsurface cation vacancy structure (see chapter 1.3) and their location can switch between oxygen atoms on opposite Fe rows of the non-blocked site. The bonds to the oxygen atoms lead to an increase in electron density on the corresponding Fe_{oct} atoms in the Fe rows of the surface. [72] Figure 4.1 shows a structural model in perspective view indicating the two preferred positions for hydrogen atoms on $Fe_3O_4(001)$ and the corresponding Fe_{oct} based on DFT calculations.

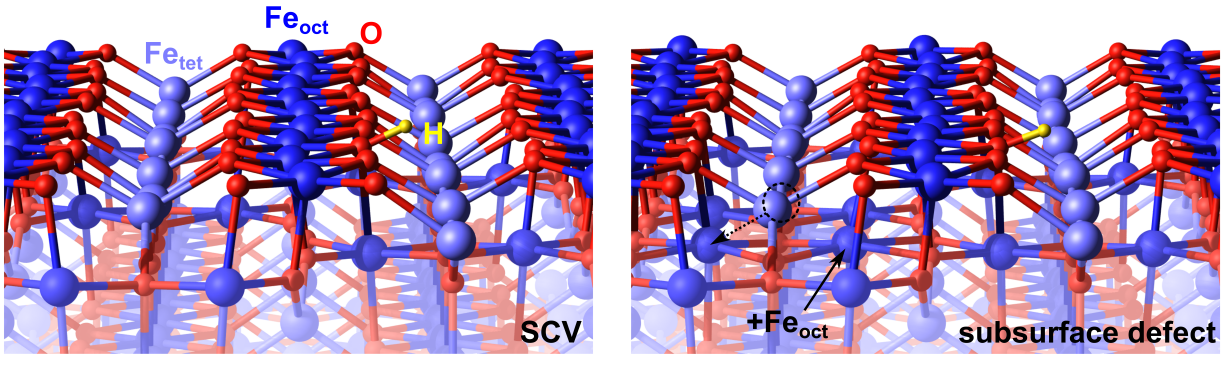

Figure 4.1: Structural model based on DFT calculations of the SCV reconstructed $\left(\sqrt{2} \times \sqrt{2}\right)$ R45° - $Fe_3O_4(001)$ with hydrogen adatom (yellow) on a pristine surface (left) and in an unit cell neighbouring an unreconstructed unit cell in $[1\bar{1}0]$ direction. Reprinted with permission from *J. Phys. Chem. C* **2019**, *123*, 19742-19747. Copyright 2019 American Chemical Society.

In constant current STM measurements, higher electron density in the accessible range of the LDOS appears higher in topography. Accordingly, the Fe_{oct} at OH groups appear higher i.e. brighter in the images presented here. All STM images presented in this section image unoccupied states of the surface ($U_B = 1.5$ V). On the pristine surface, only Fe_{oct} are visible in STM; consequently, the images are dominated by the undulating Fe rows. The white circles and the arrow in figure 4.2 indicate the H atom movement between two sites.

Quantitative Analysis of the H Adatom Switching Rate

Using FastSTM movies to quantify the switching rate of H atoms on the surface requires a computer-based semi-automatic analysis routine to do so. Here, a Jupyter notebook based on Python 3 and OpenCV is used to place oval masks over the bright protrusions and integrate over the signal

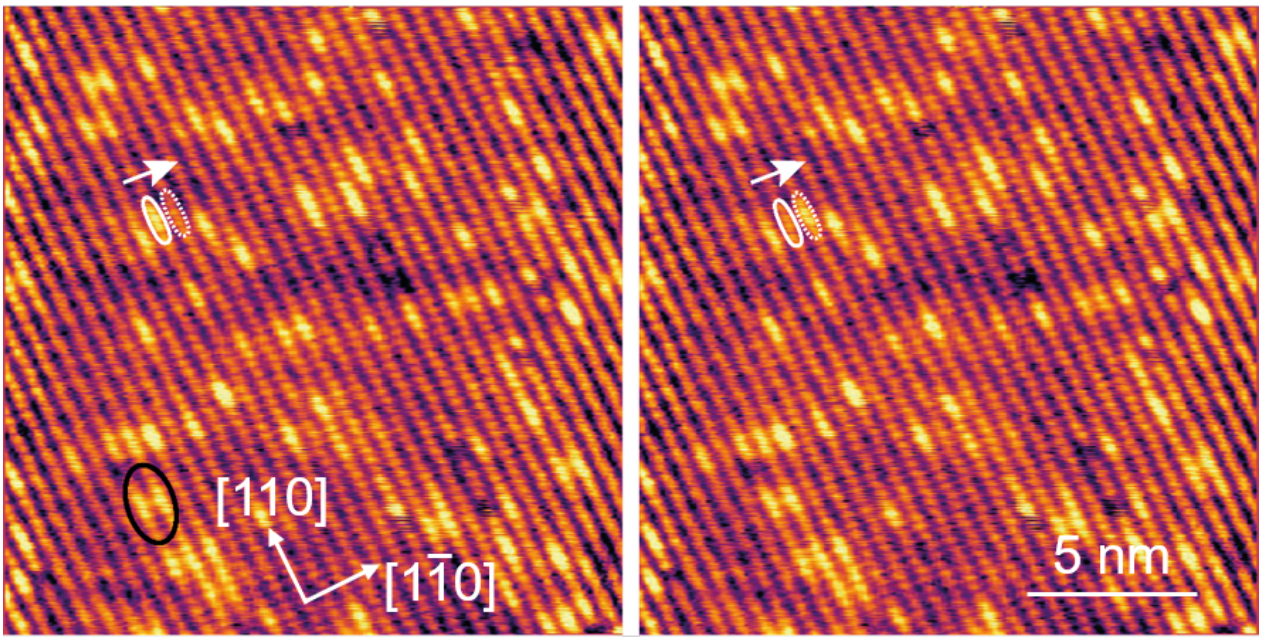

Figure 4.2: FastSTM frames of $Fe_3O_4(001)$ of one movie with a hydroxyl switching event indicated by white ovals and an arrow. An unreconstructed unit cell is marked by a black oval. Reprinted with permission from *J. Phys. Chem. C* **2019**, *123*, 19742-19747. Copyright 2019 American Chemical Society.

intensity i.e. the logarithmic tunnelling current within the oval. Calculating and plotting this integral over time gives a telegraph-noise shaped trace with two states: 0 ("H atom not present") and 1 ("H atom present") as shown in figure 4.3. Now, a line to separate the up and down states can be drawn, assigning each datapoint to a state. This is done by hand in order to check for measurement artefacts and verify that the events are real. In order to obtain a mean residence time of the hydrogen atom at each site, a histogram of residence times is created for each data set, as a simple arithmetic mean is sensitive to outliers and is not a suitable method of quantification for this kind of data, as the data sets obtained here consist typically of at least 50 events. Therefore, the mean residence time shall be obtain by a fit of the histogram based on zeroth-order kinetics, as hydrogen atoms exclusively switch through a single non-blocked site (random process in a two-state system) as long as the surface is not fully hydroxylated and the reconstruction lifted thereby (as discussed in section 1.3). Analogous to the radioactive decay, for a number of H atoms, N_0, the number of H atoms that switch, $N(t)$, in at a certain time, t, to the other site depends on the mean residence time, τ, of the H atom in an exponential way, as shown in equation 4.1

$$N\left(t\right) = N_0 \times exp\left(-\frac{t}{\tau}\right). \tag{4.1}$$

Translating this to a single hydrogen atom in equation 4.2 means that the normalized number of residence times, $N(t)/N_{tot}$, of length, t, decays exponentially with the mean residence time, τ, with the scaling factor, g, for the y-axis intercept being one for a continuous model and N_{tot} as the total

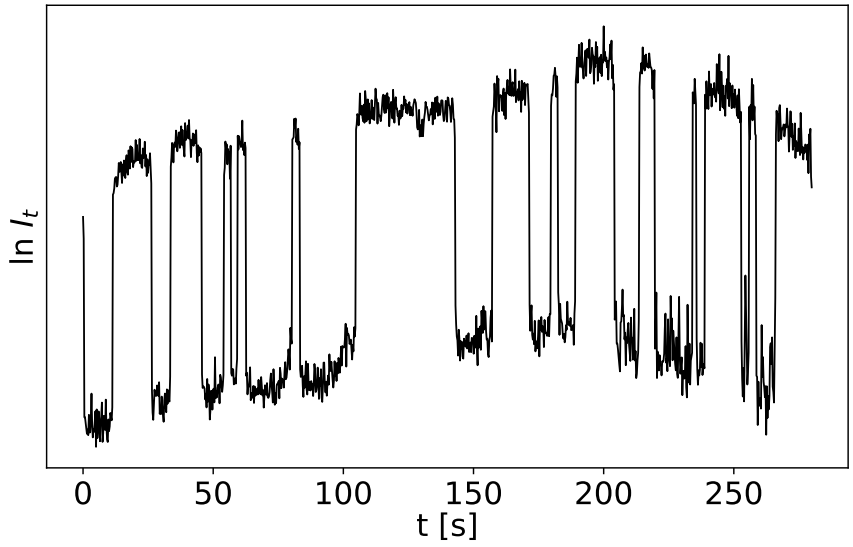

Figure 4.3: Integrated intensities of a single mask of a hydroxyl group showing states for "hydrogen atom present" (higher tunnelling current) and "hydrogen atom absent" (lower tunnelling current) gives a telegraph-noise like signal. The time the hydrogen atom stays at its place uninterruptedly is its residence time. Reprinted with permission from *J. Phys. Chem. C* **2019**, *123*, 19742-19747. Copyright 2019 American Chemical Society.

number of residence times in the data set.

$$\frac{N\,(t)}{N_{tot}} = g \times exp\left(-\frac{t}{\tau}\right) \tag{4.2}$$

Plotting $N(t)/N_{tot}$ in a histogram leads to discretization and causes the y-axis intercept to deviate from one.

The quantity of interest for this analysis is the mean switching rate $r = \frac{1}{\tau}$ which is the inverse of the mean residence time. As visible in figure 4.4, the model fits the data nicely and is therefore used for the subsequent analysis.

Histogram analysis of this kind for limited amount of data has one big challenge - how to select the bins properly. In order to avoid effects of beating due to the limit of time resolution at the frame time (inverse of the frame rate), i.e. 0.25 s for a frame rate of 4 fps, only multiples of the frame time shall be allowed as bin edges. There are several methods in the literature that recommend a good estimate of the bin width, w, for normal-distributed data. They are based on the number of datapoints, n, like Sturges' rule [164]

$$w = \frac{\max - \min}{1 + \log_2(n)}, \tag{4.3}$$

or including the standard deviation, σ, as done by Scott [165]

$$w = 3.5\sigma n^{-1/3}. \tag{4.4}$$

For the application sought here, these two approaches suffer from the fact that the data is not shaped as a normal distribution around a certain value, but decays exponentially and gets close

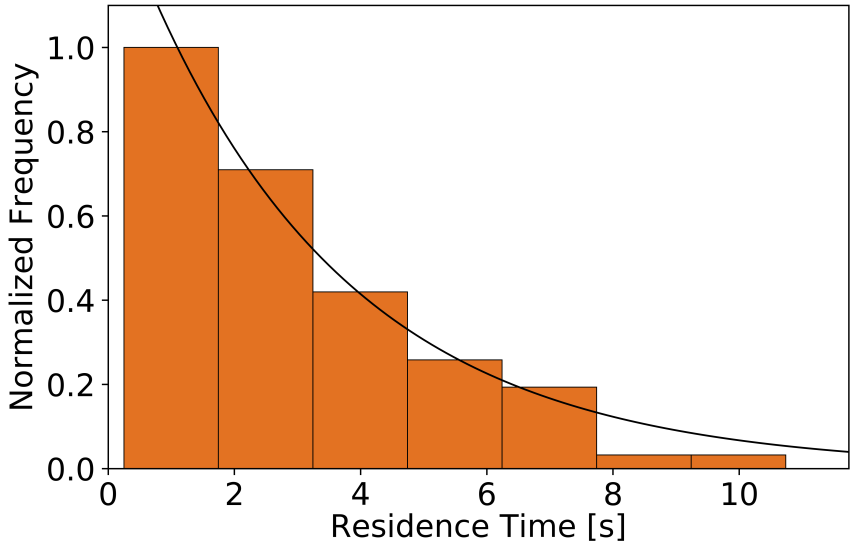

Figure 4.4: Representative histogram for residence times with a fitted single exponential based on the method described in the text giving the mean residence time. Reprinted with permission from *J. Phys. Chem. C* **2019**, *123*, 19742-19747. Copyright 2019 American Chemical Society.

to and even above the time resolution of the measurement. A more sophisticated model has been suggested by Shimazaki and Shinomoto [166] based on work by Rudemo [167]. It counts the number of events, k_i, in each of the i bins. Then, it calculates the mean number of events, k, per bin and the variance of the number of events, ν. Using the bin width, w, the optimized bin width in this model is found for the minimum of the cost function, $C(w)$:

$$C(w) = \frac{2k - \nu}{w^2} \tag{4.5}$$

The method presented by Shimazaki and Shinomoto yielded more deterministic results than the other two methods described above, but it was still sensitive to the bin width when the mean residence time got closer to the limit of the measured time resolution. In order to remove the influence of the bin width on the result, the range of all fitting results with at least three bins as maximal bin size are used and described through the mean between the upper and lower boundaries and the size of the deviation. This is reasonable as the deviation of the set of fit parameters is larger than the mean square error of the single fits.

Energetics of Hydrogen Switching on the Pristine $Fe_3O_4(001)$ surface

The mean switching rates obtained by the histogram-based method described above are now put to use to determine the activation energy of the switching process and the influence of local defects on the process. A summary of the experimental results can be seen in figure 4.5. Arrhenius analysis for H on the pristine SCV $\left(\sqrt{2} \times \sqrt{2}\right)$ R45° reconstruction of $Fe_3O_4(001)$ yields an activation barrier of 0.94 ± 0.07 eV and a prefactor of $1 \times 10^{13\pm1}$ Hz through orthogonal-distance regression of the blue data points in figure 4.5. To exclude an entropic contribution to the Gibbs free energy, the same data set was fitted taking into account transition state theory (see description by Winzor and Jackson in

Ref. [168]). In contrast to the entropic contribution found for porphyrins on Cu(111) [169], only a negligible contribution is observed for the comparatively light H atom. The determined activation energy is the same for both analysis routes. Figure 4.5 indicates as well the effect of undersampling at the orange data points measured at 4 fps as they show a clear deviation from the linear Arrhenius behaviour, while the data points starting at 367 K for the pristine surface were measured at 19.6 fps. The light grey bar illustrates the measurement limit for 19.6 fps measurements of 1/9.8 s, while the dark grey bar indicates the resolution limit for the most common 4 fps settings at 0.5 s. At 367 K, measurements at 4 fps and 19.6 fps found the same hydrogen switching rate, so the result is independent of the sampling frequency. Carpinelli and Swartzentruber [170] performed a systematic atom-tracking study on the diffusion of the Si dimer and found that changes in the bias voltage (and therefore the electric field at the tunnelling junction) affect almost exclusively the prefactor and only very marginally the activation energy. All measurements in this study are therefore performed at a constant bias voltage of 1.5 V and a constant tunnelling current of 1.0 nA. The switching movement is a symmetric one within the error of measurement.

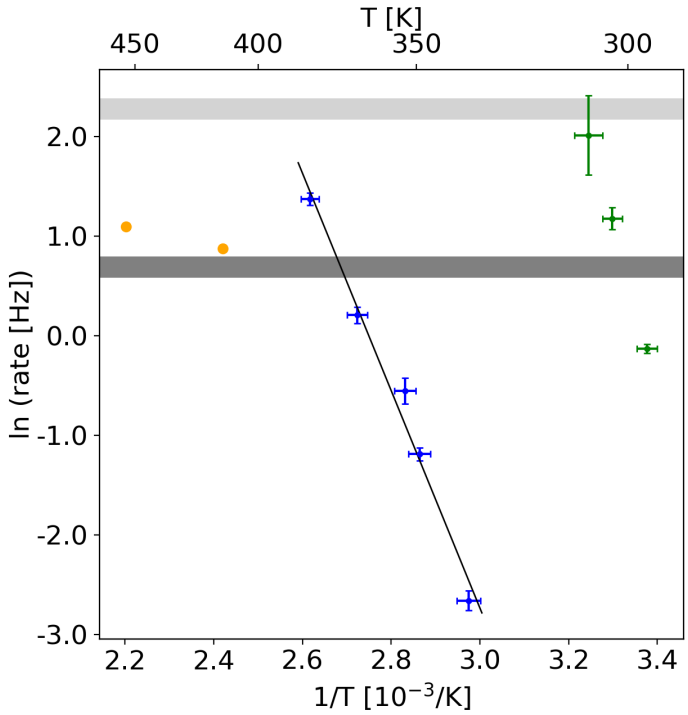

Figure 4.5: Arrhenius plot for hydrogen adatoms on the pristine surface (blue markers) and neighbouring a unit cell with an unreconstructed unit cell in [1$\bar{1}$0] direction (green markers) indicating an activated process. The black line represents an orthogonal-distance regression to the data for the pristine surface. The dark grey bar indicates the resolution limit for 4 fps measurements, while the light grey bar represents the limit for 19.6 fps measurements. All data points marked in green and those at the pristine surface at and above 367 K were measured at 19.6 fps, while the orange markers (measured at 4 fps on the pristine surface) show the effect of undersampling. Reprinted with permission from *J. Phys. Chem. C* **2019**, *123*, 19742-19747. Copyright 2019 American Chemical Society.

Effects of Defect Proximity on Hydrogen Switching

Knowing the results for the hydrogen switching on pristine $Fe_3O_4(001)$, the influence of local defects was investigated. Figure 4.6 indicates the three classes of hydrogen adsorption sites studied here: a H adatom on the pristine surface (blue oval in fig. 4.6, blue markers in fig. 4.5), a H adatom in a unit cell neighbouring an unreconstructed unit cell in $[1\bar{1}0]$ direction (green oval in fig. 4.6, green markers in fig. 4.5), and those neighbouring an unreconstructed unit cell in the other ([110]) direction (white oval in fig. 4.6). The first two cases are shown in the DFT-based structural model in figure 4.1 as well.

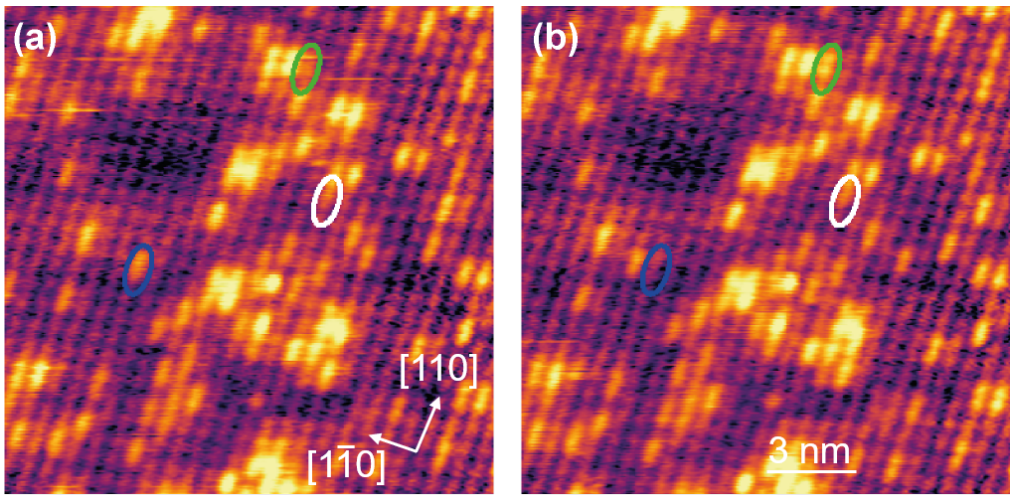

Figure 4.6: FastSTM frames of one movie indicating the three sites studied here. The colours represent those in figure 4.5. Reprinted with permission from *J. Phys. Chem. C* **2019**, *123*, 19742-19747. Copyright 2019 American Chemical Society.

As the FastSTM movies in the supporting information provided online with the published paper demonstrate, the hydrogen adatoms in $[1\bar{1}0]$ direction to an unreconstructed unit cell switch much faster than the ones on the pristine surface. Measuring them close to room temperature gives the switching rates shown as green points in figure 4.5. The corresponding activation energy is estimated by Arrhenius analysis based on the prefactor obtained for H adatoms on pristine $Fe_3O_4(001)$ to be 0.76 eV. This assumption is justified by the DFT results presented below and necessary as the data at 308 K are close to the measurement limit even for measurements at 19.6 fps, leaving only two data points on the Arrhenius in the experimentally accessible range. As for the hydrogen adatom on pristine $Fe_3O_4(001)$ described above, the movement of hydrogen atoms next to the local defect is symmetric within the error of measurement.

The hydrogen atoms neighbouring an unreconstructed unit cell in [110] direction show a much lower switching rate, so a quantification as described above is not possible due to the lack of a sufficient number of switching events for a reliable rate determination. At 349 K, it is estimated to be approximately 0.07 Hz.

No influence on hydrogen atoms at distances above one unit cell from the unreconstructed unit cell was found.

Mechanism

To explain the difference in activation energy and the switching mechanism, theoretical calculations based on DFT were performed.

Figure 4.7 shows the two systems for which DFT calculations were performed, hydrogen on pristine $Fe_3O_4(001)$ and next to an unreconstructed unit cell. Initial state and transition state configurations are shown next to each other. They reveal that the O-O distance of the initial state is shortened when the neighbouring unit cell in $[1\bar{1}0]$ direction is present (3.31 Å) compared to the pristine surface (3.50 Å). The O-H bond distance in the initial state is similar for both cases (0.99 Å), as the surrounding lattice distorts to enable this geometry. In the transition state, however, the O-O distance (2.6 Å) and the O-H distances (1.3 Å) are similar with and without a neighbouring unreconstructed unit cell. Furthermore, the Fe-O bonds of the accepting O atom do not need to extend as much (0.22 Å) to reach the transition state as for the pristine surface (0.28 Å). Activation barriers are computed to be 1.27 eV for the pristine surface and 1.00 eV for the hydrogen adatom with an unreconstructed unit cell in the neighbouring unit cell in $[1\bar{1}0]$ direction, while the diffusion path remains the same. Due to a limited temperature range available for the second case, the shift in temperature between the two data sets in figure 4.5 and 4.7 is compared to the energy difference of 0.27 eV, which is approximately 100 K. Thereby, experiment and theory are in good agreement. Furthermore, it is in agreement with the difference in activation energy calculated from the experimental data under the assumption that the prefactor does not change as discussed there. DFT confirms the experimental observation that the process is symmetric, as initial and final state energy differences are below 0.1 eV and therefore in the range of common DFT fluctuations. In all, the cumulative energy cost of multiple distortions reduces the activation energy necessary for the switching process with neighbouring unreconstructed unit cell in $[1\bar{1}0]$ direction.

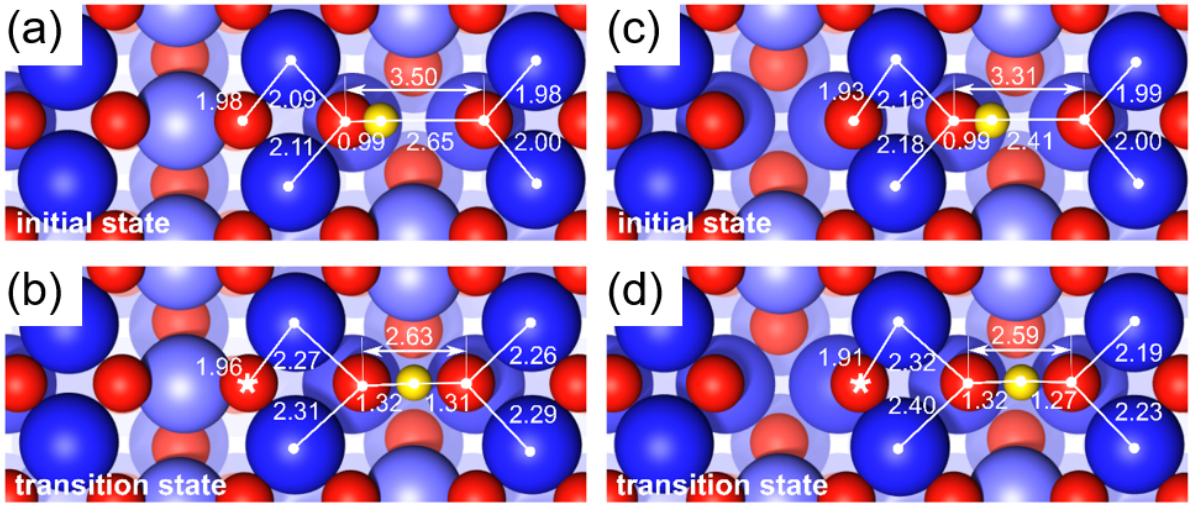

Figure 4.7: Structural models based on DFT-calculations for the initial (a,c) and the transition state (b,d) for a hydrogen adatom on the pristine SCV (a,b) and for a hydrogen adatom at a unit cell neighbouring an unreconstructed unit cell in $[1\bar{1}0]$ direction (c,d). Colours represent those from figure 4.1. Reprinted with permission from *J. Phys. Chem. C* **2019**, *123*, 19742-19747. Copyright 2019 American Chemical Society.

Conclusions and Outlook

This study shows the dependence of the switching rate on the local environment, in particular a local, Fe-rich defect, to which lattice distortions by the defect contribute. As no long-range diffusion of adsorbed hydrogen atoms up to 450 K is observed, reactions with a hydrogen migration step (similar to photocatalytic alcohol reforming on $TiO_2(110)$ [160, 161]) need a different hydrogen transport mechanism. This could include either a fully hydroxylated surface, which might allow long-range hydrogen atom transport, or higher temperatures near the water desorption temperature of 550 K [83]. Karim et al. [15] showed that the hydrogen diffusion is different on a TiO_2 and a Al_2O_3 surface. Using platinum clusters for hydrogen dissociation on this surface, the theory of long-range surface diffusion of hydrogen could be tested and investigated if there is a limit of how far this transport could happen around a cluster and if there is a size-dependence for efficient hydrogen dissociation and transport over $Pt_x/Fe_3O_4(001)$. Transitioning to alcohol reforming might reveal information on the hydrogen transport on the surface and - using the Sniffer implemented as part of this thesis as described in chapter 3.3 - investigating the reactivity of the surface. As it is known that additional Fe evaporated onto the surface increases the reactivity towards methanol [78], exchanging this with other transition metal could allow to tune the reactivity.

4.2 Lateral Mobility of Cations at the Fe_3O_4(001) Surface

In this section the lateral mobility of the cations in the surface region of the Fe_3O_4(001) surface is investigated.

Reducible oxides like magnetite are known support materials for CO oxidation with metal atoms [68] or nanoparticles [155] as catalyst. These reactions typically involve the extraction of a lattice oxygen atom as part of a Mars-van-Krevelen mechanism [155], where lattice oxygen atoms from transition metal oxide surfaces react with the reactant. Upon oxygen removal, Fe goes to the bulk, which acts as a sink for Fe atoms, leaving the surface with holes visible to STM [68]. This Fe transport can be used in the opposite way when oxygen atoms are provided on the surface, leading to island and subsequently film growth with Fe atoms from the bulk providing the Fe atoms. On the bare surface, this is observed during sample preparation of a new SCV surface layer upon oxygen dosage at temperatures above 720 K. [20, 171] The temperature for island growth can be reduced by placing platinum atoms or nanoclusters on the surface, which can dissociate molecular oxygen already at 550 K [68]. The diffusion of Fe atoms in polycrystalline bulk magnetite [172–176] and on the Fe_3O_4(110) surface region [177–179] has been studied since the 1980s at high temperatures (1023 - 1773 K) measuring penetration depths of radioactive tracers caused by annealing , finding a transition from a vacancy to an interstitial-type diffusion mechanism when decreasing the oxygen partial pressure below 10^{-3} mbar at 1473 K [172, 173, 179]. Measurements of the polycrystalline material as low as 773 K suffered from a strong influence of the grain boundaries on the data. [180] Shifting to temperatures below the high-temperature surface phase transition around 720 K, studied in more detail in chapter 4.3, integral measurements on the (001) surface using x-ray and neutron reflectometry have started. [181, 182] Low-energy electron microscopy (LEEM) data from [171] showed that the lateral movement of step edges on the Fe_3O_4(001) surface during the growth of the surface region in an oxygen atmosphere at temperatures between 830 and 953 K has an activation energy of 1.51 eV. transmission electron microscopy (TEM) images of epitaxially-grown films of Fe_3O_4 contain domain boundaries, which are found to grow in size upon annealing at temperatures between 520 and 620 K with an activation energy of 0.25 eV. [183] Theoretical calculations for bulk diffusion in Fe_3O_4 from [184] predict a movement from an octahedral site to an octahedral vacancy via a metastable tetrahedral intermediate with an activation barrier of 0.70 eV.

The Fe_3O_4(001) Surface in STM

Looking at STM images like figure 4.8, anti-phase domain boundaries (APDBs) appear as a chain of bright lobes, which runs in 45° to the dominant Fe rows of the first layer of the structure. They appear because the unit cell of the SCV structure can have two registries (since the additional Fe atom in the second layer can be in either of the two possible sites). [79] When domains with different registries meet during sample preparation, a domain boundary forms. The unit cells where the domains touch each other can now have either more or less Fe atoms. The common model is the Fe-rich APDB, originating from four adjacent Fe_{oct} in the third layer (for comparison, there are two neighbouring third layer Fe_{oct} on the pristine surface) and no interstitial Fe atoms in the second layer (i.e. only the two bulk-like Fe_{tet} are present). [78] Additionally, it can be observed that the bright APDB chain stops on a terrace as visible in the top-left corner of figure 1.7a and

in figure 9a of [185]. But this does not do away with the different registers of the two domains, so there must be a different structure present when two domains meet and do not show a chain of single bright lobes as a results. Therefore, a more detailed look at the contrast of STM images is necessary, which additionally shed some light onto the other bright lobes present in figure 4.8. The first layer of the surface is relatively stable and structural defects are usually explained by

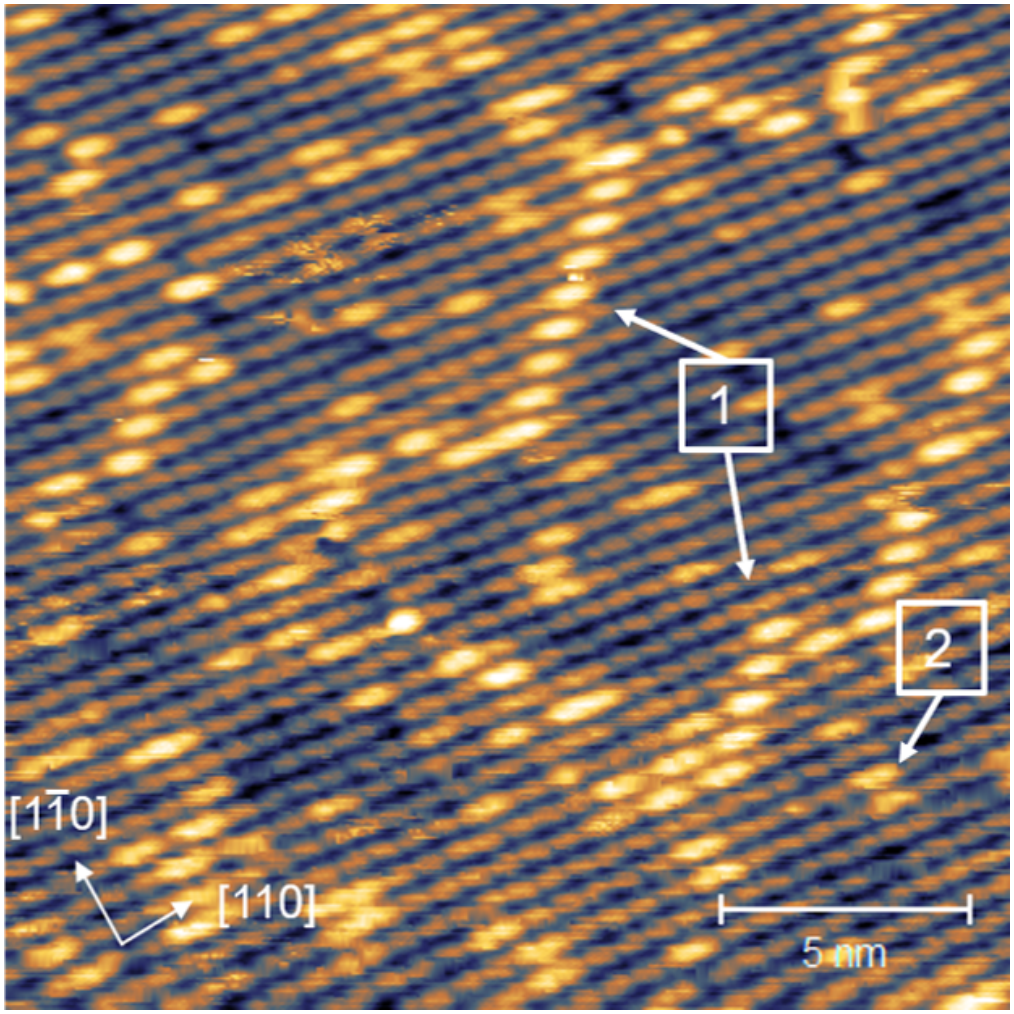

Figure 4.8: STM image of the surface at room temperature with a Fe-rich APDB (1) and one double-lobed feature commonly associated with an unreconstructed unit cell marked as (2). (U_B = 1.5 V, I_t = 0.3 nA)

rearrangements of cations in the second and third layer of the surface reconstruction. [72, 78] Of those two layers, the Fe_{oct} in the third layer play an outsize role in changing the LDOS and increasing the electron density. Generally, the bright single lobes in STM of Fe-rich APDBs are explained by four adjacent Fe atoms in the third layer [78], while, in principle, three neighbouring cations in the third layer would be sufficient for a bright oval to appear in STM. [67, 76, 77] The general idea behind the SCV model is that the third layer contains a pair of Fe_{oct} less (the subsurface cation vacancy) while the second layer has one Fe_{tet} more above the created vacancy. Adjacent lobes on two neighbouring rows (double-lobed features) result from six adjacent cations in the third layer and a vacancy in the second layer in the middle between the two lobes and are commonly assigned to unreconstructed unit cells. [78] To exclude double-counting of lobes in subsequent lines in STM,

a particular configuration shall be imaged in more than one frame.
Using this discussion of the STM contrast as basis assumptions, it is now possible to use them to interprete the dynamic motion of surface defects on the $Fe_3O_4(001)$ surface: first Fe-rich and Fe-poor APDBs and, afterwards, local Fe-rich defects.

Dynamics of Anti-Phase Domain Boundaries on $Fe_3O_4(001)$

Using conventional STM and FastSTM, the dynamics of APDBs of $Fe_3O_4(001)$ have been investigated at temperatures of 353 K and 413 K.
At 353 K, APDB movement is relatively slow and can be monitored with conventional STM. Two subsequent images are shown in figure 4.9. They indicate that APDBs at this temperature are mobile exclusively at their kink sites (emphasised by white arrows) and not site along their straight chain of bright lobes. Based on the discussions of the STM contrast above, this kink site motion can be explained by the lateral movement of two Fe atoms in the third layer, consequently creating four adjacent Fe atoms in the third layer in both configurations of the kink. To complete the movement of the APDB, a Fe atom in a tetrahedral position of the second layer moves in the opposite directions to the third layer atoms. This yields structural models for both sites that are in agreement with the static interpretation of the SCV model for RT images in [78]. Increasing the temperature to

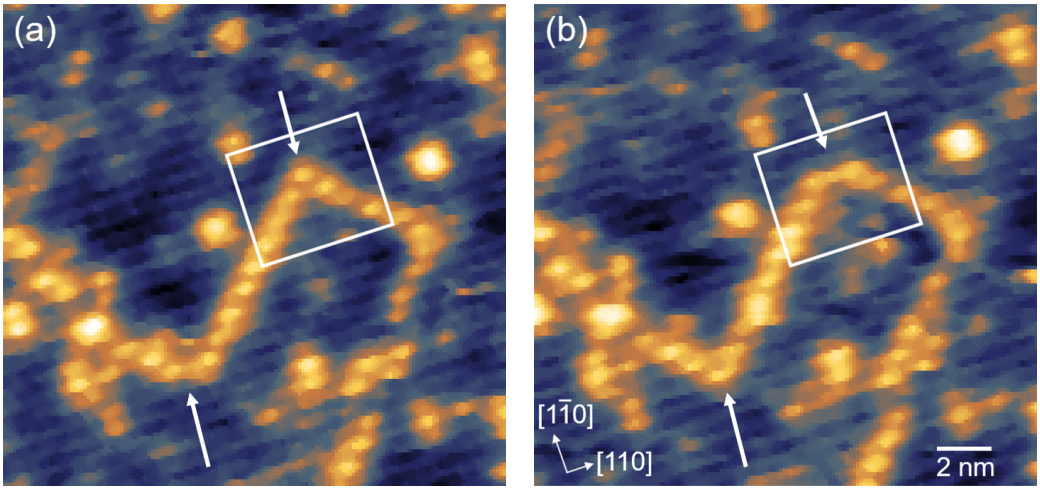

Figure 4.9: Two subsequent STM images of an anti-phase domain boundaries at 353 K, where mobility at the kink sites is observed (white arrows) (U_B = 1.5 V, I_t = 0.3 nA). The regions marked with white rectangles are represented in the models in figure 4.10.

413 K, FastSTM allows the observation of the accelerated movement at the APDB kinks. More mobility tends to be observed in APDB sections with more kinks. At 413 K, the chain of bright lobes of the APDBs can be be temporarily interrupted at kinks, which was not observed at 353 K or lower temperatures (see figure 4.11a-d). Four FastSTM frames at 413 K are shown in figure 4.11a-d. In analogy to the lower temperature movement, a tentative model for the movement observed at 413 K is suggested in figure 4.11e-h for the third layer atoms based on the tentative assumption that each lobe originates from four third layer atoms (this is commonly assumed for APDBs based on the interpretation of APDBs in [78]; in principle, already three adjacent third layer atoms can result in a single isolated lobe as shown for the incorporation of transition metals into the surface

by [67, 76, 77]). Because additional cations in the third layer would create additional bright lobes in STM, it is assumed that the unit cells at the horizontally aligned bright lobes in figure 4.11e-h can contain up to four cations in the third layer when necessary to explain the STM image. As a consequence, the third layer sites in the adjacent unit cells along the $[1\bar{1}0]$ axis likely contain zero cations. A similar local structure with adjacent unit cells of four and zero third layer cations close to regions where different domains meet could explain the structure at Fe-poor APDBs (i.e. contact regions between domains where no bright lobes are visible or the chain of bright lobes ends on a terrace, visible in the top-left corner of figure 1.7a of chapter 1.3 and in figure 9a of [185]). Building on the considerations for the third layer, a tentative model for the first and second layer is shown in figure 4.11i-l. It seems likely that the second layer structure along the straight segment of the Fe-rich APDB behaves similar to the lower temperature APDB movement (i.e. movement of one Fe_{tet} in opposite direction to the third layer atoms). No bright lobes were added or vanished during the movement shown here. It is not entirely clear, if the position of the ripped-off bright lobes in figure 4.11d is slightly shifted towards the neighbouring chain of lobes due to electronic effects or lattice distortion.

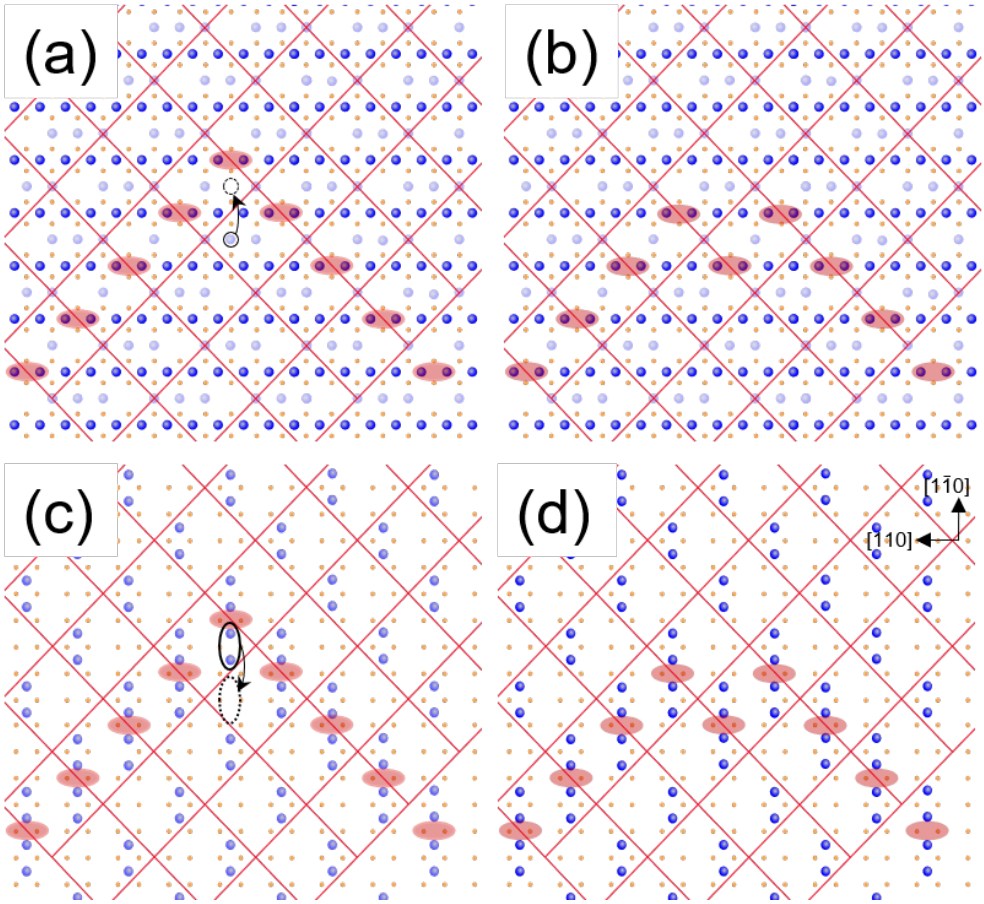

Figure 4.10: Schematic representation of the initial (a,c) and final (b,d) state of the STM images of figure 4.9 at the first and second (a,b) and the third surface layers (c,d). Oxygen atoms are shown in orange, the $\left(\sqrt{2} \times \sqrt{2}\right)$ R45° unit cell is displayed by a red grid, and the bright protrusions in STM are indicated as filled red ovals. Fe_{oct} are represented in dark blue, while second layer Fe_{tet} atoms are light blue in this model. Arrows indicate the suggested movement of atoms corresponding to the STM images of figure 4.9. More details for the model are provided in the text.

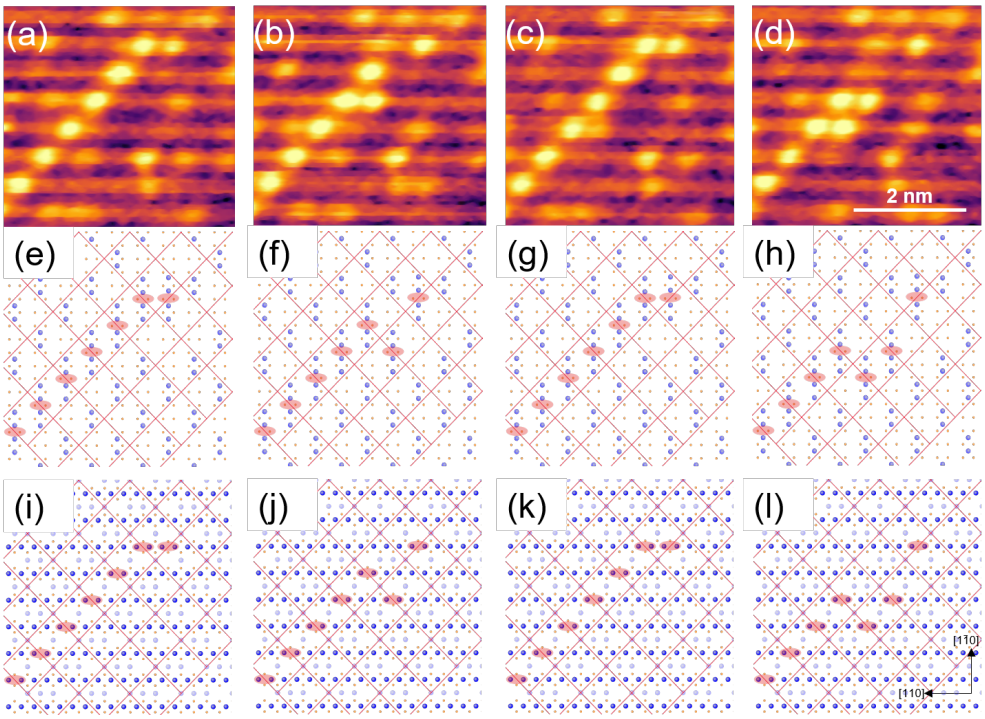

Figure 4.11: (a-d) FastSTM frames of an APDB at 413 K, observing mobility at kinks as well as a temporary interruption of the bright-lobed APDB chain. A tentative model for the structures observed is shown for the third surface layer (e-h) and the first two layers (i-l). Detailed discussion of the model can be found in the text (U_B=1.5 V, I_t=1.0 nA, 4 fps).

Dynamic Movements of Surface Defects on $Fe_3O_4(001)$

Heating the sample to higher temperatures than the ones above, a characteristic movement is observed for two more Fe-rich defect structures: a double-lobed feature and a defect containing a bright protrusion next to a dark depression in a neighbouring Fe row, henceforth labelled bright-dark defects in this thesis. The latter appear similar to the bright dark features observed by Parkinson [20] and can appear after increased Ar sputtering of the single crystal surface before surface preparation. To the author's knowledge, no complete explanation for these defects has been developed up to now going beyond the observations of [20] that their number is reduced by stronger oxidation of the single crystal. It has to be noted that the occurrence of bright-dark defects is dependent on the history of the crystal, as the first three layers are involved in the surface reconstruction.

At this temperature, only FastSTM can resolve the movement with sufficient time resolution, looking at the double-lobed feature, whose movement is investigated by FastSTM at 516 K. The "zig-zag"-like motion alternates diagonally between two double rows of the first layer Fe atoms. Positions for double-lobed features in the movie are represented by filled circles in figure 4.12a on one frame of the movie. Each colour represents the position of the double-lobed feature (i.e. the point between the two lobes) over time. The circles together with the periodicity of the Fe rows are used to impose a regular grid onto the image (shown in white), confirming the regular nature of the movement. The number of double-lobed features does not change, indicating that the movement has to be a lateral one.

A similar pattern is observed when investigating the bright-dark features at 533 K. At this temperature, the bright-dark features are mobile and move diagonally to the rows in a "zig-zag"-like pattern shown in figure 4.12b. Figure 4.12b indicates the movement by two Fe rows back and forth along the $[1\bar{1}0]$ axis. It appears that the dark depression travels along the Fe row while, simultaneously, the bright lobe moves to the Fe row on the other side of the dark depression. This movement can be observed for minutes in FastSTM. A sketch of the movement is included in the top-right corner of figure 4.12b. Comparing the movement of double-lobed features and bright-dark defects , the "zig-zag"-like movement of the bright lobes between Fe rows seems to be similar. One bright lobe is usually considered to result from three (sometimes four in the case of APDBs) adjacent cations in the third surface layer, two bright lobes in STM therefore likely originate from six adjacent cations in the third layer [67, 77, 78]. Therefore, the tentative model for the motion of double-lobed features , bright-dark defects , and APDBs shown in figure 4.13 focusses on second and third layer motion. Cations in the third layer necessary to create the features observed in STM are marked with black circles for the initial state. Based on the observed patterns and the assumption that double-lobed features likely result from six adjacent cations in the third layer, the final position of the jump event is likely the unblocked site marked with dashed black circles in figures 4.13ad. To arrive at the final structure, multiple cations need to move, which might be a reason why this dynamic is not observed at lower temperatures. The snapshots of the motion suggest that the positions of the double-lobed feature moves as glide reflection along the glide plane indicated as dashed line in the figure. Commonly, double-lobed features on the $\left(\sqrt{2} \times \sqrt{2}\right)$ R45° - $Fe_3O_4(001)$ surface are associated with unreconstructed unit cells. Nevertheless, based on the data presented it is not possible to rule out the possibility that the double-lobed features at least partly originate from scarce

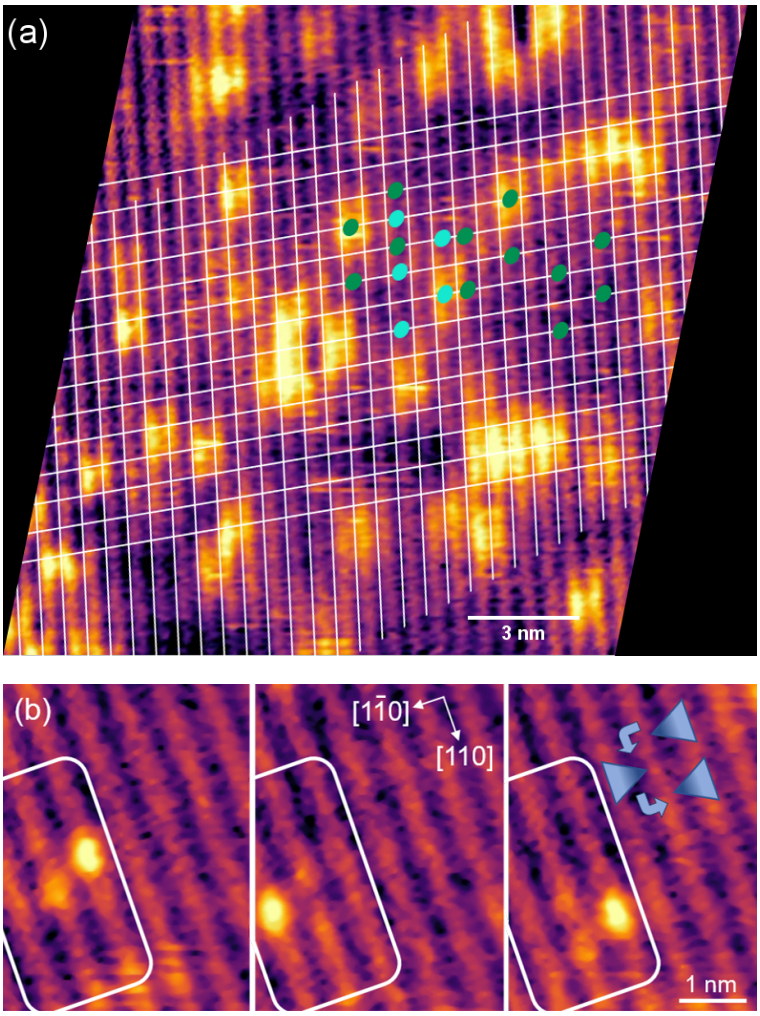

Figure 4.12: (a) FastSTM frame indicating the locations of double-lobed features during a FastSTM movie at 516 K showing a characteristic "zig-zag" motion. A regular grid is placed over the jump sites. The two colours indicate that movement can occur on two registers shifted laterally by one row. (b) On a single crystal reduced by increased sputtering before surface preparation, a similar characteristic motion of bright-dark features is observed with FastSTM at 533 K. The surface region of the moving bright-dark feature is highlighted in white as a guide to the reader's eye and an illustration of the change in contrast is shown in the top-right corner (U_B = 1.5 V, I_t = 1.0 nA, 4 fps).

impurities of the single crystal [20], which move up and down between two Fe rows and cause other Fe atoms to move to create the LDOS measured here in STM. It is imaginable that the mechanism is a concerted one, triggered by an adsorbate that diffuses along the glide plane and induces lateral displacement of Fe atoms in the third layer.

Applying a similar analysis for the bright-dark feature in figure 4.13be based on the assumptions described above, the movement of the bright lobe can be described as glide reflection at the glide plane indicated in the model structure. The relative shifts in position indicated by the red arrows for the bright lobe (b,e) and the double-lobed feature (a,d) are the same. Using this analysis for the standard APDB movement observed at 353 K and discussed above, it is found in figure 4.13cf that position of the bright lobe moves along the [1$\bar{1}$0] axis by the same length as the other two features, but does not move along the [110] axis in the same manner. In order to get further insights

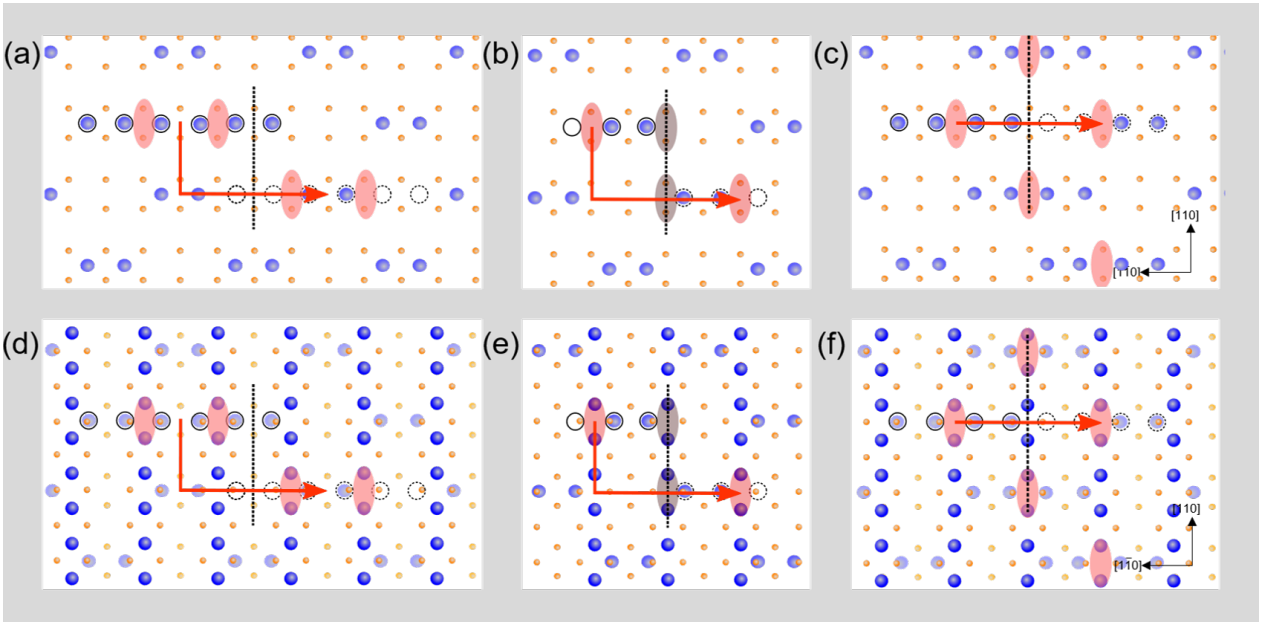

Figure 4.13: Models for the movement of (a) double-lobed features, (b) bright-dark defects, and (c) APDBs in the third surface layer. To facilitate comparison to measured FastSTM movie frames, the first surface layer structure is added to the models in the second row (d, e, f). Fe atoms are shown in blue, oxygen atoms in orange, bright lobes in STM are shown as filled red ovals, the dark lobe of the bright-dark feature is indicated by a filled grey oval, the glide planes are shown as dashed black lines, and the movement is indicated by red arrows. A more detailed discussion of the models is presented in the text.

into the double-lobed features , large scale atomic resolution STM images of the $\left(\sqrt{2} \times \sqrt{2}\right)$ R45° - $Fe_3O_4(001)$ surface at room temperature were taken. In figure 4.14, sites commonly labelled "blocked sites" are marked with a red point on the main terrace, this yields a grid that can distinguish the position of double-lobed features within their unit cells over a larger terrace. As the grid is drawn regularly over the image, the red points in the minor domains on the outer side of a APDB chain mark the "non-blocked site". Double-lobed features are marked with filled circles in blue for double-lobed features at blocked sites and in green for double-lobed features at non-blocked sites. Two more images measured at different days are analysed in a similar fashion, included in the analysis presented her and provided in the appendix of this thesis. Hydrogen adatom movement between non-blocked sites in FastSTM is used to tell the difference between the blocked and non-blocked sites at the bias voltage applied here, since the undulations in the Fe rows are imaged differently in STM dependent on the bias voltage [72].

Most double-lobed features are centred at blocked sites (89 %, 68 out of 76) and only 11 % (8 out of 76) of the double-lobed features are centred at an non-blocked site. Assuming the double-lobed features are unreconstructed unit cells - as commonly done in the literature at room temperature [20] -, the majority species is slightly more favourable energetically and forms therefore preferentially during surface preparation and rather slow cooling down. However, the mean residence times of the two double-lobed feature positions do not deviate significantly, but the very slow nature of the dynamics at the measured temperatures allows only the distinction of rather sizeable differences of residence times, while the data presented here does not allow to distinguish smaller differences in residence time.

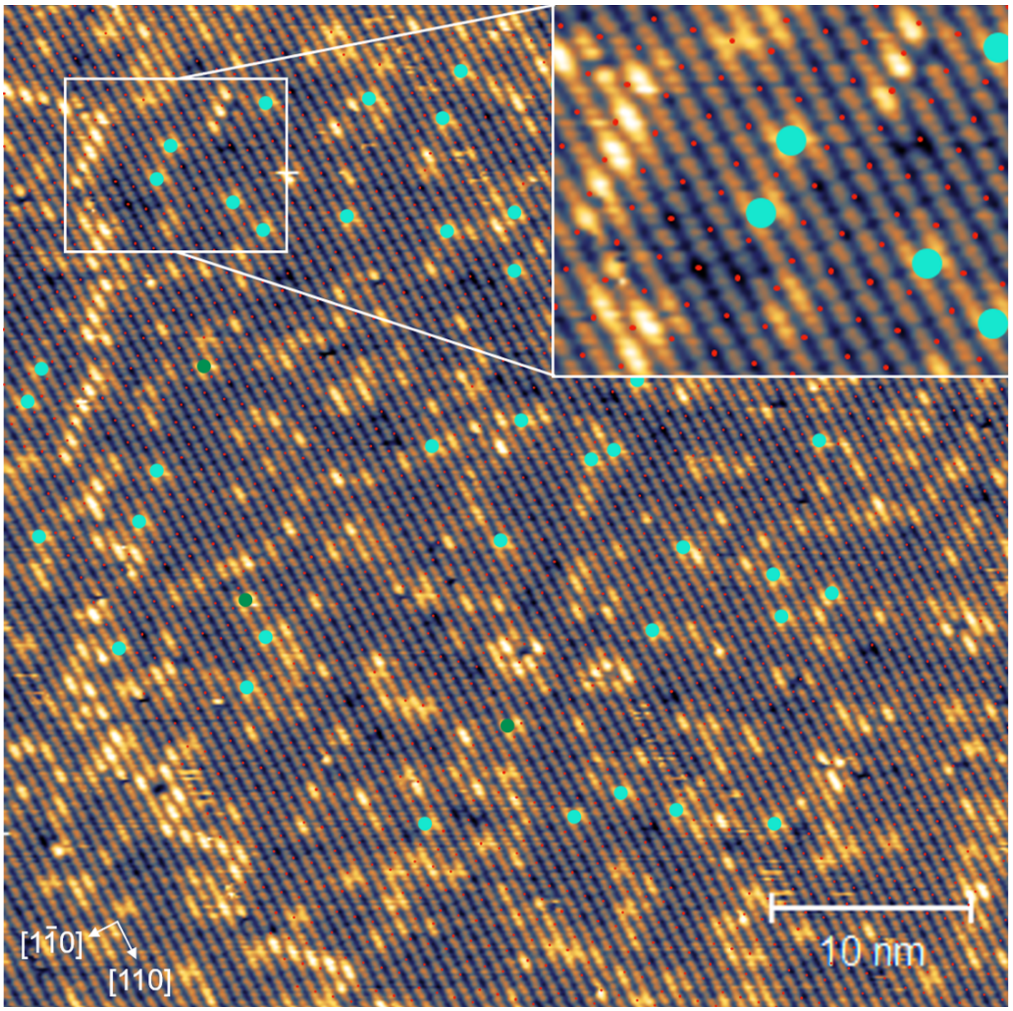

Figure 4.14: Atomically resolved STM image of $Fe_3O_4(001)$ surface at room temperature used to determine the locations of double-lobed features (assigned to unreconstructed unit cells, UUCs). A unique spot in the unit cell is marked by red points at the blocked site of the unit cell based on the central domain, UUCs at their original blocked sites are marked in blue, those at unblocked sites are marked in green. APDBs shift the unit cell by half a unit cell, leading the red points to mark the unblocked sites in the left side domain instead of the blocked sites in the large domain. As described in the text, UUCs at the original blocked sites are found more often by approximately a 9:1 ratio compared to those at unblocked sites. A magnified version of the region marked with a white rectangle is shown in the inset (U_B = 1.5 V, I_t = 0.3 nA).

Conclusions and Outlook

First, the dynamics of anti-phase domain boundaries at the $Fe_3O_4(001)$ surface is investigated at two temperatures above room temperature. An ordered site-exchange exclusively at kink sites is found at temperatures at 353 K, while additionally a temporary chain rip-off at kink sites is observed at 413 K. Mobility is only observed at kink sites. The ”regular” kink motion is explained by movement of Fe cations in the second and third surface layer. A tentative model for the chain rip-off processes and Fe-poor APDBs is given. Secondly, it is shown that double-lobed features and bright-dark features show a characteristic ”zig-zag” motion when heating the $Fe_3O_4(001)$ single crystal to 516 K and 533 K, respectively. Their movements can be described by glide axis. The location of the glide axis shifts from being along the second layer Fe_{tet} atoms for the double-lobed

features and along the Fe_{oct} of the first layer for bright-dark defect s and APDBs. Comparable jumps along the Fe rows are found for double-lobed features and bright-dark features , the regular APDB periodicity along the $[1\bar{1}0]$ axis is similar to the behaviour of double-lobed features and bright-dark features . A speculative model for the double-lobed feature and the bright-dark feature dynamics is presented based on third layer considerations. The temperature necessary to observe this process and the amount of atoms that need to move for this process to happen hint at a rather high activation energy of the process. Due to the structure of the species, activated diffusion at or diffusion near the strong friction limit [186] seems likely. Thirdly, a static analysis of the positions of double-lobed features at room temperature is performed, showing approximately 10% of the double-lobed features at atypical non-blocked sites in the $\left(\sqrt{2} \times \sqrt{2}\right)$ R45° unit cell, which could in principle result from freezing the "zig-zag"-motion upon cooling and might be explained by a small difference in energy which accumulates due to the slow cooling rate during sample preparation (<1 K/s). An effort to explain the dynamics of double-lobed features in the light of their description as unreconstructed unit cells in the literature [20, 78] is undertaken.

4.3 Stability of the SCV Surface at the High-Temperature Phase Transition

In this section the stability of the $\left(\sqrt{2} \times \sqrt{2}\right)$ R45° reconstruction of the magnetite (001) surface at high-temperature is investigated. The results of this study were submitted as a joint publication with the results from SXRD, LEIS, and photoelectron spectroscopy described below. A draft manuscript is included in section 6.2, where additional details can be found.

Previous Work 1: LEED/LEEM

In 2013, Bartelt et al. [187] found by integral measurements (LEED, see figure 4.15) that the Fe_3O_4(001) surface undergoes a second order phase transition around 720 K. The LEED and LEEM data showed the behaviour of an order-disorder phase transition. Using a two-dimensional Ising model, the authors speculated based on the description of APDBs in the distorted bulk-truncation model [79] that a gradual reduction of the subsurface Fe atoms in octahedral positions might play a role, but did not have more experimental data, particularly microscopic information, to exactly determine what happened at the surface on the atomic scale.

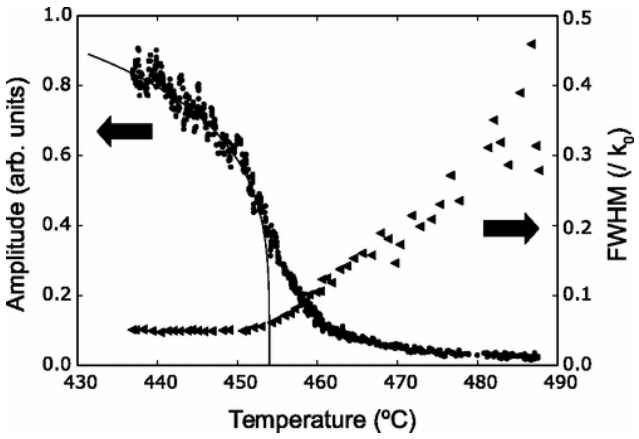

Figure 4.15: Magnetite(001) high-temperature phase transition in LEED measurements by Bartelt et al. [187] with the fit (continuous line) to a 2D Ising model estimates the transition temperature to 727 K (454°C). Amplitude (circles) and FWHMs (triangles) of LEED spots fitted with Lorentzian functions as a function of temperature. Reprinted figure with permission from Bartelt, N. C. et al., J. Phys. Rev. B, 88, 235436, 2013. Copyright 2013 by the American Physical Society.

Previous Work 2: SXRD

Surface x-ray diffraction (SXRD) measurement and fits shown in this section were performed by Björn Arndt, Elin Granäs, Marcus Creutzburg, Konstantin Krausert, Vedran Vonk, and Andreas Stierle at the Deutsches Elektronen-Synchrotron (DESY) in Hamburg.

The researchers used SXRD to confirm the initial LEED measurements from Bartelt et al. [187] and to further investigate site occupancies at temperatures below, during, and above the phase transition [188]. Figure 4.16 shows SXRD measurements of the crystal truncation rods for the

$\left(\sqrt{2} \times \sqrt{2}\right)$ R45° reconstruction of magnetite (001) for different temperatures (heating up and cooling down). The signal for the crystal truncation rod of the reconstruction decreased with increasing temperature until it is close to the baseline, and increased again upon cooling down. The peaks in SXRD scans from 573 K (300 °C) to 773 K (500°C) were fitted using Lorentzian functions to determine the width at the half-maximal height (FWHM) as a measure for the width, which can be converted to a value for the coherence length, both of which are plotted in figure 4.16c. It shows that the peak height starts to decrease and the width to increase around 723 K when heating up. The correlation length is reduced from approximately 20 nm to 5 nm when heating from 723 K to 771 K.

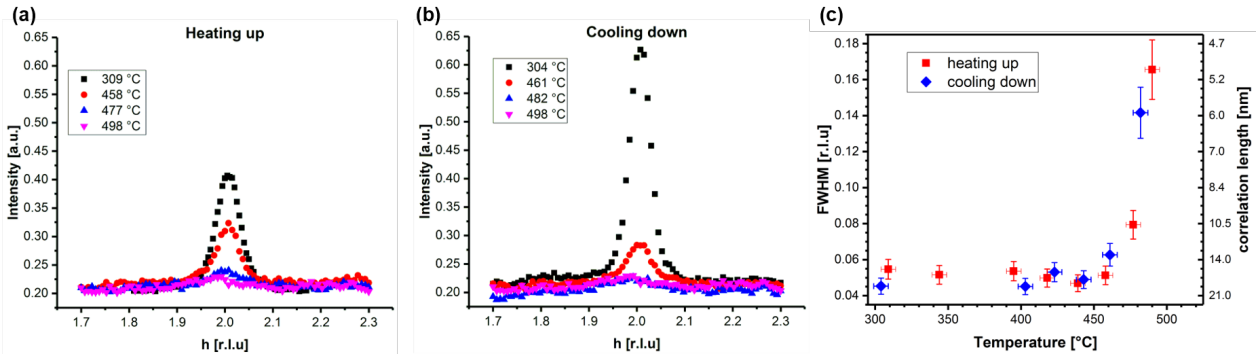

Figure 4.16: (a,b) SXRD scans through the (2,1) surface rod of the $\left(\sqrt{2} \times \sqrt{2}\right)$ R45° reconstruction at L = 1.6 along hte reciprocal h direction while (a) heating and (b) cooling down. (c) The FWHM of the peaks in SXRD rod scans increases with increasing temperature, the correlation length decreases therefore to approx. 5 nm in this range, while the peak height decreases (reproduced from [188]).

Crystal truncation rod scans were performed [188] and an excerpt of them is show in figure 4.17. They compare measurements at the end of the phase transition at 770 K (red markers) to room temperature scans (black markers) and calculated structure factors for a bulk-truncated structure model (continuous brown line) and the fit based on the SCV structure models with added occupation parameters (continuous blue line) show that a bulk-truncated structure does not provide a suitable explanation for the observed phase transition.

The scans of crystal truncation rods displayed in figure 4.17 demonstrate that the surface structure is not simply a transition to a structure based on the hypothetical distorted bulk-truncated structure. The structure factors measured are closer to the SCV structure at room temperature and than to the distorted bulk-truncated model as indicated by the calculated structure factors shown in the scan. Fitting the crystal rod data at 770 K, i.e. above the phase transition temperature, to structural models of the distorted bulk truncation (DBT, an out-of-date model for the RT surface) [189–191] and the SCV structure [72] gives a reduced χ^2 value (χ^2_{red}) of 5.66 (DBT) and 3.88 (SCV), therefore neither model provides a correct fit to data, albeit, in comparison, the SCV model is in better agreement with the data than the DBT model. To improve the model, occupancy parameters for the Fe positions are introduced. Only parameters for the following positions were found to have an influence on the fit: tetrahedral sites in the second layer (bulk-like sites Fe_{tet}, SCV-specific occupied sites $Fe_{tet,int}$, and non-blocked sites $Fe_{tet,vac}$ (from figure 1.7)) and octahedral sites in the third layer (occupied Fe_{oct} and unoccupied $Fe_{oct,vac}$ below the phase transition in the SCV). This is considered

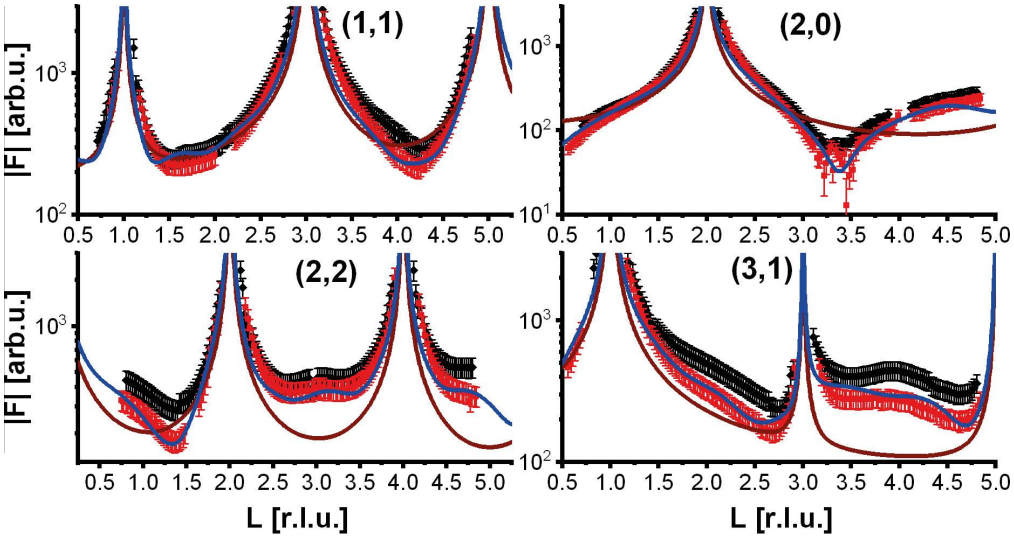

Figure 4.17: Scans of crystal truncation rods of clean $Fe_3O_4(001)$ at room temperature (black markers) and 770 K (red markers). The calculated structure factors for a SCV structure with fitted occupation parameters is shown in blue, and the calculated structure factors for the distorted bulk-truncated structure are indicated in brown, showing that the bulk-truncated model is not correct for either temperature (reproduced from [188]).

as model 1 and yielded a slightly better value for χ^2_{red} of 2.78. Enabling the positions to relax within the symmetry of the reconstruction, first only for the Fe positions (model 2) and then for Fe and O positions (model 3), leads to a great improvement of the fit to a χ^2_{red} of 0.78 for both cases. The comparable χ^2_{red} of the models thus suggests that a distortion of the O positions does not contribute to the phase transition, which is reasonable as magnetite is known for literature to be a material where cationic defect mobility dominates [20]. The results of the different fits are summarized in table 4.1.

Table 4.1: The crystal truncation rods were fitted with three different models based on their free parameters: The occupancies of Fe sites (sites explained in the text) are fitted against the data in model 1. Additionally allowing the refinement of the positions of the Fe sites greatly improved the fit (model 2), while allowing the refinement of the oxygen positions additionally to the Fe positions (model 3) does not change the fit. The reduced χ^2 value and the occupancies for a SCV reconstructed surface and a distorted bulk-truncated (DBT) structure are shown for comparison. The last column gives an average number of iron cations present overall in the sites discussed in this table. The fit results are reproduced from [188].

Model	χ^2_{red}	Refined Positions		Occupancies					**Sum**
		Fe	O	Fe_{tet}	$Fe_{tet,int}$	$Fe_{tet,vac}$	Fe_{oct}	$Fe_{oct,vac}$	
1	2.78	✘	✘	0.90	0.45	0.34	0.70	0.85	**5.69**
2	0.73	✔	✘	0.86	0.62	0.05	0.80	0.58	**5.15**
3	0.73	✔	✔	0.86	0.62	0.05	0.80	0.58	**5.15**
SCV	3.88	✘	✘	1	1	0	1	0	**5**
DBT	5.66	✘	✘	1	0	0	1	1	**6**

From this analysis, the depletion of Fe from the following three sites is found: The two tetrahedral positions in the second surface layer (the bulk-like positions as well as the interstitial position occupied due to the surface reconstruction of the SCV model) and the octahedral positions occupied

at room temperature. Fe_{oct} positions which are vacant at room temperature in the SCV model (but not in the DBT model) start to be occupied during the phase transition. Therefore, the phase transition cannot be caused exclusively by thermal vibrations of the lattice Fe atoms.

Temperature-Calibration by LEED Measurements

LEED measurements are performed to make the results comparable and calibrate small differences in phase transition temperatures between different crystals, since the transition temperature is know to vary by some 10 K, probably due to slight differences in bulk crystal stoichiometry [187]. Figure 4.18 shows the temperature dependent amplitude of the LEED spots for the $\left(\sqrt{2} \times \sqrt{2}\right)$ R45° reconstruction decreasing throughout the phase transition, showing a transition temperature of 725 ± 20 K in good agreement with Bartelt et al [187] and the SXRD data in figure 4.16. For FastSTM measurement, the sample is thermally equilibrated for a much longer time than for the LEED measurement, so the mean value between the two curves can be used here. The heating ramp of 0.2 K per second is on a different timescale while the thermal equilibrium time for FastSTM measurements is many minutes, and therefore the thermal equilibration at each temperature of the FastSTM data is better. Semi-automatic spot profile fitting using a linear model for the background of the spots was performed as described in section 2.2.

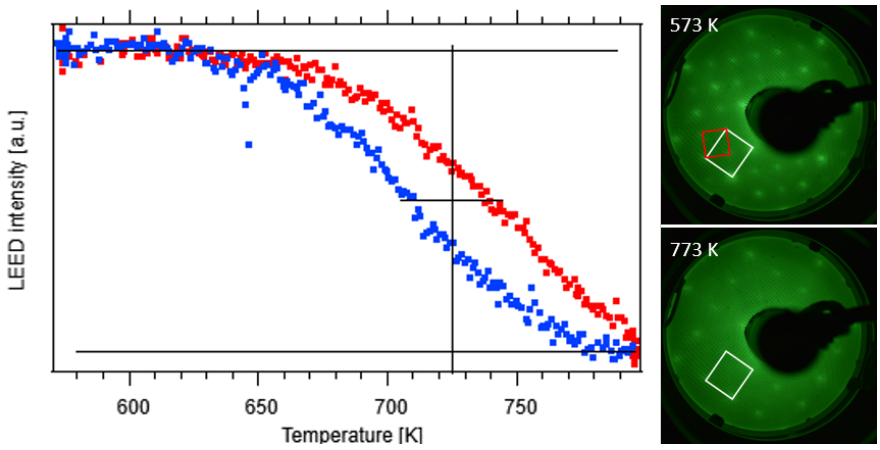

(a)

Figure 4.18: Spot intensity (amplitude) of LEED spots of the $\left(\sqrt{2} \times \sqrt{2}\right)$ R45° reconstruction during a temperature ramp heating up (red) and cooling down (blue). LEED patterns below the phase transition (573 K) and above the phase transition temperature (773 K) are shown on the right. The reciprocal unit cell for the $\left(\sqrt{2} \times \sqrt{2}\right)$ R45° reconstruction is indicated in red, the reciprocal unit cell for the (1×1) surface is indicated in white. The semi-automatic data processing for the LEED data is described in section 2.2.

Real-Space Imaging of the Phase Transition using FastSTM

Here, the first real space study of the phase transition is presented using FastSTM, which has the ability to resolve the surface in real space at temperatures necessary for measuring through the transition temperature, which is hindered for conventional STM as their images would be dominated by highly diffusive species. Averaging a drift corrected FastSTM movie over many consecutive frames gives atomically resolved information of the $Fe_3O_4(001)$ surface and 2D Fourier transform

can indicate the presence of the $\left(\sqrt{2} \times \sqrt{2}\right)$ R45° reconstruction. Care has to be taken to eliminate measurement effects as distortion and drift as described in chapters 3.1 and 3.2. In this study, drift correction is done on a frame-by-frame basis using the StackReg plug-in [132] for ImageJ [131] after frame export from pyfast.

Imaging the $Fe_3O_4(001)$ surface throughout the temperature range of the phase transition and averaging FastSTM frames from the movies gives the images shown in figure 4.19a-c. At the onset

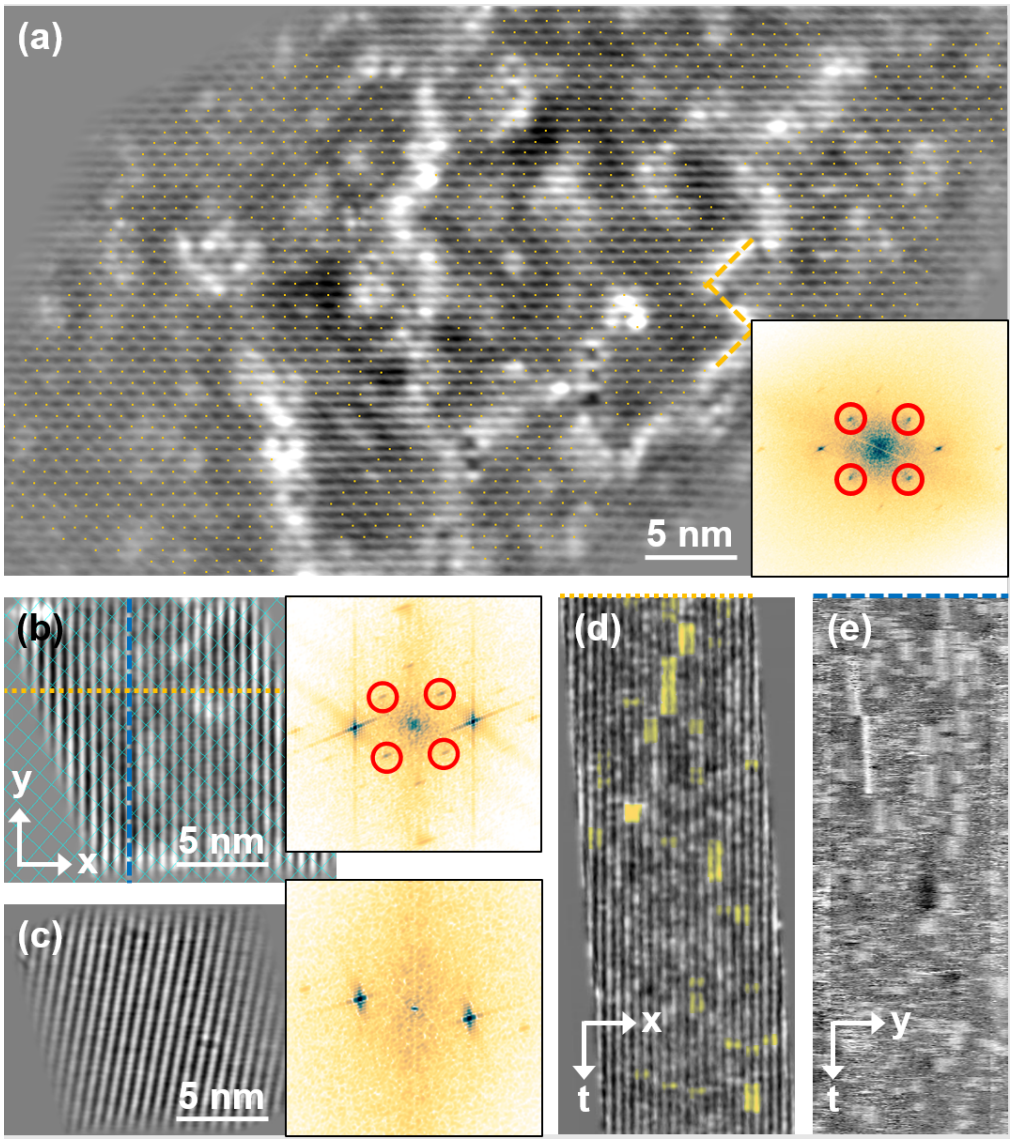

Figure 4.19: FastSTM movie averages at 701 K (a), 747 K (b), and 784 K (c) from onset until beyond the phase transition indicating the SCV unit cells by yellow dots (a) and a cyan grid (b). A APDB is indicated by a dotted orange line. Insets show 2D-FFT plots of the averaged frames with red circles indicate the $\left(\sqrt{2} \times \sqrt{2}\right)$ R45° spots. Above the phase transition (c), the Fe rows appear straight and no $\left(\sqrt{2} \times \sqrt{2}\right)$ R45° spots are visible in 2D-FFT any more. To show the dynamic nature of the surface, the orange line in X direction and the vertical blue line in Y direction in (b) are plotted as a function of time in (d) and (e), respectively. Some examples for double-lobed features are highlighted in yellow.

of the phase transition, the FastSTM image shows that the characteristic undulating rows of the SCV reconstruction of $Fe_3O_4(001)$ are still present (see section 1.3 and [72]). The different domains

are distinguished by marking an unique position in each unit cell with an yellow dot. A dashed line indicates one example of a Fe-rich anti-phase domain boundary present at the surface. More than half-way through the phase transition, at 745 K, the blue grid indicates the lattice of the $\left(\sqrt{2} \times \sqrt{2}\right)$ R45° SCV reconstruction on the FastSTM image in figure 4.19b, showing that the image encompasses only one domain. Heating to a temperature beyond the phase transition, the averaged FastSTM movie does not resolve undulating rows of the SCV any more, as they appear rather straight here.

To make sure that these observations about the periodicity are correct, the 2D-FFT of the three images are take and shown alongside the real-space images in figure 4.19. Spots for the SCV reconstruction in 2D-FFT of the images (circled in red) are visible at the onset (701 K, figure 4.19a) of and halfway through the phase transition (745 K, figure 4.19b), they are no longer visible when measuring beyond the temperature range of the phase transition (784 K, figure 4.19c). More than half-way through the phase transition, at 745 K, a single domain is imaged in figure 4.19b; the blue grid indicates the lattice of the $\left(\sqrt{2} \times \sqrt{2}\right)$ R45° SCV reconstruction, which is clearly visible in the corresponding FFT inset, while the intensity in LEED is decreased by more than half at this temperature.

Turning to the time domain, the FastSTM data shows that the $Fe_3O_4(001)$ surface itself is not static at temperatures around the phase transition. Figures 4.19de show lines and rows from FastSTM plotted as a function of time, respectively, indicating that bright features spanning one and two Fe rows occur and show residence times up to 8 s as the movie is 60 s at 745 K and each row corresponds to one image, therefore more elongation in direction of the t-axis represents a longer residence time of the feature. Double-lobe shaped bright features in STM are commonly associated with unreconstructed unit cells of $Fe_3O_4(001)$ [78]. Isolated single bright features on the Fe rows on images with only one single domain are likely to be caused by interstitial cations in usually vacant octahedral sites in the third layer of the surface reconstruction as found for nickel atoms [192]. In addition to the bright features, occasionally depressions spanning two rows are observed as shown in dark in figure 4.19e. Since lattice dynamics in magnetite are based on Fe dynamics [20], it is justified to assume that these defects are either a result of vertical Fe transport or contaminants in the cation lattice whose diffusion path reach the surface.

Conclusions and Outlook

In all, this study characterizes the $Fe_3O_4(001)$ surface throughout the high-temperature phase transition. The SCV can still be observed in the middle of the phase transition. Upon heating through the phase transition, which is of the order-disorder type, Fe_{tet} atoms in the second layer gain increased lateral mobility - possibly via third layer Fe_{oct} vacancies [184]. The FastSTM data shows indications that some vertical diffusion in the cation lattice starts around and beyond the phase transition temperature. Photoelectron spectroscopy and helium scattering data from Jan Hulva and Gareth S. Parkinson show a relative increase in Fe^{2+}-related states compared to Fe^{3+}-related states and an overall increase of Fe at the surface, which is in good agreement with the SXRD data presented above. The results of this study can provide a basis for the development of catalysts with controlled Fe concentration at the surface by temperature adjustment. Similarly, the ratio between

Fe^{3+} and Fe^{2+} can be changed within a limited range, allowing to tune the electrophilic character of the surface. This might change the adsorption and desorption properties to fit to an optimal range for a desired chemical reaction like the high-temperature water-gas shift reaction. As this reaction is performed with a magnetite-based catalyst in the range of 620 - 720 K and the Fe^{2+}/Fe^{3+} pair is considered the active catalyst for the bulk material [18], the results of this study might help to design a more efficient catalyst. This could improve the conversion rate or save energy costs by lowering the operation temperature. Furthermore, the insights from this study could provide a good starting ground to investigate the high-temperature water-gas shift reaction closer to reaction conditions using the Sniffer developed within this thesis and described in chapter 3.3.

5 Conclusions and Outlook

In this thesis, FastSTM is used to investigate the surface defect dynamics on $\left(\sqrt{2} \times \sqrt{2}\right)$ R45° $Fe_3O_4(001)$ between room temperature and 784 K. Three different dynamic regimes are surveyed in depth: 1) the movement of hydrogen atoms on the surface between room temperature and 382 K, 2) subsurface iron mobility in domain boundaries and iron-rich defects between 353 K and 533 K, and 3) the microscopic processes governing the order-disorder phase transition at approximately 725 K. Furthermore, in this thesis, a highly sensitive instrument for the investigation of surface catalysts has been developed, implemented and tested.

First, FastSTM was used to investigate the dependence of the switching behaviour of hydrogen adatoms on $Fe_3O_4(001)$. On a clean surface, no long-range transport of hydrogen adatoms was observed. The activation energy of the switching motion on the pristine SCV surface is determined to 0.94 ± 0.07 eV with a prefactor of $1 \times 10^{13\pm1}$ Hz via Arrhenius analysis. Taking into account entropic contributions to the Gibbs free energy when using a transition state theory based model did not change the obtained barrier. Analysing hydrogen adatom dynamics at different sites in the same FastSTM movie showed that the switching rate changes strongly next to iron-rich surface defects. The barrier for hydrogen adatoms next to unreconstructed unit cells in $[1\bar{1}0]$ direction were found to move at a much faster speed and their activation energy is estimated to 0.76 eV using the prefactor of 1×10^{13} Hz obtained for the pristine case. This difference is in good agreement with barrier estimates from DFT calculations for both cases. The difference can be explained by a shortening of the distance between the two sites, when an iron rich defect is present in the unit cell neighbouring in $[1\bar{1}0]$ direction. This requires less lattice distortions to reach the transition state and reduces the thermal energy necessary to enable the switching process. On the other extreme of the time scales, it was observed that a hydrogen adatom neighbouring an iron-rich defects in [110] direction shows switching only very rarely that could be barely observed. This shows that proximity to defects can both increase and decrease the switching rate.

Second, mobility of cationic defects on the $\left(\sqrt{2} \times \sqrt{2}\right)$ R45° $Fe_3O_4(001)$ are investigated. Previously not observed zig-zag type motion is observed for defects likely to be unreconstructed unit cells and so-called bright-dark defect s. Anti-phase domain boundaries are found to be mobile at kink sites. The dynamics of these three defects show all move by the same step width in $[1\bar{1}0]$ direction of twice the distance between iron rows. To explain these findings, a tentative model is drawn up, that involves the concerted subsurface displacement of several subsurface iron atoms. Comparing these observations to atomically resolved STM images at room temperature indicate that a minority species of the double-lobed features commonly associated with unreconstructed unit cells are located at non-blocked sites, what would hint at a small energy difference between the two sites. Fe-rich anti-phase domain boundaries dynamics are investigated at 353 K and 413 K. At 353 K, the domain boundaries show exclusively mobility at kink sites, the chains remain intact, and allow a description

as site-exchange consistent with the subsurface cation vacancy structural model. More kinks in a domain boundary consequently lead to increased movement. Heating to 413 K, reversible chain rip-off processes and atypical domain boundary sections along the iron rows were observed. The tentative model provided to explain these two processes might prove to be useful to explain the existence of domain boundaries suddenly ending on a surface terrace and provides a suggestion for the structure of the surface at the intersection of the domains without visible bright domain boundaries ("Fe-poor anti-phase domain boundaries").
Third, the surface dynamics of the $\left(\sqrt{2} \times \sqrt{2}\right)$ R45° reconstruction during the order-disorder phase transition is investigated. The SCV reconstruction could still be resolved more than half-way through the phase transition and is not found any more at temperatures beyond the phase transition. In the middle of the phase transition, multiple mobile defects could still be resolved. Indication for vertical diffusion above the phase transition temperature is found. Together with SXRD [188], this indicates that the phase transition results from increasing mobility of Fe_{tet}, which can diffuse between sites via third-layer Fe_{oct} vacancies in good agreement with theoretical predictions [184].
These studies show that local methods like FastSTM are a powerful tool to investigate dynamics at surfaces and are uniquely positioned to study processes where local information can have outsized influence on the integral behaviour. Furthermore, it allows to *in situ* image dynamic processes at high temperature with increased contrast.
Besides the FastSTM studies, a pulsed high-pressure and high-sensitivity *sniffer* reactor for additional studies in UHV has been designed, constructed, and implemented. It can reproducible pulse very defined amounts of gas onto the sample and detect products in real time with a quadrupole mass spectrometer. As proof-of-principle, the temperature-dependent oxidation of CO over Pt clusters on $Fe_3O_4(001)$ is investigated.
Summarising, this work has established FastSTM as a valuable and reliable tool for variable-temperature surface characterization. Having studied the $Fe_3O_4(001)$ surface between room temperature and 784 K, this thesis paves the way for further studies with size-selected metal clusters. A potential capture zone for hydrogen adatoms around metal clusters could be probed. Taking advantage of sniffer, it could be interesting to investigate how metal clusters influence alcohol reforming by size and metal dependence. Furthermore, the surface diffusion of the reactants and products, alcohols, aldehydes, and ketones, could be studied with FastSTM. Since the reactivity of the water-gas-shift catalyst is dependent on the Fe^{3+}/ Fe^{2+} ratio, the new insights on the high-temperature phase transition may help to understand and exploit this temperature-dependent oxidation state distribution for catalytic purposes.

6 Publications

6.1 Quantitative Investigation of the Dynamics of Hydrogen on $Fe_3O_4(001)$

Alexander Bourgund[1], Barbara A. J. Lechner[1,*], Matthias Meier[2,3], Cesare Franchini[3], Gareth S. Parkinson[2], Ueli Heiz[1], and Friedrich Esch[1]

[1] Chair of Physical Chemistry, Department of Chemistry & Catalysis Research Center, Technical University of Munich, 85748 Garching, Germany.
[2] Institute of Applied Physics, TU Wien, 1040 Vienna, Austria.
[3] Center for Computational Material Science, Faculty of Physics, University of Vienna, 1090 Vienna, Austria.

* corresponding author, E-mail: bajlechner@tum.de

Reprinted with permission from *J. Phys. Chem. C* **2019**, *123*, 19742-19747.

THE JOURNAL OF PHYSICAL CHEMISTRY C

Article

Cite This: J. Phys. Chem. C 2019, 123, 19742−19747

pubs.acs.org/JPCC

Influence of Local Defects on the Dynamics of O−H Bond Breaking and Formation on a Magnetite Surface

Alexander Bourgund,[†] Barbara A. J. Lechner,[*,†] Matthias Meier,[‡,§] Cesare Franchini,[§] Gareth S. Parkinson,[‡] Ueli Heiz,[†] and Friedrich Esch[†]

[†]Chair of Physical Chemistry, Department of Chemistry & Catalysis Research Center, Technical University of Munich, 85748 Garching, Germany

[‡]Institute of Applied Physics, Technische Universität Wien, 1040 Vienna, Austria

[§]Center for Computational Materials Science, Faculty of Physics, University of Vienna, 1090 Vienna, Austria

Supporting Information

ABSTRACT: The transport of H adatoms across oxide supports plays an important role in many catalytic reactions. We investigate the dynamics of H/Fe_3O_4(001) between 295 and 382 K. By scanning tunneling microscopy at frame rates of up to 19.6 fps, we observe the thermally activated switching of H between two O atoms on neighboring Fe rows. This switching rate changes in proximity to a defect, explained by density functional theory as a distortion in the Fe−O lattice shortening the diffusion path. Quantitative analysis yields an apparent activation barrier of 0.94 ± 0.07 eV on a pristine surface. The present work highlights the importance of local techniques in the study of atomic-scale dynamics at defective surfaces such as oxide supports.

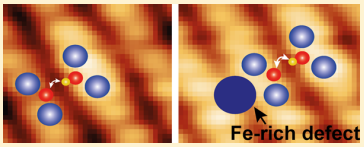

INTRODUCTION

Iron oxides have attracted considerable research interest[1−7] in recent years as supports for heterogeneous catalysts due to their natural abundance[8,9] and nontoxicity. Reactions involving hydrogenation/dehydrogenation steps often require hydrogen diffusion on the support before the hydrogen evolution can take place. A fundamental understanding of the transport behavior of hydrogen on oxide surfaces can help us understand and optimize reaction mechanisms. Sophisticated integral techniques can provide some insights. In a recent study, Karim and co-workers designed a clever experimental layout to distinguish the hydrogen transport between points of different distances.[10] They found that hydrogen diffusion on the reducible titanium oxide surface is ten orders of magnitude faster than on the nonreducible aluminum oxide. In a recent temperature-programmed desorption experiment, Walenta and co-workers showed that even sparsely distributed Pt cocatalysts on the TiO_2(110) surface can facilitate the recombinative desorption of H_2 in the photocatalytic methanol reforming, thus recovering the catalytically active site and closing the catalytic cycle.[11] On some iron oxide surfaces, similar long-range diffusion of hydrogen was observed. On a thin FeO(111) film on Pt(111), for example, hydrogen diffusion occurs readily even at cryogenic temperatures.[12] Using scanning tunneling microscopy (STM), the authors of that study showed that the diffusion could further be facilitated by the presence of coadsorbed water. On the magnetite Fe_3O_4(001) surface, however, only confined diffusion of hydrogen atoms was observed below the water desorption temperature.[13−15] Here, hydrogen can bind to two specific sites in the unit cell of the surface reconstruction and switch between them reversibly.[16,17] In the present work, we investigate the switching between these two adjacent sites at elevated temperatures, i.e., where catalytic reactions most often occur.

Bulk magnetite crystallizes in an inverse spinel structure where Fe^{2+} occupies octahedral sites and Fe^{3+} occupies tetrahedral and octahedral sites in a ratio of 1:1.[18−20] Its (001) surface reconstructs into the subsurface cation vacancy (SCV) structure, where the iron atoms of the uppermost layers are all Fe^{3+}, corresponding to a $(\sqrt{2} \times \sqrt{2})$ $R45°$ reconstruction.[21] Empty-state STM images show characteristic undulating rows of the octahedral iron atoms (see Figure 1). Fe_3O_4(001) has a rich defect chemistry that has been discussed in the literature at length (see also the Supporting Information).[15,22−24] We focus here on the so-called unreconstructed unit cells of the SCV structure, a local region on the surface where the interstitial tetrahedral Fe atom (Fe_{tet}) of the SCV reconstruction is missing and instead two additional Fe atoms are located in octahedral sites (Fe_{oct}) of the third atomic layer.[8,22] The defect is the result of a surplus Fe atom in one Fe_{oct} site (labeled as $+Fe_{oct}$ in Figure 1d) that causes the Fe atom in the tetrahedral site of the second layer to move to the other octahedral site of the third layer (indicated by the dashed arrow in Figure 1d). This unreconstructed defect region corresponds to a genuine (1 × 1) bulk structure unit cell and appears as a double-lobed elongated protrusion in STM (highlighted by the black oval in Figure 1a). Surface hydroxyls (OH groups), in contrast, appear as single protrusions (marked by white ovals in Figure 1a,b). These surface hydroxyl groups result from H adatoms that are formed

Received: June 11, 2019
Revised: July 17, 2019
Published: July 17, 2019

DOI: 10.1021/acs.jpcc.9b05547
J. Phys. Chem. C 2019, 123, 19742−19747

The Journal of Physical Chemistry C Article

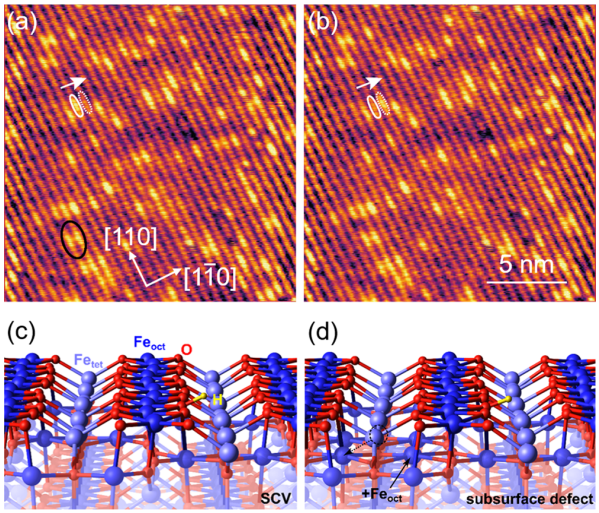

Figure 1. (a) A FastSTM frame illustrates the defects on $Fe_3O_4(001)$ discussed in the present work: a hydroxyl group resulting from an H adatom appears as an elongated protrusion (marked by a solid white oval), while an unreconstructed unit cell appears as a bright double-lobed feature (marked by a black oval). The [1$\bar{1}$0] and [110] crystal directions are marked by white arrows. (b) In the subsequent frame, the hydroxyl group has moved to its neighboring site, out of the solid white oval and into the dashed white oval. Imaging parameters: V_b = 1.50 V; I_t = 1.0 nA. (c, d) Structural models of the SCV-reconstructed $Fe_3O_4(001)$ surface in perspective view obtained from density functional theory (DFT) calculations. (c) Hydroxyl group on the pristine SCV surface and (d) hydroxyl group close to an unreconstructed unit cell site. Note the different arrangement of the cations in the second and third atomic layers. In the bulk-like unreconstructed unit cell (d), an additional Fe_{oct} is located in the third atomic layer (labeled as '+Fe_{oct}') and another Fe atom moves from the second layer Fe_{tet} site of the reconstruction into an Fe_{oct} site of the third layer, as indicated by the dashed arrow.

during the crystal preparation process, where water from the residual gas atmosphere can dissociate at oxygen vacancies.[15]

Here, we present the first quantitative analysis of the H adatom switching between two adjacent O atoms in the $Fe_3O_4(001)$ unit cell to determine the energetics involved in this process. Our FastSTM measurements show that the switching process is an activated one. Furthermore, we find that at a given temperature, the switching frequency increases or decreases depending on the local chemical environment of the hydroxyl group. We therefore compare the switching behavior of hydroxyl groups on the pristine SCV $Fe_3O_4(001)$ surface with ones close to an unreconstructed unit cell.

METHODS

The $Fe_3O_4(001)$ sample was prepared by repeated cycles of sputtering for 5 min in 5 × 10^{-6} mbar Ar at 1.0 kV and subsequent annealing to 983 K in 1.0 × 10^{-6} mbar O_2. Surface hydroxyl groups result naturally from background water dissociation during the annealing process.[15] A boron nitride heater was used to heat the sample, and a type K thermocouple was attached to the crystal to record the temperature. The thermocouple is referenced internally to the chamber temperature. This results in a very high relative accuracy (better than 0.1 K), while the absolute temperature value might have an offset up to 5 K, as confirmed by the order−disorder phase transition of the $Fe_3O_4(001)$ surface at 725 K in low-energy electron diffraction measurements.[25] All STM measurements were performed with an Omicron VT-AFM using etched Pt/Ir tips (Unisoku). Standard STM measurements were performed in constant current mode. A FAST module[26,27] attached to the standard Omicron controller was used to record movies at rates of multiple frames per second (fps). During such FastSTM measurements, the feedback was lowered to only correct for thermal drift but not follow the surface topography and the respective scanning parameters were set before starting the FastSTM measurement. The FastSTM frame rates used for this study were either 4.0 or 19.6 fps. Note that the sinusoidal tip movement in the fast scan direction results in a higher pixel density at the left and right edges of the movie. FastSTM data is recorded as a one-dimensional data stream and subsequently reconstructed into movies with a specially built Python script. Using this software, we level the background by fast Fourier transform (FFT) filtering the frequencies of the fast and slow scan directions and their overtones. We then further FFT filter the known frequencies of the setup (e.g., from turbomolecular pumps), those below the frequency of the fast scan direction, and instabilities from feedback corrections using a broad high-pass damping filter, and finally drift correct the movie. A quantitative analysis was performed by placing oval masks on one of the two locations of a hydroxyl group and integrating over their signal intensity for each frame, as demonstrated in Figure 2. The result is a telegraph noise-like graph illustrating switching between more and less bright appearances, which can be assigned to "H adatom present" and "H adatom absent", respectively. Particular care was taken to distinguish short residence times from tip changes, scratches, and the influence of other mobile defects. The residence times were then plotted as histograms, where the bin width was constrained to

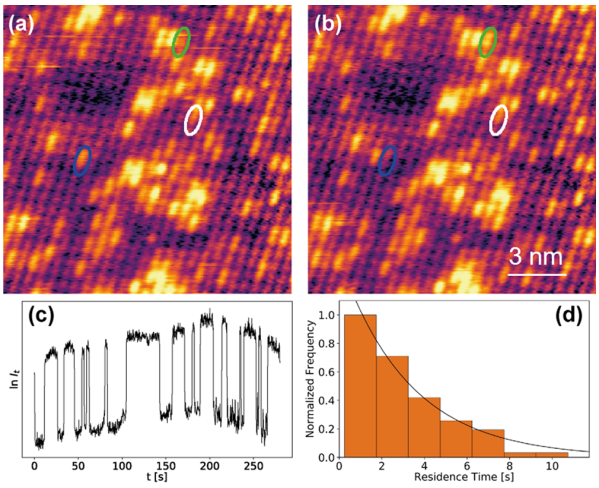

Figure 2. (a, b) Two consecutive frames from a FastSTM movie with multiple switching H adatoms. The blue mask shows a hydroxyl group on the pristine SCV surface that is located in the mask in the first frame and jumped out of it in the second frame. The green and white masks mark hydroxyl species with a defect next to them in the [1$\bar{1}$0] and [110] directions, respectively. The complete movie can be found as Supporting Information Movie S2. Imaging parameters: V_b = 1.50 V; I_t = 1.0 nA; 4 fps. (c) Plotting the signal inside a mask as a function of time (i.e., frame), we obtain a telegraph noise-like trace for a switching H adatom. (d) Residence times extracted from all traces at a given temperature are plotted in a histogram that is then fitted by an exponential function.

DOI: 10.1021/acs.jpcc.9b05547
J. Phys. Chem. C 2019, 123, 19742−19747

multiples of the respective acquisition times for one frame and a single exponential was fitted to the histogram. The mean switching rates and their respective errors were determined from the decay times fitted to bins of a width that created histograms with enough and sufficiently populated bins to properly represent the data. Typically, at least 50 events are included in a histogram at every temperature. A systematic atom tracking study on the diffusion of Si dimers showed that the electric field in a tunneling junction can influence the jump rates but almost exclusively by the prefactor and not by the activation energy.[28] Hence, to avoid systematic errors, all FastSTM movies for H adatom switching analysis were recorded at a bias voltage, V_b, of 1.50 V and a tunneling current, $I_t$of 1.0 nA.

The Vienna ab initio simulation package (VASP)[29,30] was used for all DFT calculations. The projector augmented wave (PAW)[31,32] method describes the electron and ion interactions, with the plane wave basis set cutoff energy set to 550 eV. We used the following settings: a Γ-centered k-mesh of 5 × 5 × 1 for the bulk, $Fd\bar{3}m$, a = 8.396 Å, experimental lattice magnetite cell, and (001) surface calculations (Γ-point only for the 2 × 2 supercell). After preconverging calculations using the Perdew−Burke−Ernzerhof (PBE)[33] functional, where dispersion effects are treated with D2,[34] the obtained results are further relaxed and improved using optB88-DF.[35−38] The PBE + D2[35,36] and optB88-DF van der Waals functionals were used with an effective on-site Coulomb repulsion term U_{eff} = 3.61 eV[39,40] to accurately model the oxide. Calculations were performed on an asymmetric slab with 13 planes (5 fixed and 2 relaxed $Fe_{oct}O_2$ layers) and 14 Å vacuum. To avoid interaction between adsorbates, and to accurately model the experimental coverages, a (2 × 2) supercell was used (i.e., 4 times the ($\sqrt{2}$ × $\sqrt{2}$)R45° reconstructed cell). Transition states are determined via nudged elastic band[41] (NEB) calculations using the climbing-image method. The PBE + D2 functional was used for the NEB calculations, but the energies obtained at the saddle points were further improved using the optB88-DF functional while keeping the ionic position fixed. Convergence is achieved when forces acting on ions become smaller than 0.04 eV/Å.

RESULTS AND DISCUSSION

Making use of the increased frame rates available with FastSTM, we observed the reversible switching of H adatoms, which originate from the sample preparation process, between two adjacent O atoms at room temperature and above in real time. As in previous studies at lower temperatures, we find that the H adatoms switch exclusively between the two O atoms on neighboring iron rows of the surface reconstruction (see Figure 1).[14−16,21] The process is reversible and can be monitored for many minutes to hours in temperature equilibrium. Measurements at different temperatures reveal an increase in the rate of motion with increasing temperature, implying that we are observing an activated process. Two representative movies at 331 and 349 K are shown in Supporting Information Movies S1 and S2, respectively. To determine the Arrhenius activation barrier of the switching process, we identified hydroxyl species by conventional STM imaging and then recorded FastSTM movies of these species at several temperatures. The Arrhenius plot obtained from the mean switching rate of data recorded between 336 and 382 K is shown in Figure 3. Here, only hydroxyl species that are located on a pristine SCV surface are used in the analysis, i.e., those that are located in an SCV-

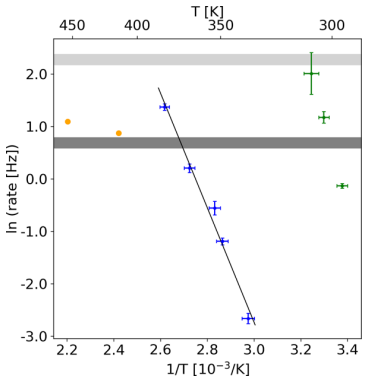

Figure 3. Arrhenius plot for H adatoms switching between two opposite O atoms. Switching rates determined from FastSTM data of species on the pristine SCV surface are shown as blue points and a linear Arrhenius fit as a black line. H adatoms next to unreconstructed unit cells in the [1$\bar{1}$0] direction exhibit a higher jump rate, shown as green points. The dark (4 fps) and light gray (19.6 fps) horizontal bars illustrate the limits of time resolution as described in the text. The orange points represent high-temperature data points measured at 4 fps, demonstrating the effect of undersampling. Switching rates for hydroxyl groups on the pristine SCV surface up to 367 K were acquired at 4 fps, while those at 367 K and higher as well as those for hydroxyls next to unreconstructed unit cells were measured at 19.6 fps.

reconstructed unit cell, as shown in Figure 1c. The rates for switching in one direction or the other are not significantly different within the statistical error of our measurements, i.e., the switching process is a symmetric one (as expected for motion between two equivalent sites). Via orthogonal distance regression, we obtain an Arrhenius activation barrier of 0.94 ± 0.07 eV and a prefactor of 1 × $10^{13\pm1}$ Hz for hydroxyl groups on the pristine SCV surface. To account for entropic contributions to the activation Gibbs free energy, we also fitted the same data taking into account transition state theory (description by Winzor and Jackson in ref 42). As expected for a simple, light adsorbate like a single H atom, compared to larger, molecular adsorbate species,[43] we confirmed that the entropic contribution is negligible and the same activation energy is obtained by both analysis routes.

When extracting residence times from FastSTM movies, care must be taken that the frame rate is sufficient to resolve the process to be studied. As a rule of thumb, we assume that reliable data can only be obtained when the frame rate is at least twice the mean jump rate, i.e., a species is observed on average at least in two consecutive frames. Taking into account the constraints of our instrument (i.e., preamplifier bandwidth, etc.) and keeping the lateral resolution sufficient for reliable analysis, we achieved a maximum frame rate of 19.6 fps in the present work. This corresponds to a maximum time resolution of 9.8 per second, as marked by the light gray bar in Figure 3. In comparison, the more convenient frame rate of 4 fps (allowing us to scan larger areas) gives a limit of 2 per second, marked by the dark gray bar. Data points for the hydroxyl groups on the pristine SCV surface were measured with 4 fps up to 367 K and 19.6 fps at higher temperatures. At 367 K, we further confirmed that data acquisition yielded the same hydroxyl switching rate at 4 fps and at 19.6 fps. To illustrate the effect of undersampling, the switching rates obtained with 4 fps measurements at higher temperatures (413 and 454 K)

DOI: 10.1021/acs.jpcc.9b05547
J. Phys. Chem. C 2019, 123, 19742−19747

The Journal of Physical Chemistry C Article

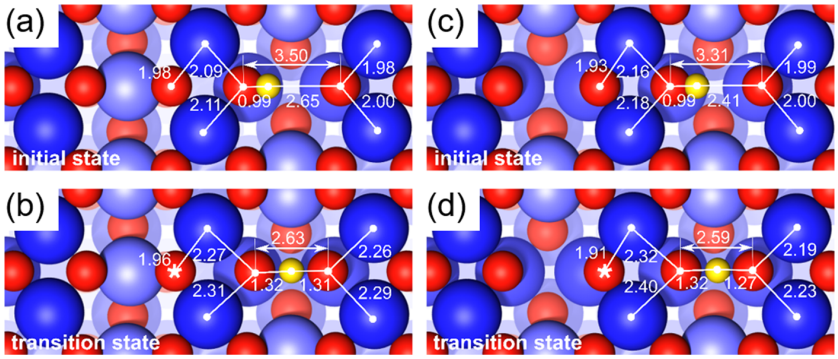

Figure 4. DFT-derived structural models illustrating the diffusion of an H adatom (a, b) on the defect-free $Fe_3O_4(001)$ surface and (c, d) neighboring an unreconstructed unit cell. Top views showing the initial and transition states for H^+ diffusion. The O−O distance is shorter in the initial state neighboring the defect. Nevertheless, the surrounding lattice distorts significantly in the transition state, ultimately achieving a similar O−H bond length in each case.

are shown as orange points in Figure 3. A clear deviation from the linear Arrhenius behavior is seen, and the obtained switching rates are close to the estimated limit marked by the dark gray bar. Indeed, these fast-moving hydroxyl groups often appear as partial protrusions in both locations in single frames. However, even at 450 K, where we cannot resolve the motion temporally, streaks between two neighboring iron rows confirm that the H adatoms only move between these two locations and do not diffuse laterally across larger distances.

Furthermore, we observed that switching rates of hydroxyl groups in the vicinity of defects differ significantly from the ones on the pristine SCV surface. On the one hand, hydroxyl species directly neighboring unreconstructed unit cells in the $[1\bar{1}0]$ direction (i.e., jumping to an iron row next to the defect, marked by the green mask in Figure 2a,b) switch more often in the temperature range considered in this study than those on the pristine SCV surface. Mean switching rates for such species are shown as green points in Figure 3. Just like for the species on the pristine SCV surface, we do not observe a statistically significant, systematic asymmetry in the switching rates towards and away from the defect. Assuming that only the path difference plays a role in the switching behavior in different local environments (substantiated by our DFT results which will be discussed below), we can estimate an Arrhenius activation barrier for OH switching next to an unreconstructed unit cell of 0.76 eV using the prefactor of 1×10^{13} Hz that we obtained for the hydroxyl species on the pristine surface. Due to the increased rate, we are now hitting the limit of our time resolution at 308 K already, even with an acquisition rate of 19.6 fps. On the other hand, switching events of those hydroxyl groups neighboring the unreconstructed unit cell in the [110] direction (i.e., a neighbor along the row, as marked by the white mask in Figure 2a,b) are switching much less frequently. Since the events are rare, we do not observe a sufficient number of them to obtain a reliable switching rate, but we estimate the rate to be approximately 0.07 Hz at a temperature of 349 K. Finally, the influence of defects is a short-range effect. We do not observe any influence on hydroxyl groups that are located one unit cell further away from a defect.

We performed DFT calculations of hydroxyl groups on a pristine SCV surface and next to an unreconstructed unit cell to better understand the experimental results. In the case of a hydroxyl group on a pristine SCV surface, an activation barrier of 1.27 eV was obtained. Where an unreconstructed unit cell is adjacent to the hydroxyl in the $[1\bar{1}0]$ direction, the activation barrier is lowered by 0.27 to a value of 1.00 eV. While the temperature range available in our experiment for the accelerated hydroxyl species is insufficient to obtain an Arrhenius activation barrier, we can compare the switching rate between species on the pristine SCV surface and those near a defect and relate these to the DFT results. Our calculations show that the diffusion mechanism remains the same in both cases. Assuming that the prefactor remains unchanged, the switching rate should thus be higher next to the defect. Assuming a reversible process with no entropy change, the energy difference of 0.27 eV corresponds to an approximately 100 K difference in temperature for a given rate, which is in good agreement with the experimental results shown in Figure 3. Furthermore, DFT confirms that the process is a symmetric one in both cases, with energy differences between the initial and final states of 0.08 and 0.06 eV for the hydroxyl group on a pristine SCV surface and that next to a defect, respectively, which are both within common fluctuations present in the calculations. The DFT results are thus consistent with the experimentally obtained jump rates and activation barriers.

Analyzing the structures obtained from DFT (shown in Figures 1c,d and 4), we note that the presence of the defect shortens the O−O distance in the initial state from 3.50 to 3.31 Å. In principle, this should facilitate a lower barrier, but this distance is still far too long for the H adatom to simply hop on a rigid lattice. Rather, the O−O distance must contract significantly to approximately 2.6 Å to create the transition state, where O−H bonds of 1.3 Å are simultaneously established to both the initial and target O atoms. This situation is similar for both models considered here. Facilitating the transition state requires that both the O atoms and the second nearest-neighbor surface Fe atoms must move toward the H adatom, i.e., toward each other. Thus, it seems that the different barrier actually originates in the cumulative energetic cost of multiple distortions to the surrounding atoms that must occur to facilitate the hydrogen transfer. Ultimately, a lower barrier is observed in the presence of the unreconstructed unit cell because less distortion of the lattice is required to form the transition state. This is seen, for example, in the Fe−O distances for the target O atom, which are approximately 0.1 Å shorter in the transition state when the defect is present than on the pristine SCV surface (compare

DOI: 10.1021/acs.jpcc.9b05547
J. Phys. Chem. C 2019, 123, 19742−19747

Figure 4b,d). Interestingly, the Fe−O distances are slightly longer to the initial O atom in the presence of the defect. This relaxation seems to be compensated by the stronger interaction with the O atom labeled as * in Figure 4b,d, which can move closer to the surface Fe_{oct} atoms when it is coordinated to a subsurface Fe_{oct} rather than an Fe_{tet}.

CONCLUSIONS

In conclusion, we have shown that the diffusion of H adatoms on $Fe_3O_4(001)$, which occurs only between two neighboring O atoms on opposite Fe rows, is an activated process. By conducting FastSTM measurements at temperatures between 295 and 382 K, we obtained an apparent Arrhenius activation energy of 0.94 ± 0.07 eV for hydroxyl groups on the pristine SCV-reconstructed surface. This result is in good agreement with DFT calculations that provide an activation barrier of 1.27 eV, especially when keeping in mind that the optB88-DF van der Waals functional used here is typically overbinding.[44] Taking into account the transition state theory to consider changes in entropy in the transition state, we determined that the experimentally obtained activation barrier results purely from energetics and does not contain any entropic contributions. Furthermore, we could not resolve any long-range diffusion of hydrogen up to approximately 550 K, at which point hydrogen is known to desorb from the surface.[15]

Importantly, our local measurements show that the activation barrier and thus the jump rate of individual species vary significantly with their local chemical environment. This effect is generally observed for a range of different local defects such as domain boundaries or adatoms. We have studied the phenomenon in detail for hydroxyl species next to the so-called unreconstructed unit cell, i.e., a region on the surface where the interstitial Fe_{tet} of the SCV reconstruction is missing but instead two more Fe atoms are located in Fe_{oct} sites in the subsurface. Our experiments showed that the switching rate of hydroxyl groups can both increase and decrease, depending on the exact location of the H adatom with respect to the defect. We explained this phenomenon by DFT calculations that show that a distortion in the Fe−O lattice brings the two neighboring O atoms closer together and thus facilitates H diffusion between them. The different energy barriers originate from the cumulative energetic cost of multiple distortions to the surrounding atoms that occur during the switching process. Less lattice distortion is thus required in the presence of defects such as a neighboring unreconstructed unit cell.

The fact that defect proximity governs the activation energy of diffusion processes highlights the importance of local techniques such as STM when it comes to investigating surface dynamics.

ASSOCIATED CONTENT

Supporting Information

The Supporting Information is available free of charge on the ACS Publications website at DOI: 10.1021/acs.jpcc.9b05547.

Several switching hydroxyl groups at 331 K; imaging parameters: V_b = 1.50 V, I_t = 1.0 nA, and 4 fps (Movie S1) (MP4)

Several switching hydroxyl groups at 349 K; imaging parameters: V_b = 1.50 *V*, I_t = 1.0 nA, and 4 fps (Movie S2) (MP4)

Structure of the $Fe_3O_4(001)$ surface and common defects; and diagram illustrating the energies and barriers of all processes calculated by DFT (PDF)

AUTHOR INFORMATION

Corresponding Author

*E-mail: bajlechner@tum.de.

ORCID

Barbara A. J. Lechner: 0000-0001-9974-1738
Gareth S. Parkinson: 0000-0003-2457-8977
Ueli Heiz: 0000-0002-9403-1486
Friedrich Esch: 0000-0001-7793-3341

Notes

The authors declare no competing financial interest.

ACKNOWLEDGMENTS

The authors would like to thank Zdenek Jakub for help with the initial sample preparation and John Ellis for useful discussions regarding the residence time distribution of binary switching events. This work was funded by the Deutsche Forschungsgemeinschaft (DFG, German Research Foundation) under research grants ES 349/1-2 and HE 3454/18-2 and under Germany's Excellence Strategy, EXC 2089/1−390776260, and by the EU-H2020 Research and Innovation Programme under grant agreement no. 654360 NFFA-Europe. B.A.J.L. gratefully acknowledges a Research Fellowship from the Alexander von Humboldt Foundation, a Marie Skłodowska-Curie Individual Fellowship under grant ClusterDynamics (no. 703972) from the European Union's Horizon 2020 research and innovation program, and financial support from the Young Academy of the Bavarian Academy of Sciences and Humanities. G.S.P. and M.M. acknowledge funding from the Austrian Science Foundation (FWF) Start Prize Y847-N20. The computational results were achieved in part using the Vienna Scientific Cluster (VSC 3).

REFERENCES

(1) Bliem, R.; Van Der Hoeven, J.; Zavodny, A.; Gamba, O.; Pavelec, J.; De Jongh, P. E.; Schmid, M.; Diebold, U.; Parkinson, G. S. An Atomic-Scale View of CO and H_2 Oxidation on a Pt/Fe_3O_4 Model Catalyst. *Angew. Chem., Int. Ed.* **2015**, *54*, 13999−14002.

(2) Müllner, M.; Riva, M.; Kraushofer, F.; Schmid, M.; Parkinson, G. S.; Mertens, S. F. L.; Diebold, U. Stability and Catalytic Performance of Reconstructed $Fe_3O_4(001)$ and $Fe_3O_4(110)$ Surfaces during Oxygen Evolution Reaction. *J. Phys. Chem. C* **2019**, *123*, 8304−8311.

(3) Kim, Y. K.; Zhang, Z.; Parkinson, G. S.; Li, S.-C.; Kay, B. D.; Dohnálek, Z. Reactivity of FeO(111)/Pt(111) with Alcohols. *J. Phys. Chem. C* **2009**, *113*, 20020−20028.

(4) Parkinson, G. S.; Novotny, Z.; Argentero, G.; Schmid, M.; Pavelec, J.; Kosak, R.; Blaha, P.; Diebold, U. Carbon Monoxide-Induced Adatom Sintering in a Pd-Fe_3O_4 Model Catalyst. *Nat. Mater.* **2013**, *12*, 724−728.

(5) Bliem, R.; van der Hoeven, J. E. S.; Hulva, J.; Pavelec, J.; Gamba, O.; de Jongh, P. E.; Schmid, M.; Blaha, P.; Diebold, U.; Parkinson, G. S. Dual Role of CO in the Stability of Subnano Pt Clusters at the $Fe_3O_4(001)$ Surface. *Proc. Natl. Acad. Sci. U.S.A.* **2016**, *113*, 8921−8926.

(6) Parkinson, G. S. Single-Atom Catalysis: How Structure Influences Catalytic Performance. *Catal. Lett.* **2019**, *149*, 1137−1146.

(7) Weng, X.; Zhang, K.; Pan, Q.; Martynova, Y.; Shaikhutdinov, S.; Freund, H.-J. Support Effects on CO Oxidation on Metal-Supported Ultrathin FeO(111) Films. *ChemCatChem* **2017**, *9*, 705−712.

(8) Parkinson, G. S. Iron Oxide Surfaces. *Surf. Sci. Rep.* **2016**, *71*, 272−365.

DOI: 10.1021/acs.jpcc.9b05547
J. Phys. Chem. C 2019, 123, 19742−19747

(9) Holleman, A. F.; Wiberg, E.; Wiberg, N.; Fischer, G. *Lehrbuch Der Anorganische Chemie*, 102nd ed.; Walter de Gruyter: Berlin, New York, 2007.
(10) Karim, W.; Spreafico, C.; Kleibert, A.; Gobrecht, J.; VandeVondele, J.; Ekinci, Y.; van Bokhoven, J. A. Catalyst Support Effects on Hydrogen Spillover. *Nature* **2017**, *541*, 68−71.
(11) Walenta, C. A.; Kollmannsberger, S. L.; Courtois, C.; Pereira, R. N.; Stutzmann, M.; Tschurl, M.; Heiz, U. Why Co-Catalyst-Loaded Rutile Facilitates Photocatalytic Hydrogen Evolution. *Phys. Chem. Chem. Phys.* **2019**, *21*, 1491−1496.
(12) Merte, L. R.; Peng, G.; Bechstein, R.; Rieboldt, F.; Farberow, C. A.; Grabow, L. C.; Kudernatsch, W.; Wendt, S.; Lægsgaard, E.; Mavrikakis, M.; et al. Water-Mediated Proton Hopping on an Iron Oxide Surface. *Science* **2012**, *336*, 889−893.
(13) Peden, C. H. F.; Herman, G. S.; Z. Ismagilov, I.; Kay, B. D.; Henderson, M. A.; Kim, Y.-J.; Chambers, S. A. Model Catalyst Studies with Single Crystals and Epitaxial Thin Oxide Films. *Catal. Today* **1999**, *51*, 513−519.
(14) Parkinson, G. S.; Novotný, Z.; Jacobson, P.; Schmid, M.; Diebold, U. Room Temperature Water Splitting at the Surface of Magnetite. *J. Am. Chem. Soc.* **2011**, *133*, 12650−12655.
(15) Meier, M.; Hulva, J.; Jakub, Z.; Pavelec, J.; Setvin, M.; Bliem, R.; Schmid, M.; Diebold, U.; Franchini, C.; Parkinson, G. S. Water Agglomerates on $Fe_3O_4(001)$. *Proc. Natl. Acad. Sci. U.S.A.* **2018**, *115*, E5642−E5650.
(16) Parkinson, G. S.; Mulakaluri, N.; Losovyj, Y.; Jacobson, P.; Pentcheva, R.; Diebold, U. Semiconductor−Half Metal Transition at the $Fe_3O_4(001)$ Surface upon Hydrogen Adsorption. *Phys. Rev. B* **2010**, *82*, No. 125413.
(17) Hiura, S.; Ikeuchi, A.; Shirini, S.; Subagyo, A.; Sueoka, K. Effect of Adsorbed H Atoms on the Fe Electronic States of $Fe_3O_4(001)$ Film Surfaces. *Phys. Rev. B* **2015**, *91*, No. 205411.
(18) Bragg, W. H. The Structure of Magnetite and the Spinels. *Nature* **1915**, *95*, No. 561.
(19) Verwey, E. J. W.; Heilmann, E. L. Physical Properties and Cation Arrangement of Oxides with Spinel Structures I. Cation Arrangement in Spinels. *J. Chem. Phys.* **1947**, *15*, 174−180.
(20) Verwey, E. J.; Haayman, P. W.; Romeijn, F. C. Physical Properties and Cation Arrangement of Oxides with Spinel Structures II. Electronic Conductivity. *J. Chem. Phys.* **1947**, *15*, 181−187.
(21) Bliem, R.; McDermott, E.; Ferstl, P.; Setvin, M.; Gamba, O.; Pavelec, J.; Schneider, M. A.; Schmid, M.; Diebold, U.; Blaha, P.; et al. Subsurface Cation Vacancy Stabilization of the Magnetite (001) Surface. *Science* **2014**, *346*, 1215−1218.
(22) Gamba, O.; Hulva, J.; Pavelec, J.; Bliem, R.; Schmid, M.; Diebold, U.; Parkinson, G. S. The Role of Surface Defects in the Adsorption of Methanol on $Fe_3O_4(001)$. *Top. Catal.* **2017**, *60*, 420−430.
(23) Gamba, O.; Noei, H.; Pavelec, J.; Bliem, R.; Schmid, M.; Diebold, U.; Stierle, A.; Parkinson, G. S. Adsorption of Formic Acid on the $Fe_3O_4(001)$ Surface. *J. Phys. Chem. C* **2015**, *119*, 20459−20465.
(24) Hulva, J.; Jakub, Z.; Novotny, Z.; Johansson, N.; Knudsen, J.; Schnadt, J.; Schmid, M.; Diebold, U.; Parkinson, G. S. Adsorption of CO on the $Fe_3O_4(001)$ Surface. *J. Phys. Chem. B* **2018**, *122*, 721−729.
(25) Bartelt, N. C.; Nie, S.; Starodub, E.; Bernal-Villamil, I.; Gallego, S.; Vergara, L.; McCarty, K. F.; De La Figuera, J. Order−Disorder Phase Transition on the (100) Surface of Magnetite. *Phys. Rev. B* **2013**, *88*, No. 235436.
(26) Esch, F.; Dri, C.; Spessot, A.; Africh, C.; Cautero, G.; Giuressi, D.; Sergo, R.; Tommasini, R.; Comelli, G. The FAST Module: An Add-on Unit for Driving Commercial Scanning Probe Microscopes at Video Rate and Beyond. *Rev. Sci. Instrum.* **2011**, *82*, No. 053702.
(27) Dri, C.; Panighel, M.; Tiemann, D.; Patera, L. L.; Troiano, G.; Fukamori, Y.; Knoller, F.; Lechner, B. A. J.; Cautero, G.; Giuressi, D.; et al. The New FAST Module: A Portable and Transparent Add-on Module for Time-Resolved Investigations with Commercial Scanning Probe Microscopes. *Ultramicroscopy* **2019**, *205*, 49−56.
(28) Carpinelli, J. M.; Swartzentruber, B. Direct Measurement of Field Effects on Surface Diffusion. *Phys. Rev. B* **1998**, *58*, R13423−R13425.
(29) Kresse, G.; Furthmüller, J. Efficiency of Ab-Initio Total Energy Calculations for Metals and Semiconductors Using a Plane-Wave Basis Set. *Comput. Mater. Sci.* **1996**, *6*, 15−50.
(30) Kresse, G.; Hafner, J. Ab Initio Molecular Dynamics for Open-Shell Transition Metals. *Phys. Rev. B* **1993**, *48*, 13115−13118.
(31) Blöchl, P. E. Projector Augmented-Wave Method. *Phys. Rev. B* **1994**, *50*, 17953−17979.
(32) Kresse, G.; Joubert, D. From Ultrasoft Pseudopotentials to the Projector Augmented-Wave Method. *Phys. Rev. B* **1999**, *59*, 1758−1775.
(33) Perdew, J. P.; Burke, K.; Ernzerhof, M. Generalized Gradient Approximation Made Simple. *Phys. Rev. Lett.* **1996**, *77*, 3865−3868.
(34) Grimme, S. Semiempirical GGA-Type Density Functional Constructed with a Long-Range Dispersion Correction. *J. Comput. Chem.* **2006**, *27*, 1787−1799.
(35) Dion, M.; Rydberg, H.; Schröder, E.; Langreth, D. C.; Lundqvist, B. I. Van Der Waals Density Functional for General Geometries. *Phys. Rev. Lett.* **2004**, *92*, No. 246401.
(36) Klimeš, J.; Bowler, D. R.; Michaelides, A. A Critical Assessment of Theoretical Methods for Finding Reaction Pathways and Transition States of Surface Processes. *J. Phys. Condens. Matter* **2010**, *22*, No. 074203.
(37) Lee, K.; Murray, É. D.; Kong, L.; Lundqvist, B. I.; Langreth, D. C. Higher-Accuracy van Der Waals Density Functional. *Phys. Rev. B* **2010**, *82*, No. 081101.
(38) Román-Pérez, G.; Soler, J. M. Efficient Implementation of a van Der Waals Density Functional: Application to Double-Wall Carbon Nanotubes. *Phys. Rev. Lett.* **2009**, *103*, No. 096102.
(39) Bernal-Villamil, I.; Gallego, S. Electronic Phase Transitions in Ultrathin Magnetite Films. *J. Phys. Condens. Matter* **2015**, *27*, No. 293202.
(40) Kiejna, A.; Ossowski, T.; Pabisiak, T. Surface Properties of the Clean and Au/Pd Covered $Fe_3O_4(111)$: DFT and DFT+U Study. *Phys. Rev. B* **2012**, *85*, No. 125414.
(41) Henkelman, G.; Jónsson, H. Improved Tangent Estimate in the Nudged Elastic Band Method for Finding Minimum Energy Paths and Saddle Points. *J. Chem. Phys.* **2000**, *113*, 9978−9985.
(42) Winzor, D. J.; Jackson, C. M. Interpretation of the Temperature Dependence of Equilibrium and Rate Constants. *J. Mol. Recognit.* **2006**, *19*, 389−407.
(43) Ditze, S.; Stark, M.; Buchner, F.; Aichert, A.; Jux, N.; Luckas, N.; Görling, A.; Hieringer, W.; Hornegger, J.; Steinrück, H.-P.; et al. On the Energetics of Conformational Switching of Molecules at and Close to Room Temperature. *J. Am. Chem. Soc.* **2014**, *136*, 1609−1616.
(44) Gillan, M. J.; Alfè, D.; Michaelides, A. Perspective: How Good Is DFT for Water? *J. Chem. Phys.* **2016**, *144*, No. 130901.

DOI: 10.1021/acs.jpcc.9b05547
J. Phys. Chem. C 2019, 123, 19742−19747

Supporting Information

for

Influence of Local Defects on the Dynamics of O-H Bond Breaking and Formation on a Magnetite Surface

Alexander Bourgund,[1] Barbara A. J. Lechner,[1,] Matthias Meier,[2,3] Cesare Franchini,[3] Gareth S. Parkinson,[2] Ueli Heiz[1] and Friedrich Esch[1]*

[1] Chair of Physical Chemistry, Department of Chemistry & Catalysis Research Center, Technical University of Munich, 85748 Garching, Germany

[2] Institute of Applied Physics, Technische Universität Wien, 1040 Vienna, Austria

[3] Center for Computational Materials Science, Faculty of Physics, University of Vienna, 1090 Vienna, Austria

* bajlechner@tum.de

a) Structure of the $Fe_3O_4(001)$ surface and common defects

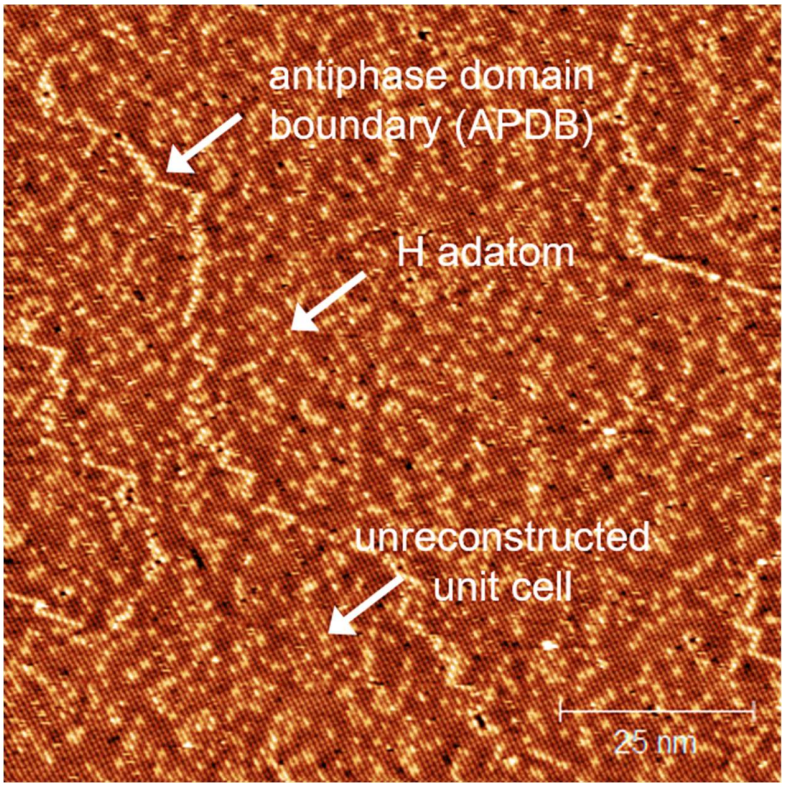

Figure S1: A large-scale STM image shows a typical preparation of the $Fe_3O_4(001)$ surface, including the most common defects (marked by white arrows). The undulating Fe rows are clearly visible through electronic contrast (the O atoms of the surface are not observed by STM), oriented here in the direction from the top left of the image to the bottom center. We find a monophase termination of one large terrace, with several domains of the $(\sqrt{2}\times\sqrt{2})R45°$ reconstruction, separated by antiphase domain boundaries which zigzag across the rows in a 45° orientation. *Imaging parameters:* $V_b = 1.50\ V, I_t = 0.3\ nA$.

b) Diagram illustrating the energies and barriers of all processes calculated by DFT

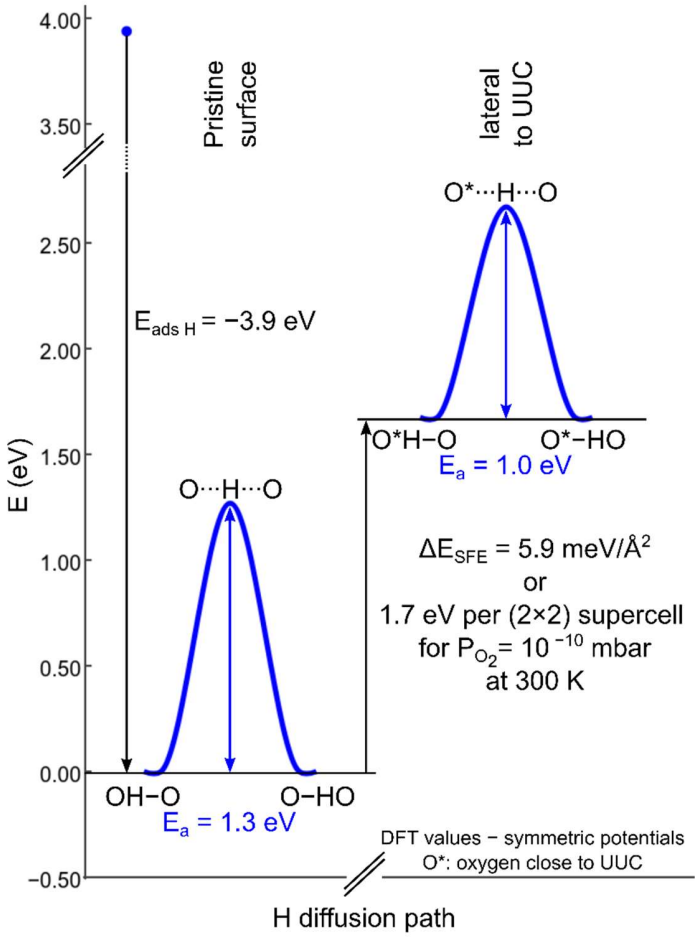

Figure S2: Energy diagram summarizing the energies and barriers from DFT calculations. The left-hand side shows the energy barrier for the switching process of a hydroxyl group on the pristine surface, while the case of a switching hydroxyl group next to an unreconstructed unit cell (UUC) defect is shown on the right-hand side. The adsorption energy of H is given with respect to H (rather than H_2) in the gas phase as $E_{ads} = E_{slab\ with\ H} - E_{clean\ slab} - E_{H\ gas}$. The difference in surface free energy (SFE) between the two cases is given as ΔE_{SFE}.[1,2] The SFE is a function of the chemical potential of O and H, but since only a relative difference is required, the chemical potential of H can be set constant as the amount of H is the same in both cases. The chemical potential of O is taken for a pressure of O_2 of $p_{O_2} = 10^{-10}$ mbar at 300 K, corresponding to experiments under ultra-high vacuum conditions.[3] To estimate

roughly how much the formation of a defect costs energetically, we multiply the SFE difference of $\Delta E_{SFE} = 5.9$ meV/Å^2 with the area of a 2×2 supercell, i.e. assuming one defect every four unit cells (an upper limit for defect density which can realistically be expected to occur). As expected, we find that the defect is unfavorable compared to the SCV reconstruction, irrespective of the presence of an H adatom.

References

(1) Reuter, K.; Scheffler, M. Composition, Structure, and Stability of RuO_2(110) as a Function of Oxygen Pressure. *Phys. Rev. B* **2001**, *65*, 035406.

(2) Reuter, K.; Scheffler, M. Erratum: Composition, Structure, and Stability of RuO_2(110) as a Function of Oxygen Pressure [Phys. Rev. B 65, 035406 (2001)]. *Phys. Rev. B* **2007**, *75*, 049901.

(3) Chase, M. W., Jr., NIST-JANAF Themochemical Tables, Fourth Edition. In *NIST Chemistry WebBook;* Linstrom, P. J., Mallard, W. G. Eds; NIST Standard Reference Database Number 69, National Institute of Standards and Technology: Gaithersburg, MD, http://webbook.nist.gov, (retrieved July 11, 2019).

6.2 Order-Disorder Phase Transition of the Subsurface Cation Vacancy Reconstruction on $Fe_3O_4(001)$

Björn Arndt[1,2], Barbara A. J. Lechner[3,*], **Alexander Bourgund**[3], Elin Grånäs[1], Marcus Creutzburg[1,2], Konstantin Krausert[1,2], Jan Hulva[4], Gareth S. Parkinson[4], Michael Schmid[4], Vedran Vonk[1], Friedrich Esch[3], and Andreas Stierle[1,2,*]

[1] Deutsches Elektronen-Synchrotron (DESY), 22607 Hamburg, Germany.
[2] University of Hamburg, 20355 Hamburg, Germany.
[3] Chair of Physical Chemistry, Department of Chemistry & Catalysis Research Center, Technical University of Munich, 85748 Garching, Germany.
[4] Institute of Applied Physics, TU Wien, 1040 Vienna, Austria.

* corresponding authors, E-mail: bajlechner@tum.de, andreas.stierle@desy.de

Manuscript draft was submitted to *Chemistry of Materials* on January 10, 2020.

Order-disorder phase transition of the subsurface cation vacancy reconstruction on $Fe_3O_4(001)$

Björn Arndt,[†,‡] Barbara A. J. Lechner,[*,¶] Alexander Bourgund,[¶] Elin Grånäs,[†] Marcus Creutzburg,[†,‡] Konstantin Krausert,[†,‡] Jan Hulva,[§] Gareth S. Parkinson,[§] Michael Schmid,[§] Vedran Vonk,[†] Friedrich Esch,[‖] and Andreas Stierle[*,†,‡]

†*Deutsches Elektronen-Synchrotron (DESY), D-22607 Hamburg*

‡*University of Hamburg, Physics Department, D-20355 Hamburg*

¶*Department of Chemistry & Catalysis Research Center, Technical University of Munich, D-85748 Garching*

§*Institute of Applied Physics, TU Wien, A-1040 Vienna*

‖*Department of Chemistry and Catalysis Research Center, Technical University of Munich, D-85748 Garching*

E-mail: bajlechner@tum.de; andreas.stierle@desy.de

Abstract

We present surface X-ray diffraction and fast scanning tunneling microscopy results to elucidate the nature of the surface phase transition on magnetite (001) from a $(\sqrt{2} \times \sqrt{2})$R45° reconstructed to a non-reconstructed surface around 720 K. In-situ surface x-ray diffraction results at a temperature above the phase transition, at which long range order is lost, give evidence that the subsurface cation vacancy reconstruction still exists as a local structural motif, inline with the characteristics of a 2D second-order phase transition. Fast scanning tunneling microscopy results across the phase transition underpin the hypothesis that the reconstruction lifting is initiated by surplus

Fe ions occupying subsurface octahedral vacancies. The reversible near-surface iron enrichment and reduction of the surface is further confirmed by in-situ low-energy ion scattering, as well as ultraviolet and X-ray photoemission results.

Keywords

Magnetite, defects, spinels, oxide surfaces, diffusion, scanning tunneling microscopy, surface x-ray diffraction

Introduction

Magnetite is a material used in many different areas. Its electronic and magnetic properties make it a promising material for spintronics. Its magnetism and biocompatibility triggered development of magnetite nanoparticles for use in waste-water cleaning[1] and application in cancer treatment.[2,3] In addition, it is used as a catalyst for several different reactions, such as the high-temperature water-gas shift reaction.[4,5] For hierarchical materials, magnetite in form of nanoparticles linked together by organic molecules as a first building block shows remarkable mechanical properties.[6,7] Since these applications depend on surface properties such as adsorption sites, binding strength and geometries, which are closely related to the surface structure, determining and understanding the surface structure is vital to get an understanding of the surface properties and therefore of the parameters that determine the performance of the material.

The surface structure of the (001) surface of magnetite, one of the predominant facets on nanoparticles,[6] was studied extensively at room temperature. When prepared in ultra-high vacuum, it exhibits a $(\sqrt{2} \times \sqrt{2})$R45° reconstruction based on a reordering of cations in the near-surface layers.[8,9] Compared to a bulk-truncated surface, it contains one additional iron cation in a tetrahedral site of the second layer, and two octahedral vacancies in the third layer directly underneath.[8,9] A perspective view of both the reconstructed surface and the

bulk terminated surface is shown in Figure 1. This surface was found to be stable over a large

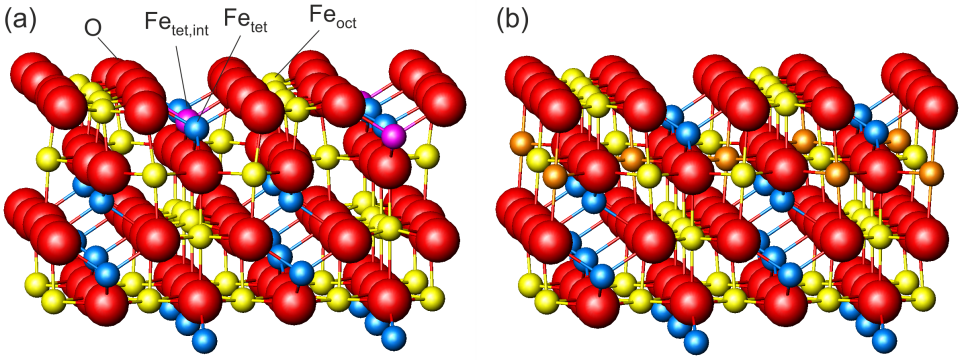

Figure 1: Perspective view of (a) the reconstructed surface and (b) a bulk-truncated surface. Oxygen is shown in red, octahedral iron in yellow and tetrahedral iron in blue. The additional tetrahedral iron atom in the first subsurface layer is shown in violet, and atoms that get removed from octahedral sites when forming the reconstructed surface are orange in the bulk-truncated surface.

range of oxygen chemical potentials.[8] Many of the aforementioned applications, however, require temperatures above room temperature. One obvious example is the high-temperature water-gas shift reaction, which is performed at temperatures between 620 and 720 K. But also the synthesis and pre-processing of the material is often done at elevated temperatures - as the interlinking of organic molecules for the formation of hierarchical materials, which requires heating to temperatures up to 620 K.[6] Iron cations are relatively mobile in magnetite, which can lead to incorporation of metal adatoms into the lattice at elevated temperatures[10] or even the growth of new layers or etching into the surface in the vicinity of nanoparticles.[11] On the clean surface, it is known that the $(\sqrt{2} \times \sqrt{2})$R45° reconstruction present at room temperature is reversibly lifted at temperatures around 720 K[12] An earlier study identified the origin of the lifting process as an order-disorder phase transition based on low-energy electron diffraction experiments.[12] The continuous transition was observed to be second-order Ising-like with a gradual loss of long-range order but persisting short-range order above the transition temperature. The structural interpretation of this transition, however, was based

on a previously proposed model of a bulk-truncated magnetite surface,[13] and no quantitative structural analysis was performed.

In this study, we investigate the crystallographic and electronic structure of the magnetite (001) surface at elevated temperatures by a combination of surface x-ray diffraction (SXRD), fast in-situ scanning tunneling microscopy (STM), x-ray and ultraviolet photoemission spectroscopy (XPS, UPS) and low-energy ion scattering (LEIS). We followed the transition from a long-range ordered $(\sqrt{2} \times \sqrt{2})$R45° reconstructed surface at room temperature to a (1×1) surface at elevated temperatures. We interpret our results in view of the subsurface cation vacancy reconstruction (SCV) structural model for this surface,[8] and provide a quantitative analysis of the surface structure at elevated temperatures above the phase transition temperature.

Experimental Details

The surface of magnetite single crystals was cut and mechanically polished to exhibit the (001) surface with a miscut below 0.2°. Three different crystals were used for the SXRD, STM and XPS, LEIS and UPS experiments, respectively. Note that the exact phase transition temperature varies slightly between crystals, as reported previously.[12] In each experiment, the crystal was cleaned in ultra-high vacuum with a base pressure of 10^{-10} mbar by multiple cycles of sputtering with 1 keV Ar-ions for 15 minutes and subsequent annealing. For the SXRD experiments, the annealing temperature of 920 K was held for 15 minutes, with the last annealing step performed in $5 \cdot 10^{-6}$ mbar of oxygen; for the scanning tunneling microscopy (STM) experiments, 20 minutes annealing at 983 K was chosen, with the last annealing step in oxygen of $1 \cdot 10^{-6}$ mbar. This resulted in a contamination-free, $(\sqrt{2} \times \sqrt{2})$R45° reconstructed surface.

We carried out surface x-ray diffraction (SXRD) experiments at the ID03 beamline of the ESRF[14] at a photon energy of 14 keV using a 2D detector in stationary mode[15] at grazing

incidence. The momentum transfer is given in relative reciprocal lattice coordinates (H,K,L) in units of $\frac{2\pi}{a}$ with a magnetite lattice constant of $a = 8.394$ Å. A set of crystal truncation rod data was taken from the clean surface. The sample was subsequently heated in several steps, and the surface structure was probed in each step by scanning through the (2,1) superstructure rod at L=1.6 after waiting $\sim$ 15 minutes for the temperature to stabilize. This was done until no further changes were observed at 770 K. This point in reciprocal space was chosen because it lies on a surface rod only arising from the $(\sqrt{2} \times \sqrt{2})$R45° reconstruction, and is therefore only sensitive to this superstructure and not to the bulk-like structure of the subsurface region underneath. At 770 K, another set of crystal truncation rods was measured, and the surface was cooled down using the same steps, again probing the (2,1,1.6) peak at each temperature step. The SXRD data was analyzed using the ANAROD program package.[16]

The STM experiments were performed using a variable temperature (VT) instrument complemented with a FAST electronics module[17,18] which enables the recording of movies at up to 20 frames per second (fps). A low defect density and large, atomically flat terraces were confirmed by STM and long-range order by low-energy electron diffraction (LEED) before commencing experiments. A boron nitride heater in the sample holder was used to heat the sample and a type K thermocouple directly attached to the crystal and internally referenced to the chamber temperature was used to record the temperature. Temperature-dependent LEED measurements confirmed that our temperature reading is calibrated well and the phase transition temperature of this magnetite crystal is around 725 K, in agreement with previous reports[12] (see Supporting Information). In so-called FastSTM measurements, the feedback gain was lowered to only correct for thermal drift but not follow the surface topography. A sinusoidal tip movement in the fast scan direction was employed, resulting in images and movies which exhibit a higher pixel density at the left and right edges. FastSTM data were recorded as a one-dimensional data stream which was subsequently Fourier filtered to remove known frequencies (e.g. from turbomolecular pumps), background leveled by FFT filtering of

the fast and slow scan directions and their overtones, and reconstructed into movies using a specially built Python script. The resulting movies were then further processed and analyzed in ImageJ.[19] The images were corrected for linear and nonlinear distortions based on (1×1) spots in the Fourier transform, similar to the process described in Ref.[20] Thermal drift was corrected for by laterally shifting frames with respect to each other in time. The frames of drift-corrected movies could then be averaged to a noise level that is vastly superior compared to standard (slow) STM images: subtle structural details with little corrugation which are typically drowned by highly diffusive transient species can thus be recovered as long as the time window for averaging is appropriate. The averaged frames could further be Fourier transformed to provide a comparison with reciprocal-space measurements and give a clear indication whether the $(\sqrt{2} \times \sqrt{2})$R45° reconstruction was still observable in the images. When reconstruction spots were absent in this FFT, we also examined the average of the Fourier transforms of the individual frames, to ensure that the reconstruction spots are not missing due to rapidly moving domains, which could cause the reconstruction to disappear in the average of the real-space images. Finally, we extracted image lines and rows from the drift-corrected movies and plotted them versus time to investigate contrast changes along and across the Fe rows.

Ultraviolet and X-ray photoelectron spectroscopy (UPS, XPS), low energy ion scattering (LEIS), and LEED experiments were performed in a UHV system described in detail in ref.[21] A SPECS FOCUS 500 monochromatized X-ray source (Al Kα anode) was used for XPS. UPS was performed using a SPECS UVS 10/35 source emitting either He I and He II radiation, and LEIS utilized 1 keV He^+ ions generated by a SPECS IQE 12/38 ion source with a scattering angle of 90°. The same SPECS PHOIBOS 150 energy analyzer was used for all these measurements. The XPS measurements were performed at a grazing emission angle (80° with respect to the surface normal) for maximum surface sensitivity. The LEED measurements were performed using a commercial rear-view LEED optics. The sample used in these experiments was prepared was prepared by Ne^+ sputtering (1 keV) for 10 minutes

followed by annealing at 950 K. Every other annealing step and the last before an experiment was performed in $5 \cdot 10^{-7}$ mbar O_2.

Results and Discussion

SXRD results

In Figure 2, some of the SXRD scans through the (2,1) surface rod only sensitive to the $(\sqrt{2} \times \sqrt{2})$R45° superstructure at different temperatures are shown both during heating up (a) and cooling back down (b) to room temperature. Below 570 K, no changes were visible. Above this temperature, a decrease of the peak intensity of the reconstruction signal is observed. At a temperature of 750 K, the reconstruction peak vanished almost completely, and no further changes could be observed when increasing the temperature to 770 K. When cooling back down, the superstructure signal reappeared. Due to the realignment that was necessary during the heating, the intensities had to be scaled. For this, the background level was used as a reference. Since this level is not absolute and expected to increase due to an increase in thermal diffuse scattering during heating and can also change with the alignment, the absolute intensities cannot be compared directly. The differences stemming from this, however, are rather small and do not fully explain the observed increase in intensity on the superstructure signal during cooling down compared to that during heating up at the same temperature. This is most likely related to desorption of adsorbates during the time the sample was kept at elevated temperatures and slight re-annealing after cooling back down. Next we will discuss the full width at half maximum (FWHM) values extracted from these scans, which can then easily be converted into the lateral correlation length of the surface (Figure 3). In both the crystal used for the present SXRD experiments and in the previous experiments mentioned above,[12] the onset temperature of the lifting process is around 720 K, and the lateral correlation length is gradually decreasing up to a temperature of 770 K, where the intensity becomes too low to determine the FWHM. Overall, these measurements

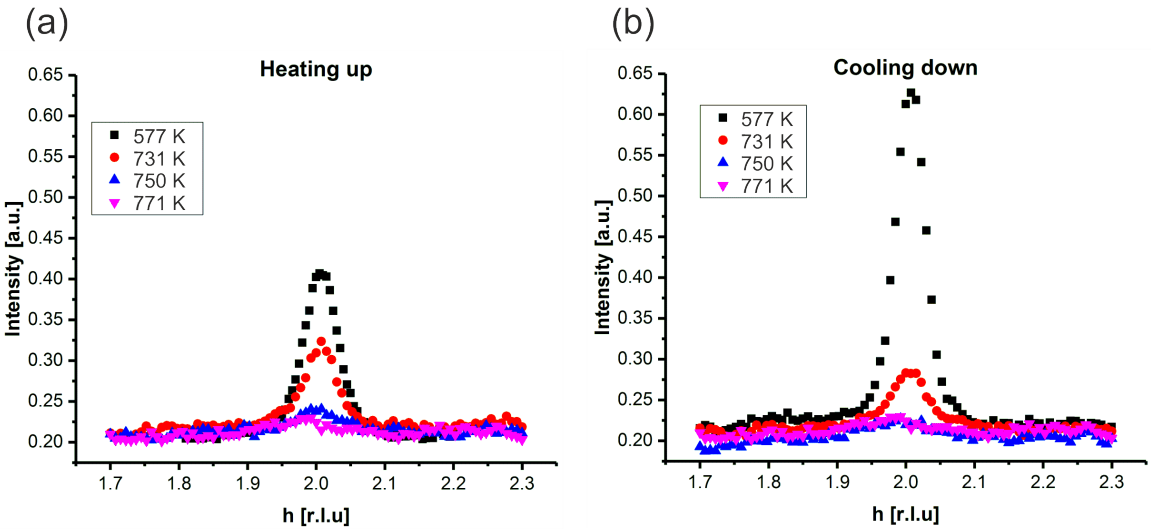

Figure 2: Scans through the (2,1) surface rod in reciprocal H-direction at L=1.6 during (a) heating up and (b) cooling down.

agree very well with the order-disorder phase transition that was found for this surface in an earlier study,[12] as does the temperature range in which the transition occurs.

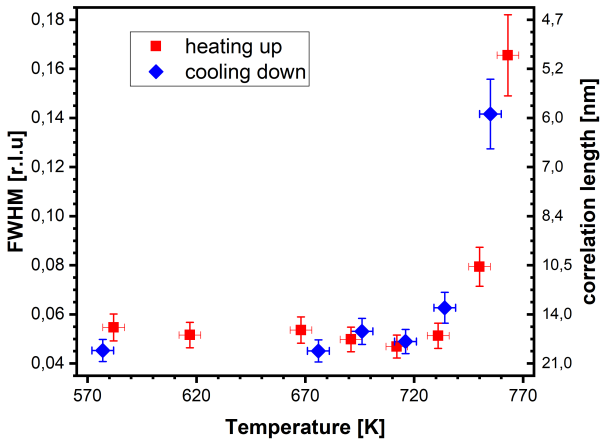

Figure 3: FWHM-values of line scans through the (2,1)-reconstruction rod at L=1.6 taken at different temperatures during heating up (red) and cooling down (blue). Also shown are the corresponding lateral correlation lengths.

To analyze the surface structure in more detail, crystal truncation rods were measured at room temperature and at 770 K, shown in Figure 4. They demonstrate that the phase transition is not simply a lifting of the reconstruction. The crystal truncation rods at room temperature fit very well to those of the reconstructed surface.[9] But although the super-

structure signal from the reconstruction vanishes at 770 K, the crystal truncation rods at this temperature are fairly similar to those of the reconstructed surface, and show a huge difference to those expected from a bulk-truncated surface[22] (also shown in Figure 4). This allows us to hypothesize, that locally the structure of the reconstruction is still partially intact, i.e., the layer occupations (additional Fe in the first tetrahedral layer, missing Fe in the subsurface octahedral layer) do not substantially change, although the long-range $(\sqrt{2} \times \sqrt{2})$R45° order is lost. The absence of the superstructure order does not influence the signal on the crystal truncation rods since they are only sensitive to the smaller periodicity of the bulk crystal lattice and not to the larger one of the superstructure.

To get more insights into the structural arrangement of the Fe cations, different models were fitted to the SXRD data, and the reduced χ^2, also called goodness-of-fit, was used to check and compare the level of agreement between fit and data. As expected, a bulk-truncated surface shows a bad agreement with the data ($\chi^2_{red} = 5.66$). A reconstructed surface shows a better, but still suboptimal agreement ($\chi^2_{red} = 3.88$). To improve the agreement, the possibility that not all lattice sites were fully occupied or unoccupied had to be taken into account. This possibility was included in the models by introducing occupation parameters for several iron lattice positions. In the first double layer, occupation parameters were introduced for the tetrahedral iron positions that are normally fully occupied in both the bulk truncated and the reconstructed surface (Fe_{tet}), for the additional tetrahedral site that is occupied in the reconstructed surface but unoccupied in the bulk-truncated structure ($Fe_{tet,int}$) and for the tetrahedral site that is equivalent to this one under bulk symmetry, but usually not occupied in either structure ($Fe_{tet,add}$). In the second double layer, occupation parameters were introduced for the octahedral lattice sites that are vacant in the reconstructed surface but occupied in the bulk-truncated structure ($Fe_{oct,vac}$; orange in Figure 1(b)), and the octahedral lattice sites that are occupied in both structures ($Fe_{(oct)}$). Occupation parameters for adjacent sites were tested, but not found to have any significant impact on the fits and therefore omitted in the final fitting. In addition, the positions of all iron

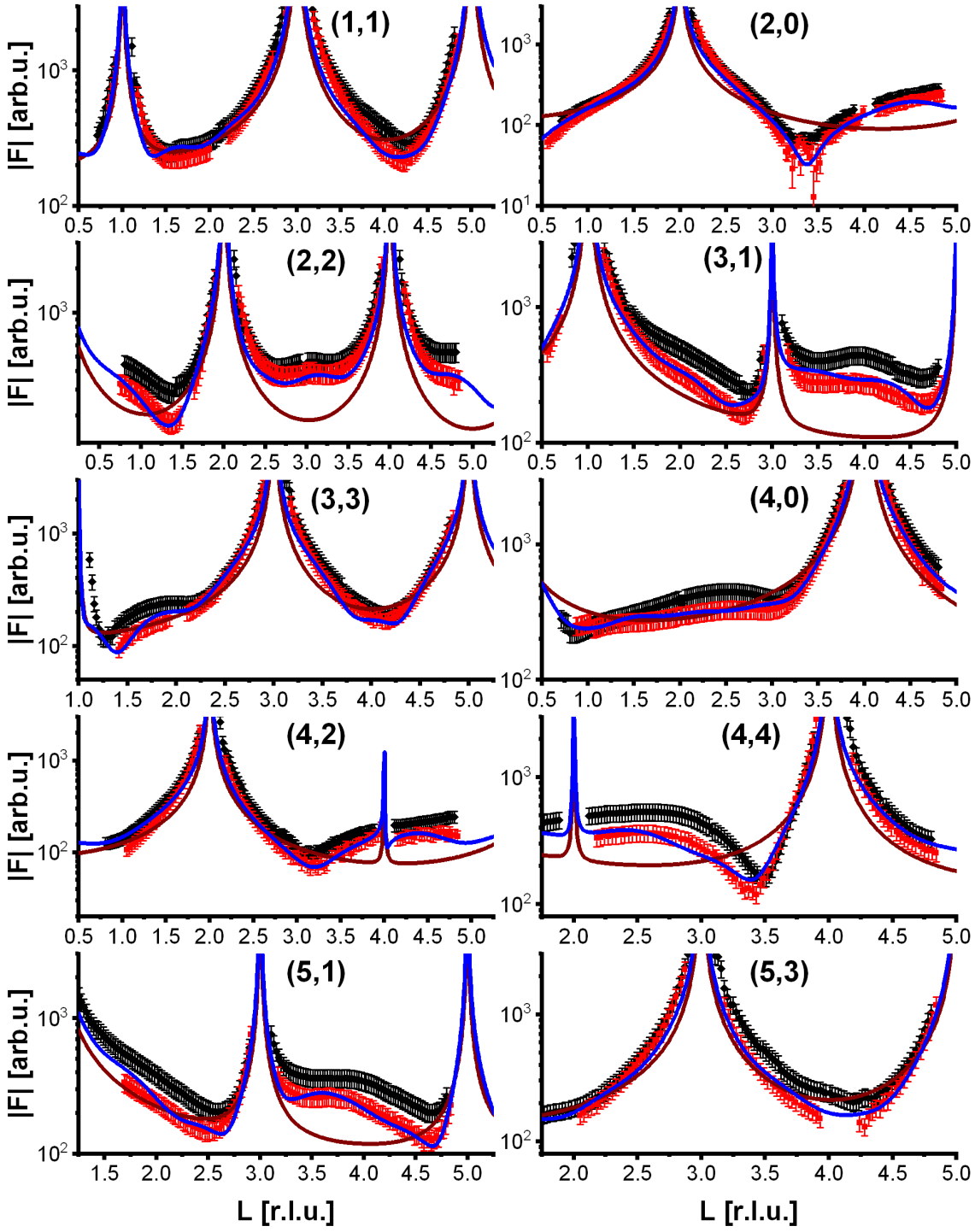

Figure 4: Crystal truncation rods of the clean magnetite (001) surface at room temperature (black squares) and at 770 K (red squares). Also shown are the structure factors of a bulk-truncated surface (brown) and of the best fit to the data at 770 K (blue).

and, in a second step, also all oxygen atoms in the first unit cell were fitted, only allowing distortions according to the symmetry of the $(\sqrt{2} \times \sqrt{2})R45°$ reconstruction. An overview of these results is shown in Table 1.

Table 1: Overview over the results from the structural refinement for the high-temperature phase (773 K, above the phase transition). In model 1, only the occupation parameters were fitted, while model 2 also includes parameters for the iron positions, and in model 3, also the oxygen positions were refined.

Model	χ^2_{red}	Positions		Occupancies				
		Fe	O	$Fe_{(tet)}$	$Fe_{tet,int}$	$Fe_{tet,add}$	$Fe_{(oct)}$	$Fe_{oct,vac}$
1	2.78	-	-	0.90	0.45	0.34	0.70	0.85
2	0.73	+	-	0.86	0.62	0.05	0.80	0.58
3	0.73	+	+	0.86	0.62	0.05	0.80	0.58

These fits show that, at elevated temperatures, the additional tetrahedral iron position becomes partially depleted, and the octahedral vacant sites underneath are partially filled, in good agreement with the STM data which we will discuss below. This is accompanied by a partial depletion of the regular tetrahedral lattice sites in the first double layer and the octahedral sites in the second one that are occupied in both the bulk-truncated and the reconstructed surface, and slight distortions of the lattice of up to 0.1 Å in the first layer and 0.06 Å in the second layer. This change in site occupations rules out a loss of long-range order simply due to an increase in thermal vibrations, especially since the Debye-Waller-factor values of the surface atoms did not increase significantly when included in the fitting. Together with the fact that the local structure seems rather unchanged, this observation points towards a statistical reorganization by diffusion at the surface mainly of the additional tetrahedral iron atoms through the octahedral vacant sites underneath as the source for the lifting of the reconstruction. The reorganization leads to a fluctuating occupation of lattice sites, lattice distortions and an increase in the concentration of defects at the surface like anti-phase domain boundaries and interstitial subsurface cations.[23,24]

At high temperature, the occupation of the sites deviates too much from that of the ideal

SCV reconstruction, thus the long-range order is lost. Nevertheless, the site occupations are not too far from that of the SCV model, in line with the reported surface diagram from theoretical calculations[8] which shows that the reconstruction should indeed be stable under an oxygen chemical potential of -1.71 eV corresponding to UHV conditions at 770 K. In addition, regular lattice sites are also found to be involved in the near surface diffusion process.

FastSTM results

Having determined from SXRD the average atomic surface structure, the question arises how the structure evolves locally in real space and whether the change in occupations is static or dynamic. Looking at FastSTM movies at and around the phase transition, several structural features can still be resolved. While standard STM images (in particular in constant-current mode) are dominated by streaks from fast moving species, averaging many consecutive FastSTM frames preserves atomic resolution. Figure 5 shows the average of several hundred frames each at the onset of the phase transition at 701 K (a), right in the middle at 745 K (b), and beyond at 784 K(c) (cf. Supporting Information for a temperature calibration by LEED). At the onset, the $(\sqrt{2} \times \sqrt{2})$R45° reconstruction can still be clearly observed with atomic resolution.[8] An FFT of the average frame at this temperature confirms that the reconstruction spots are fairly sharp and clearly visible (circled in red). Furthermore, by marking the same location in each unit cell with a yellow dot, we can unambiguously assign domains on the surface. The domain boundaries between them are increasingly mobile at elevated temperatures. FastSTM Supporting Movie S1 shows that at this temperature, the domain boundaries move rapidly back and forth around an average location but do not move extended distances across the surface. As a result, they appear as smeared-out bright regions that zigzag across the surface in the average frame. One example is marked in the average frame by yellow dashed lines, as a guide to the eye. Comparing the average domain size in Figure 5 (a) with the correlation length from SXRD (Figure 3), we find

good agreement: The FastSTM movie reveals typical domain sizes in the range from 5 to 25 nm. In the middle of the phase transition (745 K), such structures were more difficult to distinguish, as can be seen in 5 (b). A smaller surface area was scanned here which is entirely covered in a single domain, as indicated by the overlaid yellow dots. Perhaps surprisingly, even though the reconstruction spots lost more than half of their intensity in LEED at this temperature (see Figure S1), they are still clearly visible in the FFT of the averaged frame. Finally, at a temperature just beyond the phase transition, the FFT of drift-corrected and averaged frames does not show any $(\sqrt{2} \times \sqrt{2})$R45° reconstruction spots anymore and there is also no sign of the reconstruction in the real-space images (see Figure 5 (c)). The STM data are thus consistent with the picture that a long-range SCV reconstruction is no longer present at this temperature.

Looking at the FastSTM movies, it is clear that the surface is anything but static at such elevated temperatures. At the onset of the phase transition, in Supporting Movie S1, defects and domain boundaries are mobile but their dynamics can still be resolved reasonably well. One obvious type of defect appears as bright squares spanning two adjacent Fe_{oct} rows. Just 44 K higher, in Supporting Movie S2, the dynamics resemble more closely fluctuations in apparent brightness than discrete hops. However, a more detailed analysis of the movie reveals that mobile species are similar as at 701 K. To better understand which features might be the mobile ones, it is useful to look at temporal changes in a single line or row of a FastSTM movie. Although not immediately obvious in the movie, we thus find that the same type of bright squares spanning two adjacent Fe rows is still present at 745 K, as shown by the x-t scan ("kymograph") in Figure 5 (d), in which it often appears that two adjacent rows appear bright at the same time (marked in yellow to guide the eye). In addition, we observe many fluctuation-like local changes of the apparent height without a correlation between neighboring rows, which we attribute to a change in local electron density. An increase in brightness on an Fe row typically results from a local surplus of Fe in the surface or subsurface: one example thereof are antiphase domain boundaries, which are Fe rich, and

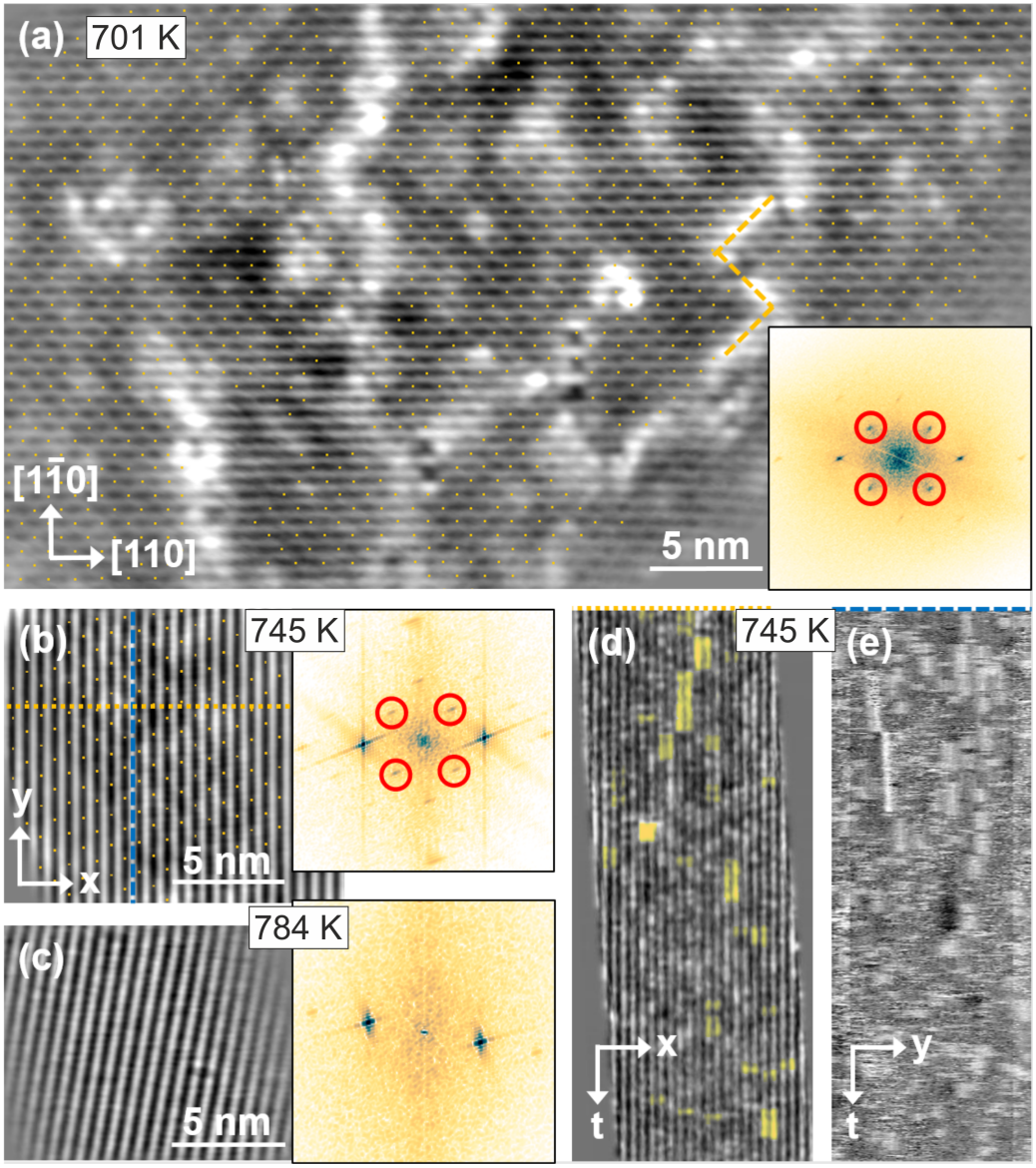

Figure 5: FastSTM data of $Fe_3O_4(001)$. Average of movie frames (a) at the onset of the phase transition (701 K, $V_b = 1.5$ V, $I_t = 0.9$ nA, 4 fps, 520 frames), (b) in the middle of the phase transition (745 K, $V_b = 1.3$ V, $I_t = 1.0$ nA, 11.7 fps, 706 frames), and (c) beyond the phase transition (784 K, $V_b = 1.5$ V, $I_t = 1.0$ nA, 11.7 fps, 818 frames). Full movies see Supporting Movies S1-S3. In (a), the periodicity of the $(\sqrt{2} \times \sqrt{2})$R45° reconstruction is indicated by yellow dots. Dashed yellow lines indicate an example of a domain boundary, i.e. where the dots do not align. In (b), a single domain is visible (yellow dots), while in (c) the reconstruction is no longer apparent. The insets show the FFT of the respective averaged frames, clearly indicating reconstruction spots in (a) and (b) (circled in red), while they are no longer present in (c). (d) and (e) show a line in the x- and y-directions of the movie at 745 K vs. time, cut at the locations marked by the yellow dotted and blue dashed lines in (b), respectively. The time axis spans 60 s. Some example features which extend across two Fe rows are highlighted in yellow in (d).

which appear bright in STM. In an antiphase domain boundary, four Fe atoms can align in the subsurface where domain boundaries occur, resulting in elongated bright features which are arranged diagonally with respect to the surface octahedral Fe rows (see Figure 5 (a)).[24] Unreconstructed unit cells are a different type of local defects, where an additional Fe atom in an octahedral site in the third layer causes the Fe atom in the tetrahedral site in the second layer to move into another octahedral site,[22] thus resulting in six Fe atoms in a row which appear as two elongated bright features on neighboring Fe rows.[24] Additionally, cation interstitials in octahedral sites in the subsurface appear as bright spots on an Fe row which has been shown recently for Ni interstitials.[25] By comparing these known defects with the signatures obtained in the time evolution of a horizontal slice across the Fe rows (5 (d)), the bright features extending across two Fe rows most likely indicate that unreconstructed unit cells are present on the surface. In addition, many bright species which do not extend across two rows are also visible which could be due to the presence of impurity cations.

Looking instead at the time evolution of the brightness along a row, shown in Figure 5 (e), it becomes clear that the residence times of bright features (both those in a single row and those spanning two rows) vary between one and many frames. Since the entire movie spans a time of 60 s, this corresponds to residence times between 0.08 and 8 s. In addition to the bright features, we occasionally observe dark (vacancy-like) features usually spanning two adjacent Fe_{oct} rows, one of them appearing as a dark line in Figure 5 (e); the rows adjacent to them appear brighter (see Supporting Information Figure S2). For the STM movie taken above the phase transition (784 K), a kymograph similar to Fig. 5 (d) shows only horizontal streaks (not shown), indicating that most of the bright features remain stationary for a very short time (less than the interval between the frames, 0.1 seconds). Nevertheless, when viewing the movie (see Supporting Movie S3), one can see several isolated bright species diffusing at the surface. The bright features spanning two adjacent Fe_{oct} rows are very rare, possibly only a random arrangement of isolated species. The only features remaining stationary for a somewhat longer times (up to 3 s) are the vacancy-like dark spots

spanning two adjacent rows, mentioned earlier.

XPS and LEIS results

From the SXRD data analysis, we obtain an Fe enrichment of ~ 10 % in the topmost layers. This would by necessity lead to an appearance of more reduced Fe cations. Figure 6 (a) and (b) show grazing-emission XPS data for the Fe 2p and O 1s regions, respectively. The shoulder at 708.5 eV due to Fe^{2+} increases over the transition, consistent with the reduction of Fe at the surface. The O 1s peak does not change visibly over the same temperature range. A similar conclusion can be drawn from UPS experiments shown in 6 (c), where the increase in the Fe^{2+}-related states at approximately 1 eV occurs at the same time as a decrease in the intensity of the Fe^{3+}-related states at 3 eV. The LEIS data shown in 6 (d) reveals that the peaks from Fe and O change in relative intensity over the transition. The increase in the Fe signal is consistent with the interpretation that the (1×1) surface is enriched in Fe. In reference LEED experiments, shown in Figure S3, we confirmed that the lifting of the reconstruction occurs in the same temperature range on this sample as for the crystals used in the SXRD and STM experiments.

Conclusions

We investigated the temperature-dependent, reversible lifting of the $(\sqrt{2} \times \sqrt{2})$R45° reconstruction of the magnetite (001) surface in a multimodal approach. As reported in an earlier study,[12] we find that the onset temperature of the lifting process lies around 720 K, and the reconstruction is lifted gradually. At a temperature of 770 K, it was found to be almost completely lifted, and no further changes were observed in SXRD. This fits well to the postulated second-order phase transition. At the same time, FastSTM shows that Fe cations are highly dynamic at elevated temperatures. While the superstructure is still present, our data at 745 K provide evidence for isolated sites where the reconstruction is lifted and the otherwise

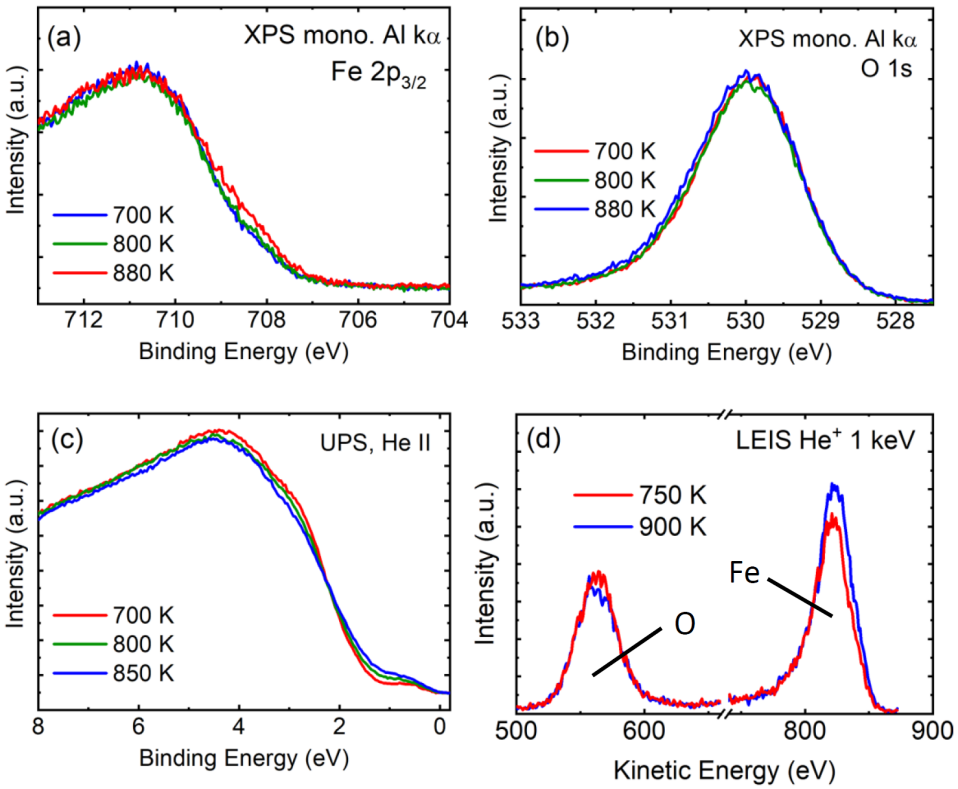

Figure 6: (a) Fe $2p_{3/2}$ and (b) O 1s measured at 700 K (blue), 800 K (green), and 880 K (red). These data are normalized to the peak maximum, and were measured by monochromatized Al K_α radiation. The shoulder at 708.5 eV in the Fe^{2+}-related signal increases above the transition temperature while no change in the O 1s signal is observed. (c) UPS spectra measured using the He II line at 700 K (blue), 800 K (green), and 850 K (red) show an increase in the Fe^{2+}-related states at approximately 1 eV and a decrease in the intensity of the Fe^{3+}-related states at 3 eV with increasing temperature. (d) LEIS measured at 750 K (blue) and 900 K (red) show a change in relative intensity of the O and Fe signals (indicated in the graph). The data were acquired using 1 keV He^+.

empty Fe sites of the subsurface Fe_{oct} layer are filled. Further on, we performed a quantitative structural SXRD analysis of the surface above the phase transition, and found that the site occupations are between that of the SCV reconstruction and the bulk-truncated surface, but still closer to those of the SCV structure, although the long-range $(\sqrt{2} \times \sqrt{2})R45°$ order is lost. The surface is more Fe rich than the perfect (long-range-ordered) SCV-reconstruction. This is in agreement with LEIS as well as XPS and UPS, which indicate a small amount of Fe^{2+} at the surface. Finally, we could resolve the local structure atomically with FastSTM and confirmed the presence of the reconstructed surface just below and in the middle of the phase transition.

Acknowledgement

This work was funded by the Deutsche Forschungsgemeinschaft (DFG, German Research Foundation) Projektnummer 192346071 SFB 986 for the SXRD work and ES 349/1-2 and HE 3454/18-2 for the STM work. FastSTM was developed with funds from the EU-H2020 Research and Innovation Programme under grant agreement no. 654360 NFFA-Europe. B.A.J.L. gratefully acknowledges a Marie Skłodowska-Curie Individual Fellowship under grant ClusterDynamics (no. 703972) from the European Union Horizon 2020 research and innovation program and financial support from the Young Academy of the Bavarian Academy of Sciences and Humanities. The authors at TUM acknowledge Sebastian Kaiser and Ke Zhang for help with the LEED measurements. JH and GSP acknowledge funding from the Austrian Science Fund (FWF) START prize Y847-N20. We acknowledge excellent support by the ID03 beamline staff during our SXRD experiment at the ESRF.

Supporting Information Available

A listing of the contents of each file supplied as Supporting Information should be included. For instructions on what should be included in the Supporting Information as well as how

to prepare this material for publications, refer to the journal's Instructions for Authors.

The following files are available free of charge.

- SIArndt.pdf: supporting information concerning temperature calibration and FastSTM movies
- MovieS1.avi: supporting FastSTM movie T=701 K, 4 fps
- MovieS2.avi: Supporting FastSTM Movie T=745 K, 11.7 fps
- MovieS3.avi Supporting FastSTM Movie T=784 K, 11.7 fps

References

(1) Hua, M.; Zhang, S.; Pan, B.; Zhang, W.; Lv, L.; Zhang, Q. Heavy metal removal from water/wastewater by nanosized metal oxides: A review. *Journal of Hazardous Materials* **2012**, *211-212*, 317–331.

(2) Jain, T. K.; Morales, M. A.; Sahoo, S. K.; Leslie-Pelecky, D. L.; Labhasetwar, V. Iron Oxide Nanoparticles for Sustained Delivery of Anticancer Agents. *Molecular Pharmaceutics* **2005**, *2*, 194–205.

(3) Dilnawaz, F.; Singh, A.; Mohanty, C.; Sahoo, S. K. Dual drug loaded superparamagnetic iron oxide nanoparticles for targeted cancer therapy. *Biomaterials* **2010**, *31*, 3694–3706.

(4) Fu, Z.; Wang, J.; Zhang, N.; An, Y.; Yang, Z. Effect of Cu doping on the catalytic activity of Fe_3O_4 in water-gas shift reactions. *International Journal of Hydrogen Energy* **2015**, *40*, 2193–2198.

(5) Zhu, M.; Wachs, I. E. Iron-Based Catalysts for the High-Temperature Water-Gas Shift (HT-WGS) Reaction: A Review. *ACS Catalysis* **2016**, *6*, 722–732.

(6) Dreyer, A.; Feld, A.; Kornowski, A.; Yilmaz, E. D.; Noei, H.; Meyer, A.; Krekeler, T.; Jiao, C.; Stierle, A.; Abetz, V.; Weller, H.; Schneider, G. A. Organically linked iron oxide nanoparticle supercrystals with exceptional isotropic mechanical properties. *Nature Materials* **2016**, *15*, 522.

(7) Domenèch, B.; Plunkett, A.; Kampferbeck, M.; Blankenburg, M.; Bor, B.; Giuntini, D.; Krekeler, T.; Wagstaffe, M.; Noei, H.; Stierle, A.; Ritter, M.; Mueller, M.; Vossmeyer, T.; Weller, H.; Schneider, G. A. Modulating the mechanical properties of supercrystalline nanocomposite materials via solvent-ligand interactions. *Langmuir*

(8) Bliem, R.; McDermott, E.; Ferstl, P.; Setvin, M.; Gamba, O.; Pavelec, J.; Schneider, M. A.; Schmid, M.; Diebold, U.; Blaha, P.; Hammer, L.; Parkinson, G. S. Subsurface cation vacancy stabilization of the magnetite (001) surface. *Science* **2014**, *346*, 1215–1218.

(9) Arndt, B.; Bliem, R.; Gamba, O.; Van Der Hoeven, J. E. S.; Noei, H.; Diebold, U.; Parkinson, G. S.; Stierle, A. Atomic structure and stability of magnetite Fe_3O_4(001): An X-ray view. *Surface Science* **2016**, *653*, 76–81.

(10) Bliem, R.; Pavelec, J.; Gamba, O.; McDermott, E.; Wang, Z.; Gerhold, S.; Wagner, M.; Osiecki, J.; Schulte, K.; Schmid, M.; Blaha, P.; Diebold, U.; Parkinson, G. S. Adsorption and incorporation of transition metals at the magnetite Fe_3O_4(001) surface. *Physical Review B* **2015**, *92*, 075440.

(11) Bliem, R.; van der Hoeven, J.; Zavodny, A.; Gamba, O.; Pavelec, J.; de Jongh, P. E.; Schmid, M.; Diebold, U.; Parkinson, G. S. An Atomic-Scale View of CO and H_2 Oxidation on a Pt/Fe_3O_4 Model Catalyst. *Angewandte Chemie International Edition* **2015**, *54*, 13999–14002.

(12) Bartelt, N. C.; Nie, S.; Starodub, E.; Bernal-Villamil, I.; Gallego, S.; Vergara, L.;

McCarty, K. F.; de la Figuera, J. Order-disorder phase transition on the (100) surface of magnetite. *Physical Review B* **2013**, *88*, 235436.

(13) Pentcheva, R.; Wendler, F.; Meyerheim, H. L.; Moritz, W.; Jedrecy, N.; Scheffler, M. Jahn-Teller Stabilization of a Polar Metal Oxide Surface: $Fe_3O_4(001)$. *Physical Review Letters* **2005**, *94*, 126101.

(14) Balmes, O.; van Rijn, R.; Wermeille, D.; Resta, A.; Petit, L.; Isern, H.; Dufrane, T.; Felici, R. The ID03 surface diffraction beamline for in-situ and real-time X-ray investigations of catalytic reactions at surfaces. *Catalysis Today* **2009**, *145*, 220–226.

(15) Schlepütz, C. M.; Herger, R.; Willmott, P. R.; Patterson, B. D.; Bunk, O.; Brönnimann, C.; Henrich, B.; Hülsen, G.; Eikenberry, E. F. Improved data acquisition in grazing-incidence X-ray scattering experiments using a pixel detector. *Acta Crystallographica Section A: Foundations of Crystallography* **2005**, *61*, 418–425.

(16) ESRF hompage of the ANA-ROD project. `http://www.esrf.eu/computing/scientific/joint_projects/ANA-ROD`.

(17) Esch, F.; Dri, C.; Spessot, A.; Africh, C.; Cautero, G.; Giuressi, D.; Sergo, R.; Tommasini, R.; Comelli, G. The FAST module: an add-on unit for driving commercial scanning probe microscopes at video rate and beyond. *Review of Scientific Instruments* **2011**, *82*, 053702.

(18) Dri, C.; Panighel, M.; Tiemann, D.; Patera, L. L.; Troiano, G.; Fukamori, Y.; Knoller, F.; Lechner, B. A.; Cautero, G.; Giuressi, D.; Comelli, G.; Fraxedas, J.; Africh, C.; Esch, F. The new FAST module: A portable and transparent add-on module for time-resolved investigations with commercial scanning probe microscopes. *Ultramicroscopy* **2019**, *205*, 49 – 56.

(19) Schneider, C. A.; Rasband, W. S.; Eliceiri, K. W. NIH Image to ImageJ: 25 years of image analysis. *Nature methods* **2012**, *9*, 671.

(20) Choi, J. I. J.; Mayr-Schmälzer, W.; Mittendorfer, F.; Redinger, J.; Diebold, U.; Schmid, M. The growth of ultra-thin zirconia films on $Pd_3Zr(0\,0\,0\,1)$. *Journal of Physics: Condensed Matter* **2014**, *26*, 225003.

(21) Pavelec, J.; Hulva, J.; Halwidl, D.; Bliem, R.; Gamba, O.; Jakub, Z.; Brunbauer, F.; Schmid, M.; Diebold, U.; Parkinson, G. S. A multi-technique study of CO_2 adsorption on Fe_3O_4 magnetite. *The Journal of Chemical Physics* **2017**, *146*, 014701.

(22) Arndt, B.; Sellschopp, K.; Creutzburg, M.; Grånäs, E.; Krausert, K.; Vonk, V.; Müller, S.; Noei, H.; Feldbauer, G.; Stierle, A. Carboxylic acid induced near-surface restructuring of a magnetite surface. *Communications Chemistry* **2019**, *2*, 92.

(23) Parkinson, G. S.; Manz, T. a.; Novotný, Z.; Sprunger, P. T.; Kurtz, R. L.; Schmid, M.; Sholl, D. S.; Diebold, U. Antiphase domain boundaries at the $Fe_3O_4(001)$ surface. *Physical Review B* **2012**, *85*, 195450.

(24) Gamba, O.; Hulva, J.; Pavelec, J.; Bliem, R.; Schmid, M.; Diebold, U.; Parkinson, G. S. The Role of Surface Defects in the Adsorption of Methanol on $Fe_3O_4(001)$. *Topics in Catalysis* **2017**, *60*, 420–430.

(25) Jakub, Z.; Hulva, J.; Mirabella, F.; Kraushofer, F.; Meier, M.; Bliem, R.; Diebold, U.; Parkinson, G. S. Nickel Doping Enhances the Reactivity of $Fe_3O_4(001)$ to Water. *The Journal of Physical Chemistry C* **2019**,

Graphical TOC Entry

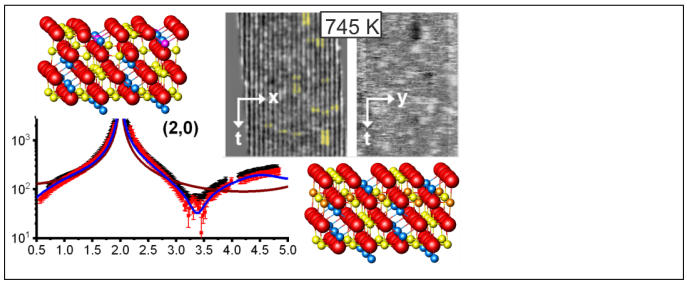

Supporting information for Order-disorder phase transition of the subsurface cation vacancy reconstruction on $Fe_3O_4(001)$

Björn Arndt[a,b], Barbara A. J. Lechner[c,*], Alexander Bourgund[c], Elin Grånäs[a], Marcus Creutzburg[a,b], Konstantin Krausert[a,b], Jan Hulva[d], Gareth S. Parkinson[d], Michael Schmid[d], Vedran Vonk[a], Friedrich Esch[c], Andreas Stierle[a,b,*]

[a] *Deutsches Elektronen-Synchrotron (DESY), D-22607 Hamburg*
[b] *University of Hamburg, Physics Department, D-20355 Hamburg*
[c] *Department of Chemistry & Catalysis Research Center, Technical University of Munich, D-85748 Garching*
[d] *Institute of Applied Physics, TU Wien, A-1040 Vienna*

*Corresponding author.

1. Temperature calibration for FastSTM measurements

In order to ensure that the temperature reading during our FastSTM experiments is comparable to that from the SXRD experiments, we performed temperature-dependent LEED on the sample used for STM measurements. The sample is kept on the same sample holder and the same heater and thermocouple (both included in the holder) are used to control and read the temperature in the two experiments. Figure 1 shows the amplitude of the (1/2, 3/2) diffraction spot of the $(\sqrt{2} \times \sqrt{2})$R45°reconstruction while heating the sample up through the phase transition and cooling back down, measured with an electron energy of 25 eV. To account for the hysteresis behavior in the heating and cooling curves, we take the mean value of the two curves at the point where the intensity drop is half of its maximum. This approach is justified since the sample is equilibrated at one temperature for a significantly longer time in the STM than during the LEED measurement. We obtain a transition temperature of 725±20 K, in excellent agreement with Ref. [1].

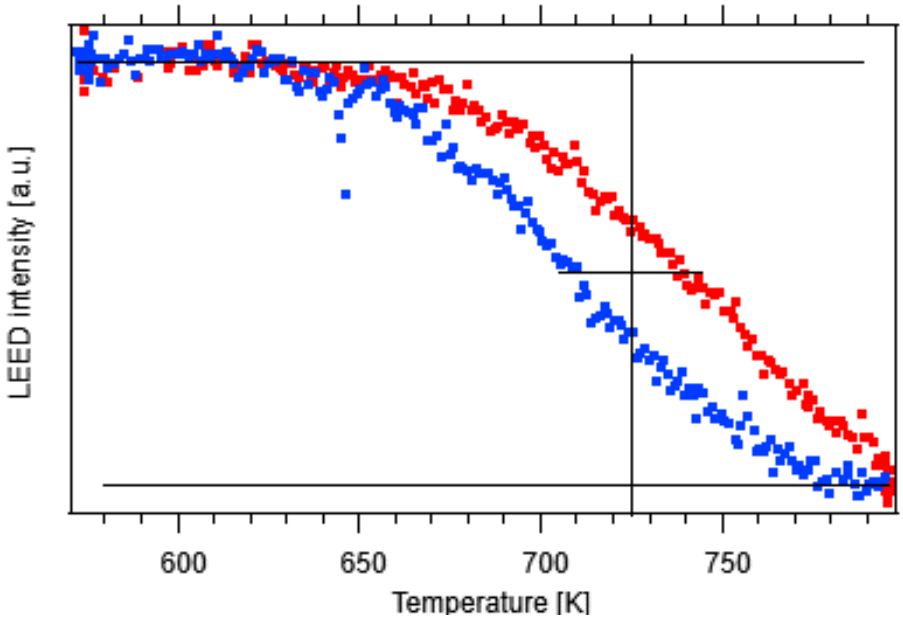

Figure 1: Intensity of the $(\sqrt{2} \times \sqrt{2})$R45°(1/2, 3/2) LEED spot while heating (red) and cooling (blue) the sample through the phase transition. The horizontal lines mark the minimum and maximum intensity levels and the cross is used to identify the transition temperature as the mean value of the heating and cooling curves where the intensity has dropped by half of the total drop.

2. Surface dynamics in FastSTM movies

Three supporting movies are available which were recorded with the following settings:
Supporting Movie S1: 701 K, $V_b = 1.5$ V, $I_t = 0.9$ nA, 4 fps.
Supporting Movie S2: 745 K, $V_b = 1.3$ V, $I_t = 1.0$ nA, 11.7 fps.
Supporting Movie S3: 784 K, $V_b = 1.5$ V, $I_t = 1.0$ nA, 11.7 fps.

For better visualization, Movie S1 has been accelerated by a factor of 7.5 and Movie S2 has been slightly filtered to remove streaks and every other frame has been omitted to avoid slight vertical phase shifts between upward and downward measurements. In line with the rearrangement of the iron atoms, we have further information for possible vertical mass transport in the measurements obtained at 784 K: In rare events, we see the formation of depressions extending across two iron rows with a well-defined rim that disappear after some frames and occasionally reappear at the same position. The frequency of occurrence of these depressions depends on the sample preparation. When cooling down the sample to room temperature, some of these defects can still be observed as static features. In view of the magnetite lattice dynamics governed by Fe transport and not by O transport [2], we assign these depressions either to Fe transport processes or to contaminants in the cation lattice that occasionally reach the surface on their diffusion path.

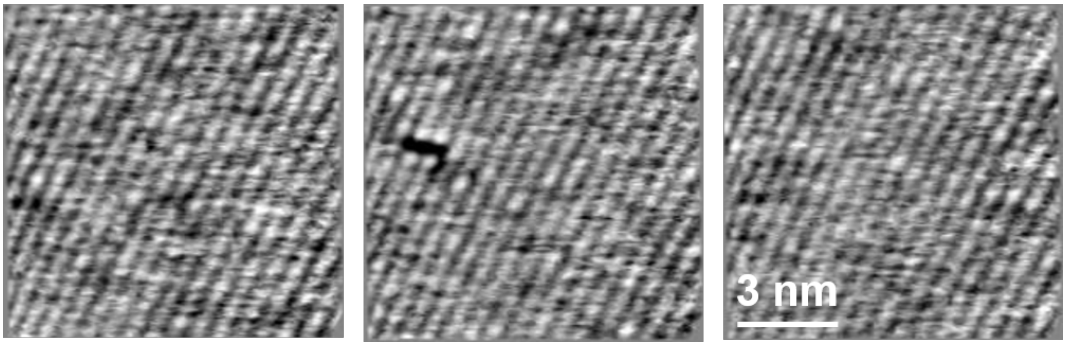

Figure 2: Frames from a FastSTM movie at 784 K which are separated in time by approx. 0.3 s show that a depression appears in a location where previously the pristine surface was visible, and disappears again.

3. Temperature calibration for XPS, UPS and LEIS measurements

On the crystal used for XPS, UPS and LEIS, the phase transition was also investigated by low energy electron diffraction (LEED), as shown in Fig. 3. We could thus confirm that the phase transition occurs in a similar temperature range in this crystal as in the ones used for SXRD and STM experiments, respectively.

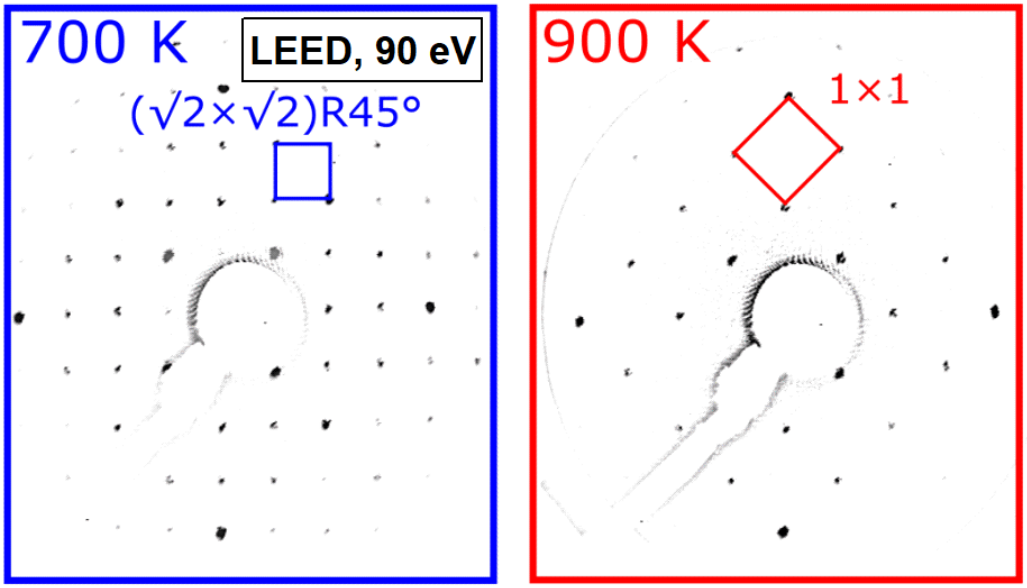

Figure 3: LEED pattern below (700 K) and above the phase transition (900 K)

[1] N. C. Bartelt, S. Nie, E. Starodub, I. Bernal-Villamil, S. Gallego, L. Vergara, K. F. McCarty, J. de la Figuera, Order-disorder phase transition on the (100) surface of magnetite, Physical Review B 88 (23) (2013) 235436. doi:10.1103/PhysRevB.88.235436.
URL http://link.aps.org/doi/10.1103/PhysRevB.88.235436
[2] G. S. Parkinson, Iron oxide surfaces, Surface Science Reports 71 (1) (2016) 272–365.

6.3 List of Publications

- Lechner, B. A. J.; Knoller, F.; Bourgund, A.; Heiz, U.; Esch, F. A Microscopy Approach to Investigating the Energetics of Small Supported Metal Clusters, *J. Phys. Chem. C* **2018**, *122*, 22569–22576.

- Bourgund, A.; Lechner, B. A. J.; Meier, M.; Franchini, C.; Parkinson, G. S.; Heiz, U.; Esch, F. Influence of Local Defects on the Dynamics of O–H Bond Breaking and Formation on a Magnetite Surface, *J. Phys. Chem. C* **2019**, *123*, 19742–19747.

- Arndt, B.; Lechner, B. A. J.; Bourgund, A.; Grånäs, E.; Creutzburg, M; Krausert, K.; Hulva, J.; Parkinson, G. S.; Schmid, M.; Vonk, V.; Esch, F.; Stierle, A. *submitted*.

Bibliography

(1) Döbereiner, J. W., *Die neuesten und wichtigsten physikalisch-chemischen Entdeckungen: über neu entdeckte höchst merkwürdige Eigenschaften des Platins und die pneumatisch-capillare Thätigkeit gesprungener Gläser*; August Schmid: Jena, 1823.

(2) Houdry, E. J. Catalytic Structure and Composition. pat., US2742437, 1952.

(3) Li, H.; Bhadury, P. S.; Riisager, A.; Yang, S. *Catal. Sci. Technol.* **2014**, *4*, 4138–4168.

(4) W. Vielstich, A. Lamm, H. G., *Handbook of Fuel Cells*, 2003.

(5) Bosch, C.; Wild, W. Hydrogen Production., 1914.

(6) Haber, F.; van Oordt, G. *Zeitschrift für Anorg. Chemie* **1905**, *44*, 341–378.

(7) Mittasch, A.; Pier, M.; Mueller, C. Verfahren zur Herstellung von Methylalkohol und anderen sauerstoffhaltigen organischen Verbindungen. pat., DE544665C, 1932.

(8) Nobel Media AB The Nobel Prize in Chemistry 2007., 2019.

(9) Scipioni, A.; Manzardo, A.; Ren, J., *Hydrogen Economy*; Academic Press: London, San Diego, Cambridge, Oxford, 2017.

(10) German Federal Ministry of Education and Research Nationale Wasserstoffstrategie., 2019.

(11) German Federal Ministry for Economic Affairs and Energy Wasserstoff und Energiewende., 2019.

(12) Bartholomew, C. H. *Appl. Catal. A Gen.* **2001**, *212*, 17–60.

(13) Fukamori, Y.; König, M.; Yoon, B.; Wang, B.; Esch, F.; Heiz, U.; Landman, U. *ChemCatChem* **2013**, *5*, 3330–3341.

(14) Wang, B.; König, M.; Bromley, C. J.; Yoon, B.; Treanor, M. J.; Garrido Torres, J. A.; Caffio, M.; Grillo, F.; Früchtl, H.; Richardson, N. V.; Esch, F.; Heiz, U.; Landman, U.; Schaub, R. *J. Phys. Chem. C* **2017**, *121*, 9413–9423.

(15) Karim, W.; Spreafico, C.; Kleibert, A.; Gobrecht, J.; VandeVondele, J.; Ekinci, Y.; van Bokhoven, J. A. *Nature* **2017**, *541*, 68–71.

(16) Walenta, C. A.; Kollmannsberger, S. L.; Courtois, C.; Pereira, R. N.; Stutzmann, M.; Tschurl, M.; Heiz, U. *Phys. Chem. Chem. Phys.* **2019**, *21*, 1491–1496.

(17) Moulijn, J. A.; Makkee, M.; van Diepen, A. E., *Chemical Process Technology*, 2nd editio; John Wiley & Sons, Ltd: West Sussex, 2013.

(18) Zhu, M.; Wachs, I. E. *ACS Catal.* **2016**, *6*, 722–732.

(19) Santos-Carballal, D.; Roldan, A.; Grau-Crespo, R.; de Leeuw, N. H. *Phys. Chem. Chem. Phys.* **2014**, *16*, 21082–21097.

(20) Parkinson, G. S. *Surf. Sci. Rep.* **2016**, *71*, 272–365.

(21) Haberland, H.; Kleinermanns, K.; Träger, F. In *Gase, Nanosyst. Flüssigkeiten*; Walter de Gruyter: Berlin, New York, 2005, pp 817–976.

(22) Taylor, K. J.; Pettiette-Hall, C. L.; Cheshnovsky, O.; Smalley, R. E. *J. Chem. Phys.* **1992**, *96*, 3319–3329.

(23) Henry, C. R. In *Nanocatalysis Nanosci. Technol.* Heiz, U., Landman, U., Eds.; Springer, Berlin, Heidelberg: 2007, pp 245–268.

(24) Smalley, R. E.; E., R. *Laser Chem.* **1983**, *2*, 167–184.

(25) Abbet, S.; Sanchez, A.; Heiz, U.; Schneider, W.-D. D.; Ferrari, A. M.; Pacchioni, G.; Rösch, N. *J. Am. Chem. Soc.* **2000**, *122*, 3453–3457.

(26) Kunz, S.; Schweinberger, F. F.; Habibpour, V.; Röttgen, M.; Harding, C.; Arenz, M.; Heiz, U. *J. Phys. Chem. C* **2010**, *114*, 1651–1654.

(27) Haruta, M. *Catal. Today* **1997**, *36*, 153–166.

(28) Valden, M.; Lai, X.; Goodman, D. W. *Science* **1998**, *281*, 1647–1650.

(29) Lopez, N.; Janssens, T. V.; Clausen, B. S.; Xu, Y.; Mavrikakis, M.; Bligaard, T.; Nørskov, J. K. *J. Catal.* **2004**, *223*, 232–235.

(30) Sanchez, A.; Abbet, S.; Heiz, U.; Schneider, W.-D. D.; Häkkinen, H.; Barnett, R. N.; Landman, U. *J. Phys. Chem. A* **1999**, *103*, 9573–9578.

(31) Meusel, I.; Hoffmann, J.; Hartmann, J.; Libuda, J.; Freund, H.-J. *J. Phys. Chem. B* **2001**, *105*, 3567–3576.

(32) Engel, T.; Ertl, G. *J. Chem. Phys.* **1978**, *69*, 1267.

(33) Wörz, A. S.; Judai, K.; Abbet, S.; Heiz, U. *J. Am. Chem. Soc.* **2003**, *125*, 7964–7970.

(34) Bonanni, S.; Aït-Mansour, K.; Brune, H.; Harbich, W. *ACS Catal.* **2011**, *1*, 385–389.

(35) Crampton, A. S.; Rötzer, M. D.; Ridge, C. J.; Schweinberger, F. F.; Heiz, U.; Yoon, B.; Landman, U. *Nat. Commun.* **2016**, *7*, 10389.

(36) Crampton, A. S.; Rötzer, M. D.; Schweinberger, F. F.; Yoon, B.; Landman, U.; Heiz, U. *J. Catal.* **2016**, *333*, 51–58.

(37) Häkkinen, H.; Abbet, S.; Sanchez, A.; Heiz, U.; Landman, U. *Angew. Chem., Int. Ed.* **2003**, *42*, 1297–1300.

(38) Mackay, A. L. *Acta Crystallogr.* **1962**, *15*, 916–918.

(39) Echt, O.; Sattler, K.; Recknagel, E. *Phys. Rev. Lett.* **1981**, *47*, 1121–1124.

(40) Häkkinen, H.; Moseler, M.; Landman, U. *Phys. Rev. Lett.* **2002**, *89*, 033401.

(41) Häkkinen, H.; Yoon, B.; Landman, U.; Li, X.; Zhai, H.-J.; Wang, L.-S. *J. Phys. Chem. A* **2003**, *107*, 6168–6175.

(42) Doye, J. P. K.; Meyer, L. *Phys. Rev. Lett.* **2005**, *95*, 063401.

(43) Xing, X.; Li, X.; Yoon, B.; Landman, U.; Parks, J. H. *Int. J. Mass Spectrom.* **2015**, *377*, 393–402.

(44) Xiao, L.; Wang, L. *J. Phys. Chem. A* **2004**, *108*, 8605–8614.

(45) Eckhard, J. F.; Masubuchi, T.; Tschurl, M.; Barnett, R. N.; Landman, U.; Heiz, U. *J. Phys. Chem. C* **2018**, *122*, 25628–25637.

(46) Yoon, B.; Häkkinen, H.; Landman, U.; Wörz, A. S.; Antonietti, J. M.; Abbet, S.; Judai, K.; Heiz, U. *Science* **2005**, *307*, 403–407.

(47) Harding, C.; Habibpour, V.; Kunz, S.; Farnbacher, A. N.-S.; Heiz, U.; Yoon, B.; Landman, U. *J. Am. Chem. Soc.* **2009**, *131*, 538–548.

(48) Crampton, A. S.; Rötzer, M. D.; Schweinberger, F. F.; Yoon, B.; Landman, U.; Heiz, U. *Angew. Chem., Int. Ed.* **2016**, *55*, 8953–8957.

(49) Crampton, A. S.; Rötzer, M. D.; Landman, U.; Heiz, U. *ACS Catal.* **2017**, *7*, 6738–6744.

(50) Bromann, K.; Felix, C.; Brune, H.; Harbich, W.; Monot, R.; Buttet, J.; Kern, K. *Science* **1996**, *274*, 956–958.

(51) Heiz, U.; Vanolli, F.; Trento, L.; Schneider, W. D. *Rev. Sci. Instrum.* **1997**, *68*, 1986–1994.

(52) Messerli, S.; Schintke, S.; Morgenstern, K.; Sanchez, A.; Heiz, U.; Schneider, W. D. *Surf. Sci.* **2000**, *465*, 331–338.

(53) Wang, B.; Yoon, B.; König, M.; Fukamori, Y.; Esch, F.; Heiz, U.; Landman, U. *Nano Lett.* **2012**, *12*, 5907–5912.

(54) Cheng, H.-P.; Landman, U. *J. Phys. Chem.* **1994**, *98*, 3527–3537.

(55) Chang, J.-R. R.; Chang, S.-L. L.; Lin, T.-B. B. *J. Catal.* **1997**, *169*, 338–346.

(56) Balaj, O. P.; Balteanu, I.; Roßteuscher, T. T. J.; Beyer, M. K.; Bondybey, V. E. *Angew. Chemie* **2004**, *116*, 6681–6684.

(57) Hao, Y; Mihaylov, M; Ivanova, E; Hadjivanov, K; Knozinger, H; Gates, B *J. Catal.* **2009**, *261*, 137–149.

(58) Tauster, S. J.; Fung, S. C.; Garten, R. L. *J. Am. Chem. Soc.* **1978**, *100*, 170–175.

(59) Tauster, S *J. Catal.* **1978**, *55*, 29–35.

(60) Tauster, S. J.; Fung, S. C.; Baker, R. T.; Horsley, J. A. *Science* **1981**, *211*, 1121–1125.

(61) Dulub, O.; Hebenstreit, W.; Diebold, U. *Phys. Rev. Lett.* **2000**, *84*, 3646–3649.

(62) Ertl, G. *Nachrichten aus Chemie, Tech. und Lab.* **1983**, *31*, 178–182.

(63) Kotraba, N. L.; Holley, C. A. Direct reduction process in a rotary hearth furnace. pat., US5186741A, 1993.

(64) Holleman, A. F.; Wiberg, E.; Wiberg, N.; Fischer, G., *Lehrbuch der Anorganische Chemie*, 102nd ed.; Walter de Gruyter: Berlin, New York, 2007.

(65) Wulff, G. *Zeitschrift für Krist. - Cryst. Mater.* **1901**, *34*, 449–530.

(66) Parkinson, G. S.; Novotný, Z.; Jacobson, P.; Schmid, M.; Diebold, U. *Surf. Sci.* **2011**, *605*, L42–L45.

(67) Ryan, P. T. et al. *Phys. Chem. Chem. Phys.* **2018**, *20*, 16469–16476.

(68) Bliem, R.; Van Der Hoeven, J.; Zavodny, A.; Gamba, O.; Pavelec, J.; De Jongh, P. E.; Schmid, M.; Diebold, U.; Parkinson, G. S. *Angew. Chem., Int. Ed.* **2015**, *54*, 13999–14002.

(69) Bliem, R.; van der Hoeven, J. E. S.; Hulva, J.; Pavelec, J.; Gamba, O.; de Jongh, P. E.; Schmid, M.; Blaha, P.; Diebold, U.; Parkinson, G. S. *Proc. Natl. Acad. Sci.* **2016**, *113*, 8921–8926.

(70) Wiesendanger, R.; Shvets, I. V.; Burgler, D.; Tarrach, G.; Guntherodt, H. J.; Coey, J. M. D.; Graser, S. *Science* **1992**, *255*, 583–586.

(71) Seoighe, C.; Naumann, J.; Shvets, I. *Surf. Sci.* **1999**, *440*, 116–124.

(72) Bliem, R.; McDermott, E.; Ferstl, P.; Setvin, M.; Gamba, O.; Pavelec, J.; Schneider, M. A.; Schmid, M.; Diebold, U.; Blaha, P.; Hammer, L.; Parkinson, G. S. *Science* **2014**, *346*, 1215–1218.

(73) Novotný, Z.; Argentero, G.; Wang, Z.; Schmid, M.; Diebold, U.; Parkinson, G. S. *Phys. Rev. Lett.* **2012**, *108*, 216103.

(74) Parkinson, G. S.; Novotny, Z.; Argentero, G.; Schmid, M.; Pavelec, J.; Kosak, R.; Blaha, P.; Diebold, U. *Nat. Mater.* **2013**, *12*, 724–728.

(75) Bliem, R.; Kosak, R.; Perneczky, L.; Novotny, Z.; Gamba, O.; Fobes, D.; Mao, Z.; Schmid, M.; Blaha, P.; Diebold, U.; Parkinson, G. S. *ACS Nano* **2014**, *8*, 7531–7.

(76) Bliem, R.; Pavelec, J.; Gamba, O.; McDermott, E.; Wang, Z.; Gerhold, S.; Wagner, M.; Osiecki, J.; Schulte, K.; Schmid, M.; Blaha, P.; Diebold, U.; Parkinson, G. S. *Phys. Rev. B* **2015**, *92*, 075440.

(77) Jakub, Z.; Hulva, J.; Meier, M.; Bliem, R.; Kraushofer, F.; Setvin, M.; Schmid, M.; Diebold, U.; Franchini, C.; Parkinson, G. S. *Angew. Chemie* **2019**, *131*, 14099–14106.

(78) Gamba, O.; Hulva, J.; Pavelec, J.; Bliem, R.; Schmid, M.; Diebold, U.; Parkinson, G. S. *Top. Catal.* **2017**, *60*, 420–430.

(79) Parkinson, G. S.; Manz, T. A.; Novotný, Z.; Sprunger, P. T.; Kurtz, R. L.; Schmid, M.; Sholl, D. S.; Diebold, U. *Phys. Rev. B* **2012**, *85*, 195450.

(80) Kurahashi, M.; Sun, X.; Yamauchi, Y. *Phys. Rev. B - Condens. Matter Mater. Phys.* **2010**, *81*, 193402.

(81) Parkinson, G. S.; Mulakaluri, N.; Losovyj, Y.; Jacobson, P.; Pentcheva, R.; Diebold, U. *Phys. Rev. B* **2010**, *82*, 125413.

(82) Hiura, S.; Ikeuchi, A.; Shirini, S.; Subagyo, A.; Sueoka, K. *Phys. Rev. B* **2015**, *91*, 205411.

(83) Meier, M.; Hulva, J.; Jakub, Z.; Pavelec, J.; Setvin, M.; Bliem, R.; Schmid, M.; Diebold, U.; Franchini, C.; Parkinson, G. S. *Proc. Natl. Acad. Sci.* **2018**, *115*, E5642–E5650.

(84) Gamba, O.; Noei, H.; Pavelec, J.; Bliem, R.; Schmid, M.; Diebold, U.; Stierle, A.; Parkinson, G. S. *J. Phys. Chem. C* **2015**, *119*, 20459–20465.

(85) Novotny, Z.; Mulakaluri, N.; Edes, Z.; Schmid, M.; Pentcheva, R.; Diebold, U.; Parkinson, G. S. *Phys. Rev. B* **2013**, *87*, 195410.

(86) Parkinson, G. S.; Novotný, Z.; Jacobson, P.; Schmid, M.; Diebold, U. *J. Am. Chem. Soc.* **2011**, *133*, 12650–12655.

(87) Kim, Y. K.; Zhang, Z.; Parkinson, G. S.; Li, S.-C.; Kay, B. D.; Dohnálek, Z. *J. Phys. Chem. C* **2009**, *113*, 20020–20028.

(88) Chen, S.; Si, R.; Taylor, E.; Janzen, J.; Chen, J. *J. Phys. Chem. C* **2012**, *116*, 12969–12976.

(89) Binnig, G.; Rohrer, H. Scanning tunneling microscope., 1979.

(90) Binnig, G.; Rohrer, H.; Gerber, C.; Weibel, E. *Appl. Phys. Lett.* **1982**, *40*, 178–180.

(91) Binnig, G.; Rohrer, H.; Gerber, C.; Weibel, E. *Phys. Rev. Lett.* **1982**, *49*, 57–61.

(92) Binnig, G.; Rohrer, H. *Surf. Sci.* **1983**, *126*, 236–244.

(93) Binnig, G.; Rohrer, H.; Gerber, C.; Weibel, E. *Phys. Rev. Lett.* **1983**, *50*, 120–123.

(94) Binnig, G.; Fuchs, H.; Stoll, E. *Surf. Sci.* **1986**, *169*, L295–L300.

(95) Heinrich, A.; Lutz, C.; Baumann, S.; Rau, I. A Boy And His Atom: The World's Smallest Movie., en-ZZ, Film, 2013.

(96) Becker, R. S.; Golovchenko, J. A.; Hamann, D. R.; Swartzentruber, B. S. *Phys. Rev. Lett.* **1985**, *55*, 2032–2034.

(97) Repp, J.; Meyer, G.; Stojković, S. M.; Gourdon, A.; Joachim, C. *Phys. Rev. Lett.* **2005**, *94*, 026803.

(98) Tersoff, J.; Hamann, D. R. *Phys. Rev. Lett.* **1983**, *50*, 1998–2001.

(99) Wiesendanger, R., *Scanning Probe Microscopy and Spectroscopy*; Cambridge University Press: Cambridge, 1994.

(100) Chen, C. J., *Introduction to Scanning Tunneling Microscopy*; Oxford University Press: New York, Oxford, 2007.

(101) Kolasinski, K. W., *Surface Science*; John Wiley & Sons, Ltd: Chichester, UK, 2012.

(102) Voigtländer, B., *Scanning Probe Microscopy*; NanoScience and Technology; Springer Berlin Heidelberg: Berlin, Heidelberg, 2015.

(103) Fonin, M.; Pentcheva, R.; Dedkov, Y. S.; Sperlich, M.; Vyalikh, D. V.; Scheffler, M.; Rüdiger, U.; Güntherodt, G. *Phys. Rev. B* **2005**, *72*, 104436.

(104) Wintterlin, J.; Trost, J.; Renisch, S.; Schuster, R.; Zambelli, T.; Ertl, G. *Surf. Sci.* **1997**, *394*, 159–169.

(105) Rost, M. J. et al. *Rev. Sci. Instrum.* **2005**, *76*, 053710.

(106) Curtis, R.; Mitsui, T.; Ganz, E. *Rev. Sci. Instrum.* **1997**, *68*, 2790–2796.

(107) Mamin, H. J.; Birk, H.; Wimmer, P.; Rugar, D. *J. Appl. Phys.* **1994**, *75*, 161–168.

(108) Schitter, G.; Rost, M. J. *Mater. Today* **2008**, *11*, 40–48.

(109) Besenbacher, F.; Lægsgaard, E.; Stensgaard, I. *Mater. Today* **2005**, *8*, 26–30.

(110) Junkes, H.; Freund, H.; Gura, L.; Heyde, M.; Marschalik, P.; Yang, Z. In *ICALEPCS2017*, JACOW, Geneva, Switzerland: Barcelona, Spain, 2017, pp 1762–1766.

(111) Esch, F.; Dri, C.; Spessot, A.; Africh, C.; Comelli, G. A method for driving a scanning probe microscope at elevated scan frequencies., 2010.

(112) Esch, F.; Dri, C.; Spessot, A.; Africh, C.; Cautero, G.; Giuressi, D.; Sergo, R.; Tommasini, R.; Comelli, G. *Rev. Sci. Instrum.* **2011**, *82*, 053702.

(113) Dri, C.; Panighel, M.; Tiemann, D.; Patera, L. L.; Troiano, G.; Fukamori, Y.; Knoller, F.; Lechner, B. A.; Cautero, G.; Giuressi, D.; Comelli, G.; Fraxedas, J.; Africh, C.; Esch, F. *Ultramicroscopy* **2019**, *205*, 49–56.

(114) Davisson, C.; Germer, L. H. *Phys. Rev.* **1927**, *30*, 705–740.

(115) Ertl, G.; Küppers, J., *Low energy electrons and surface chemistry*, 2nd ed.; Weinheim, Verl. Chemie: Weinheim i.a., 1985.

(116) Park, R. L.; Houston, J. E.; Schreiner, D. G. *Rev. Sci. Instrum.* **1971**, *42*, 60–65.

(117) Henzler, M. *Appl. Surf. Sci.* **1982**, *11-12*, 450–469.

(118) Ibach, H., *Physics of surfaces and interfaces*, 1st ed.; Springer Berlin Heidelberg: 2006.

(119) Apker, L. R. *Ind. Eng. Chem.* **1948**, *40*, 846–847.

(120) King, D. A. *Surf. Sci.* **1975**, *47*, 384–402.

(121) Filser, J. Implementation of advanced FAST movie processing techniques in the pyfast package., Internship Report, Technical University of Munich, 2017.

(122) Forrest, A. R. *Comput. J.* **1972**, *15*, 71–79.

(123) Shao, L.; Zhou, H. *Graph. Model. Image Process.* **1996**, *58*, 223–232.

(124) Delaunay, B. *Zeitschrift für Krist.* **1933**, *84*, 109–149.

(125) Barber, C. B.; Dobkin, D. P.; Huhdanpaa, H. *ACM Trans. Math. Softw.* **1996**, *22*, 469–483.

(126) Briegel, K. Towards fast and stable Pyfast movie processing., Internship Report, Technical University of Munich, 2019.

(127) Yurov, V. Y.; Klimov, A. N. *Surf. Interface Anal.* **1994**, *22*, 84–88.

(128) Nečas, D.; Klapetek, P. *Open Phys.* **2012**, *10*, 181–188.

(129) Bellard, F. FFmpeg (https://ffmpeg.org).

(130) Hunter, J. D. *Comput. Sci. Eng.* **2007**, *9*, 90–95.

(131) Schneider, C. A.; Rasband, W. S.; Eliceiri, K. W. *Nat. Methods* **2012**, *9*, 671–675.

(132) Thevenaz, P.; Ruttimann, U.; Unser, M. *IEEE Trans. Image Process.* **1998**, *7*, 27–41.

(133) Choi, J. I. J.; Mayr-Schmölzer, W; Mittendorfer, F; Redinger, J; Diebold, U; Schmid, M *J. Phys. Condens. Matter* **2014**, *26*, 225003.

(134) Dri, C.; Esch, F.; Africh, C.; Comelli, G. *Meas. Sci. Technol.* **2012**, *23*, 055402.

(135) Knoller, F. L. Reactivity and dynamics of monodisperse Pd clusters on a periodically wettable boron nitride substrate., PhD Thesis, Technical University of Munich, 2018.

(136) Feulner, P.; Menzel, D. *J. Vac. Sci. Technol.* **1980**, *17*, 662–663.

(137) Gleaves, J. T.; Ebner, J. R.; Kuechler, T. C. *Catal. Rev.* **1988**, *30*, 49–116.

(138) Gleaves, J. T.; Yablonskii, G. S.; Phanawadee, P.; Schuurman, Y. *Appl. Catal. A Gen.* **1997**, *160*, 55–88.

(139) Duriez, C.; Henry, C.; Chapon, C. *Surf. Sci.* **1991**, *253*, 190–204.

(140) Shaikhutdinov, S.; Heemeier, M.; Hoffmann, J.; Meusel, I.; Richter, B.; Bäumer, M.; Kuhlenbeck, H.; Libuda, J.; Freund, H.-J.; Oldman, R.; Jackson, S.; Konvicka, C.; Schmid, M.; Varga, P. *Surf. Sci.* **2002**, *501*, 270–281.

(141) Libuda, J. *Surf. Sci.* **2005**, *587*, 55–68.

(142) Libuda, J.; Freund, H.-J. *Surf. Sci. Rep.* **2005**, *57*, 157–298.

(143) Judai, K.; Abbet, S.; Wörz, A. S.; Röttgen, M. A.; Heiz, U. *Int. J. Mass Spectrom.* **2003**, *229*, 99–106.

(144) Watanabe, Y.; Isomura, N. *J. Vac. Sci. Technol. A Vacuum, Surfaces, Film.* **2009**, *27*, 1153–1158.

(145) Bonanni, S.; Aït-Mansour, K.; Hugentobler, M.; Brune, H.; Harbich, W. *Eur. Phys. J. D* **2011**, *63*, 241–249.

(146) Domont, G. Catalysis on supported transiton metal nanostructures - Development and characterization of a UHV compatible reactor and first measurements., Master Thesis, EPFL, 2014.

(147) Achour, H. Transition metal clusters on h-BN/Rh(111): surface interaction and catalytic activity., PhD Thesis, EPFL, 2016.

(148) Parker Hannifin Corp Series 99 Gas Valve Datasheet., 2019.

(149) B.E.S.T. Fluidsysteme GmbH München Order Confirmation., 2019.

(150) Wolfslau, J. G.; Dube, J. E. Balanced pressure solenoid valve., 1958.

(151) Hargraves, D. E. Solenoid valve., 1978.

(152) Najmolhoda, H. Proportional variable force solenoid control valve., 1991.

(153) Hutchings, P. G.; Dalton, J; Anthony, J. C. Proportional solenoid controlled valve., 1993.

(154) Kaiser, S. A highly sensitive setup for reactivity measurements on size-selected supported clusters., Master's Thesis, Technical University of Munich, 2019.

(155) Widmann, D.; Behm, R. J. *Acc. Chem. Res.* **2014**, *47*, 740–749.

(156) Campbell, C.; Ertl, G.; Kuipers, H.; Segner, J. *Surf. Sci.* **1981**, *107*, 207–219.

(157) Park, Y.; Banholzer, W.; Masel, R. *Surf. Sci.* **1985**, *155*, 341–365.

(158) Yoshinobu, J.; Kawai, M. *J. Chem. Phys.* **1995**, *103*, 3220–3229.

(159) Gland, J. L.; Kollin, E. B. *J. Chem. Phys.* **1983**, *78*, 963–974.

(160) Walenta, C. A.; Kollmannsberger, S. L.; Courtois, C.; Tschurl, M.; Heiz, U. *Phys. Chem. Chem. Phys.* **2018**, *20*, 7105–7111.

(161) Kollmannsberger, S. L.; Walenta, C. A.; Courtois, C.; Tschurl, M.; Heiz, U. *ACS Catal.* **2018**, *8*, 11076–11084.

(162) Dulub, O.; Hebenstreit, W.; Diebold, U. *Phys. Rev. Lett.* **2000**, *84*, 3646–3649.

(163) Bourgund, A.; Lechner, B. A. J.; Meier, M.; Franchini, C.; Parkinson, G. S.; Heiz, U.; Esch, F. *J. Phys. Chem. C* **2019**, *123*, 19742–19747.

(164) Struges, H. *J. Am. Stat. Assoc.* **1926**, *21*, 65–66.

(165) Scott, D. W. *Biometrika* **1979**, *66*, 605–610.

(166) Shimazaki, H.; Shinomoto, S. *Neural Comput.* **2007**, *19*, 1503–1527.

(167) Rudemo, M. *Scand. J. Stat.* **1982**, *9*, 65–78.

(168) Winzor, D. J.; Jackson, C. M. *J. Mol. Recognit.* **2006**, *19*, 389–407.

(169) Ditze, S.; Stark, M.; Buchner, F.; Aichert, A.; Jux, N.; Luckas, N.; Görling, A.; Hieringer, W.; Hornegger, J.; Steinrück, H.-P.; Marbach, H. *J. Am. Chem. Soc.* **2014**, *136*, 1609–1616.

(170) Carpinelli, J. M.; Swartzentruber, B. *Phys. Rev. B* **1998**, *58*, R13423–R13425.

(171) Nie, S.; Starodub, E.; Monti, M.; Siegel, D. A.; Vergara, L.; El Gabaly, F.; Bartelt, N. C.; De La Figuera, J.; McCarty, K. F. *J. Am. Chem. Soc.* **2013**, *135*, 10091–10098.

(172) Dieckmann, R.; Schmalzried, H. *Berichte der Bunsengesellschaft/Physical Chem. Chem. Phys.* **1977**, *81*, 414–419.

(173) Peterson, N.; Chen, W.; Wolf, D. *J. Phys. Chem. Solids* **1980**, *41*, 709–719.

(174) Lewis, G.; Catlow, C.; Cormack, A. *J. Phys. Chem. Solids* **1985**, *46*, 1227–1233.

(175) Atkinson, A.; O'Dwyer, M. L.; Taylor, R. I. *J. Mater. Sci.* **1983**, *18*, 2371–2379.

(176) Dieckmann, R.; Hilton, M. R.; Mason, T. O. *Berichte der Bunsengesellschaft/Physical Chem. Chem. Phys.* **1987**, *91*, 59–66.

(177) Lin, C.-M.; Stubican, V. S. *J. Am. Ceram. Soc.* **1990**, *73*, 587–591.

(178) Dorris, S.; Martin, M. *Berichte der Bunsengesellschaft für Phys. Chemie* **1990**, *94*, 721–726.

(179) Stubican, V. S. *Philos. Mag. A Phys. Condens. Matter, Struct. Defects Mech. Prop.* **1993**, *68*, 809–818.

(180) Atkinson, A. *Rev. Mod. Phys.* **1985**, *57*, 437–470.

(181) Tober, S.; Creutzburg, M.; Arndt, B.; Krausert, K.; Mattauch, S.; Pütter, S.; Mohd, A. S.; Koutsioubas, A.; Volgger, L.; Hutter, H.; Noei, H.; Vonk, V.; Lott, D.; Stierle, A. In *Verhandlungen der DPG*, Regensburg, 2019.

(182) Lott, D.; Koutsioumpas, A.; Creutzburg, M.; Mattauch, S.; Vonk, V.; Syed Mohd, A.; Pütter, S.; Stierle, A. In *Ger. Conf. Res. with Synchrotron Radiation, Neutrons Ion Beams Large Facil.* 2019.

(183) Eerenstein, W.; Palstra, T. T. M.; Hibma, T.; Celotto, S. *Phys. Rev. B* **2003**, *68*, 014428.

(184) Muhich, C. L.; Aston, V. J.; Trottier, R. M.; Weimer, A. W.; Musgrave, C. B. *Chem. Mater.* **2016**, *28*, 214–226.

(185) Pavelec, J.; Hulva, J.; Halwidl, D.; Bliem, R.; Gamba, O.; Jakub, Z.; Brunbauer, F.; Schmid, M.; Diebold, U.; Parkinson, G. S. *J. Chem. Phys.* **2017**, *146*, 014701.

(186) Pollak, E. In *Stoch. Process. Physics, Chem. Biol.* Lecture Notes in Physics; Springer, Berlin, Heidelberg: 2000, pp 75–84.

(187) Bartelt, N. C.; Nie, S.; Starodub, E.; Bernal-Villamil, I.; Gallego, S.; Vergara, L.; McCarty, K. F.; De La Figuera, J. *Phys. Rev. B* **2013**, *88*, 235436.

(188) Arndt, B. Atomic Structure and Stability of Magnetite (001)., PhD Thesis, University Hamburg, 2018.

(189) Pentcheva, R.; Wendler, F.; Meyerheim, H. L.; Moritz, W.; Jedrecy, N.; Scheffler, M. *Phys. Rev. Lett.* **2005**, *94*, DOI: 10.1103/PhysRevLett.94.126101.

(190) Łodziana, Z. *Phys. Rev. Lett.* **2007**, *99*, 206402.

(191) Pentcheva, R.; Moritz, W.; Rundgren, J.; Frank, S.; Schrupp, D.; Scheffler, M. *Surf. Sci.* **2008**, *602*, 1299–1305.

(192) Jakub, Z.; Hulva, J.; Mirabella, F.; Kraushofer, F.; Meier, M.; Bliem, R.; Diebold, U.; Parkinson, G. S. *J. Phys. Chem. C* **2019**, *123*, 15038–15045.

List of Abbreviations

AES	Auger Electron Spectroscopy
AFM	Atomic Force Microscopy
APDB	Anti-phase Domain Boundary
DFT	Density Functional Theory
EA	Electron Affinity
fcc	Face-Centred Cubic
FFT	Fast Fourier-Transformation
fps	Frames per Second
FPGA	Field Programmable Gate Array
FWHM	Full Width at Half Maximum
HT	High-Temperature
IMFP	Inelastic Mean Free Path
LDOS	Local Density of States
LEED	Low-Energy Electron Diffraction
LEEM	Low-Energy Electron Microscopy
LEIS	Low-Energy Ion Scattering
LT	Low-Temperature
NAP	Near-Ambient Pressure
QMS	Quadrupole Mass Spectrometry
RAM	Random-Access Memory
STM	Scanning Tunnelling Microscopy
SXRD	Surface X-Ray Diffraction
TC	Thermocouple
TEM	Transmission Electron Microscopy
TPD	Temperature Programmed Desorption
UHV	Ultra-High Vacuum
UPS	Ultraviolet Photoelectron Spectroscopy
UV	Ultraviolet
VT	Variable Temperature
WF	Work Function
UUC	Unreconstructed Unit Cell
WGS	Water-gas Shift
XPS	X-Ray Photoelectron Spectroscopy

List of Figures

List of Tables

Appendix

Supporting Figures to Chapter 4.2

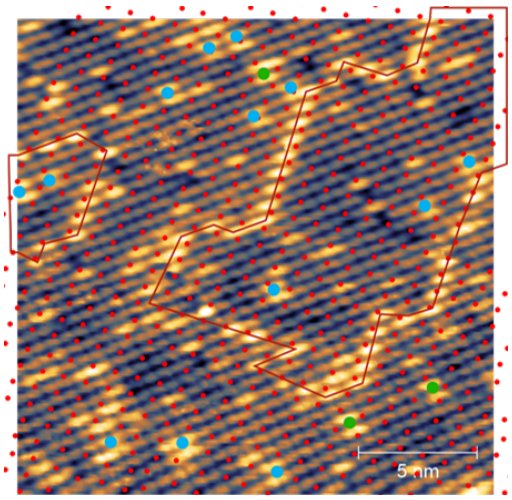

(a)

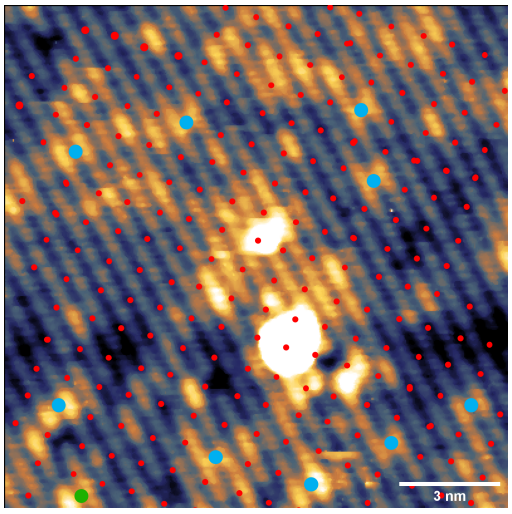

(b)

Figure .1: (a) Atomically resolved STM image of $Fe_3O_4(001)$ surface at room temperature used to determine the locations of double-lobed features (assigned to unreconstructed unit cells, UUCs). A unique spot in the unit cell is marked by red points at the blocked site of the unit cell based on the central domain, APDBs are marked by red lines, UUCs at their original blocked sites are marked in blue, those at unblocked sites are marked in green. APDBs shift the unit cell by half a unit cell, leading the red points to mark the unblocked sites in the left and right domains instead of the blocked sites in the central domain. As described in the text, UUCs at the original blocked sites are found more often by approximately a 9:1 ratio compared to those at unblocked sites (U_B = 1.5V, I_t = 0.3 nA).

"[H]e has dreamed many dreams about time. His dreams have taken hold of his research. His dreams have worn him out [...] . But the dreaming is finished. Out of many possible natures of time, imaged in as many nights, one seems compelling."

- Alan Lightman, *Einstein's Dreams*, 1993.